Open microfluidic technologies for fundamental and applied studies of human health and the environment

Ulri N. Lee

A dissertation
submitted in partial fulfillment of the
requirements for the degree of

Doctor of Philosophy

University of Washington
2022

Reading Committee:
Ashleigh B. Theberge, Chair
Alshakim Nelson
Robert E. Synovec

Program Authorized to Offer Degree:
Chemistry

University of Washington

Abstract

Open microfluidic technologies for fundamental and applied studies of human health and the environment

Ulri N. Lee

Chair of the Supervisory Committee:
Ashleigh B. Theberge, Ph.D.
Department of Chemistry

This dissertation discusses the applications for open microfluidics in emerging technologies for studying human health and the environment. Open microfluidics is a sub-field of microfluidics that is quickly gaining traction for technologies across biology and the environment. The open nature of the microchannels enables flexibility to the user for adding or removing components and makes it simple to use. Chapter 1 introduces how microfluidics has traditionally been used and provides a background of open microfluidics and the common methods used to fabricate devices. Chapter 2 evaluates rapid injection molding, a more economical version of traditional injection molding, for open microfluidic cell-based technologies. Minimum dimensions and dimension accuracy are investigated for applications with fluorescence imaging. Chapter 3 highlights a novel method for generating droplets in an open microfluidic device that utilizes natural hydrostatic pressure and therefore does not require pumps or external equipment to generate the droplets. Additionally, potential use cases are presented for applications in droplet manipulation, patterning, splitting, and fusion. Chapter 4 presents a layer-by-layer hydrogel patterning method made possible by spontaneous capillary flow. An open microfluidic rail-based device is used to pattern entire layers of hydrogels for biological applications in tissue engineering, organoid development, and 3D cell culture. Chapter 5 presents a novel method for capturing airborne particles using microdroplets and open microfluidic channels for shuttling the collected sample across the device. The work presented here demonstrates fundamental open microfluidic principles for droplet

generation and fabrication as well as how open microfluidics can be applied to diverse fields of study such as hydrogel patterning and environmental sampling.

Table of Contents

List of Figures

Acknowledgements

I am grateful to have been surrounded by so many amazing, loving, and supportive people throughout my PhD. Thank you to the entire Theberge Lab, past and present, for shaping my graduate experience; I am thankful to have experienced working with a diverse group of scientists and learning from, and alongside, you all. Thank you to co-authors, John Day, Amanda Haack, Jian Wei Khor, Tammi van Neel, Xiaojing Su, Ashley Dostie, and Hannah Lea. Co-leading projects with you all solidified my belief that two (or more) heads are better than one.

To Ashleigh, being mentored by you has been an invaluable experience and I am forever grateful that I was not only able to witness your leadership but also be a recipient of your dedication to mentoring quality scientists. Thank you for believing in me and trusting me with the responsibility of conducting research in your lab. You have fostered the confidence in me to pursue research as a career and inspire me to be the best mentor, teacher, and colleague that I can. Thank you for your authenticity, integrity, and transparency; you are a role model to so many young scientists, myself included. Thank you. To Erwin, thank you for always sharing your creative ideas and unique approaches to problems. I have learned from you to not fear sharing my ideas even if I'm not sure how they will be received. To Sanitta, thank you for welcoming me to the CandyCollect team. It was a pleasure to work with you and the amazing team of students you brought together.

Tianzi, Dostie, Jing, and Sam, you all played an integral role in shaping my undergraduate and graduate research experience. Thank you for showing me from the beginning what it means to be a great scientist, teacher, and supportive lab mate. Tammi, thank you for your trust, loyalty, and entertaining my wild ideas, many of my favorite memories from graduate school were from our time working on the air sampling project.

Lastly, thank you to my family for keeping me grounded and reminding me the importance of being present and spending time with the ones you love. Mom and Dad, thank you for supporting my education from day one and providing me with a welcoming home to come to. To Lia and Erika, thank you for getting me through my detail-obsessed-panics; to Alex, thank you for letting me visit you in Bozeman when I needed a brief escape from my PhD; and to Bret, thank you for your consistent love, humor, and understanding.

Dedication

For my mom and dad, who gave me the space to explore and choose my own path.

Chapter 1 | Introduction

1.1 Introduction to open microfluidics

Microfluidics is a field that began emerging during the early 2000s.[1] A microfluidic system is defined as a fluid system where at least one dimension is on the sub-millimeter scale. Consequently, little fluid (10^{-9} to 10^{-18} liters) is required for conducting microfluidic experiments, enabling high throughput and more sensitive analytical measurements with less material and reagent usage.[1] Sitting at the intersection of chemistry, biology, and engineering, the interdisciplinarity of microfluidics enables innovation and exciting applications across the intersecting fields.

A subfield of microfluidics, open microfluidics, has been increasing in popularity due to its manufacturability, ease of use, and elimination of tubing and pumps.[2-4] In a traditional microfluidic system, the microfluidic chip is connected to a network of tubing and one or more pumps to generate the fluid flow throughout the channels. Consequently, once the microfluidic chip is set up, it is difficult to move across the lab space and typically has a large laboratory footprint. Additionally, in open microfluidic systems, at least one side of the microfluidic area is open to the air enabling access to the channels at any point and adding a level of customizability not found in traditional microfluidic systems.[5] The open surface enables intervention with tools such as standard laboratory pipettes to add, remove, and manipulate fluids throughout the experiment.[5, 6] In addition, open systems do not require pumps and actuators, users simply pipette their fluids into the channel; this feature enables open microfluidic technology to be used by labs without specialized equipment.[7] Without pumps and actuators, flow in open microfluidic channels is established by leveraging spontaneous capillary flow (SCF).[8] A previously derived simplified equation (Eq 1) makes it simple for anyone to design an open microfluidic channel that meets the conditions for SCF because there are only a few considerations-- the contact angle of the flowing fluid on the channel surface, θ, and the wetted P_w and non-wetted P_f perimeters of the channel (Figure 1.1).[8] Capillary-driven open

$$\frac{P_f}{P_w} < cos\theta \quad \text{(Eq 1)}$$

microfluidics have lower throughput compared to traditional microfluidics because capillary flow rates are lower than pump-generated flow rates.[9] However, for some applications the usability of an open microfluidic system outweighs the benefits of a high-throughput especially if high-throughput experiments are not essential to the end goal.

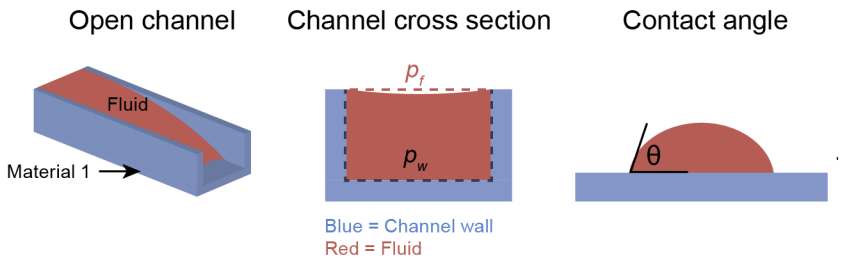

Figure 1.1. Components of an open channel required to determine spontaneous capillary flow.

Some considerations when implementing an open microfluidic workflow, especially those involving cells and other biological components, are evaporation and contamination. These two factors often cause hesitation with adopting an open microfluidic workflow, however, methods have been developed to mitigate evaporation and contamination. One solution is to add sacrificial liquid near the microfluidic channel which has been shown to help maintain the partial pressure of water at equilibrium above the liquid in the channel.[10] Day and Nicholson *et al.* also developed and evaluated open microfluidic devices with liquid reservoirs for sacrificial liquid designed directly on top of the microfluidic device.[11] Lastly, a secondary container for the device has been successfully used to prevent evaporation and contamination because it adds an additional physical layer to prevent contaminants from entering the system and moisture exiting.

1.2 Fabrication and scaling microfluidic technologies

For microfluidic technologies to make the greatest impact they must be scalable and easy to use. The manufacturability of a design is essential for scalability because not all manufacturing methods can

execute all design features. The following subsections touch on the common fabrication methods for microfluidic devices.

1.2.1 3D printing

3D printing is a very versatile fabrication method when it comes to geometries; it can produce parts with overhanging or hollow features which are more difficult or impossible for milling and injection molding.[12] In addition, 3D printing has proven to be a great technology for prototyping open microfluidic devices because users can have an iteration of a design in <24 hrs.[13] While it is a fantastic autonomous tool for prototyping and small-scale production (1-500 devices), due to the speed of 3D printing and limited space on a 3D printer, it is not yet at the stage where it is reasonable for producing thousands of parts which has prevented its use in large scale microfluidic device fabrication.

1.2.2 Soft lithography

Soft lithography revolutionized microfluidics and is typically the method of choice when precision in nanometer and micrometer sized channels is needed.[14, 15] Briefly, polydimethylsiloxane (PDMS) is cast or spin coated over a silicon mold and heated to cure. While PDMS is a cost-effective material, the silicon molds require a clean room to fabricate and are costly.[16] PDMS is optically clear and inert which makes it ideal for microscopy and compatible for biological applications.[15] However, a major limitation to PDMS is that it absorbs small molecules which is problematic when many applications target small metabolites or molecules as the analyte of interest.[17] Additionally, PDMS devices are difficult to scale because they require a bonding step to adhere the PDMS to a substrate and close the channel.[18, 19]

1.2.3 Micromilling

Thermoplastics such as polystyrene, polypropylene, and cyclic olefin co-polymer are popular because of their manufacturability with micromilling and injection molding.[20] They provide the benefits of optical clarity for imaging, biological compatibility, solvent compatibility (polypropylene), and do not absorb small molecules.[21] Micromilling enables the fabrication of high precision parts out of thermoplastics in addition to metal, acrylic, polytetrafluoroethylene (PTFE), and others.[20] Micromilled polystyrene is an

excellent material for cell-based assays since polystyrene is a gold standard cell culture material.[22] While the upfront cost of milling is higher due to the initial cost of the mill (>$15k), the cutting tools can be used for many hours of milling if maintained well and the workpiece (material being milled) is relatively affordable.[20] A typical 3-axis micromill is designed to mill vertical walls with standard endmills and some simple overhanging geometries with specialized endmills. While the geometric versatility of micromilling is less than that of 3D printing and the resolution of features is limited to the micron scale as opposed to the nanometer scale for soft lithography, micromilling provides material compatibility and versatility for cell-culture grade microfluidics devices.[20]

1.2.4 Injection molding

To largely disseminate open microfluidic tools, large-scale manufacturing processes must be employed. Traditionally, injection molding is used as the gold standard for the large-scale manufacturing of thermoplastics because it can produce 10,000< of parts efficiently.[23, 24] However, traditional rapid injection molding is expensive and can take up to 12 weeks because a steel mold is used for the parts (sometimes exceeding $50,000 for the mold). More recently, rapid injection molding has been used to produce 500-10,000 parts with a turnaround time of two weeks and at a much lower cost ($2,000-$5,000 for the mold) because it uses an aluminum mold.[25] The tradeoff is that rapid injection molding cannot produce as many parts per mold because aluminum wears down more quickly than steel.[25] However, for academic labs where traditional injection molding costs can be prohibitive and millions of parts unnecessary, rapid injection molding provides an alternative to traditional injection molding.

1.3 Applications and advances of open microfluidics for biology and the environment

Open microfluidics is a tool that can be leveraged for many different applications. As an example, the following subsections briefly discuss how open microfluidics has been implemented in the technology of three different fields.

1.3.1 Open droplet microfluidics

An entire subfield of microfluidics has been dedicated to droplet generation and manipulation with the vast majority of droplet microfluidic workflows utilizing closed-channel microfluidic devices. Droplet microfluidics is a powerful analytical tool that enables researchers to precisely control the environment within the droplet. The droplets act as microscale reaction chambers where reactions are expedited due to faster mixing of reagents and the contents can be controlled even to a single cell.[26] Several applications on the cellular and molecular level such as single cell analysis, RNA and DNA analysis (PCR), drug discovery, medical diagnostics, and materials chemistry.[27] Not only are applications for droplet microfluidics expanding, but so is our fundamental understanding of the physics within the system.[28, 29] Leveraging our growing understanding of the physis in a droplet system, droplet manipulation techniques have advanced and been an area of interest because of its ability to open up the repertoire of applications for droplet microfluidics. Techniques to split, merge, and sort droplets by mechanical, acoustic, electric, and magnetic forces have been developed to control droplet microfluidic workflows and reactions.[30]

To implement a droplet microfluidic workflow into a laboratory, the users must know how to determine flowrates for the desired droplet throughput, connect various tubing to the appropriate ports (can often be 10+), and troubleshoot for any technical issues such as clogging. While droplet microfluidics is a valuable analytical tool for many fields, these requirements are often a barrier to entry for researchers whose primary field is not droplet microfluidics. There is room for a more user-friendly droplet microfluidic platform that can easily be adopted by non-specialists. To address this need, we leveraged open microfluidics to create a droplet generation platform that does not require pumps or tubing. The user can use a standard laboratory pipette to dispense the aqueous phase that will form the droplets and the carrier phase that will guide the droplets through the open channel. Once the carrier phase is dispensed, droplets begin to generate autonomously due to the inherent hydrostatic and capillary pressures in the device. The open platform is particularly enabling because the user can selectively retrieve, sort, and manipulate droplets with simple tools like tweezers.

1.3.2 Hydrogel structures for tissue engineering and 3D cell culture

Engineers and biologists have leveraged 3D printing technology to print tissues, cell-laden hydrogels, and biopolymers.[31, 32] The resulting 3D printed structure is primarily hydrogel-based and designed to mimic organs and tissues in the human body, which can be used for both in vivo and in vitro experiments.[33] To print 3D hydrogel-based structures with specific shape and composition, the printing process is often lengthy because small amounts of material are deposited at a time and multiple nozzles are needed for multi-material structures.[31] In most 3D printing, where nozzles dispense material by rastering back and forth, they are prone to clogging and require xyz stages and mechanics. Open microfluidics enables entire layers of material to be deposited directly where it will be used such as in a well plate, a standard vessel for cell culture.[34] With each layer, a new material can be used to fill the open channel, enabling multimaterial structures with only the use of pipettes and patterning devices. Open microfluidic layer-by-layer hydrogel patterning is particularly accessible for those who do not have the expertise or training in 3D printing but would like to be able to form 3D hydrogel structures.

1.3.3 Environmental air sampling

Air sampling techniques come in a wide range of forms and functions. From large industrial systems to portable devices the size of a keychain, their uses can vary from detecting specific gasses like a home carbon monoxide monitor to capturing viruses. The air sampling field is saturated with many different types of devices and yet there is still no gold standard, making new technologies difficult to validate. A major challenge is that air is a constantly changing, complex matrix and accurate measurements are affected by humidity, temperature, and air flow. Often specialists are needed to evaluate airborne hazards by visiting the site and inspecting the area, which is not an accessible service for everyone. There is a need for technologies that people can use to sample the air without training and then ship the sample to a lab with analytical tools for sophisticated analysis.

For efficient capture, active methods utilizing pumps or fans to pull in larger volumes of air have been used.[35] However, bioaerosols often become desiccated under the air flow preventing analysis of viability, an important factor when determining the risk it poses to human health.[36] To prevent desiccation, liquid and

hydrogel components have been incorporated into air sampling devices and been successful in improving capture and viability of bioaerosols.[37] With this in mind, we developed a device that uses liquid microdroplets to capture bioaerosols. Open microfluidic channels direct the collected aerosol-laden liquid sample to a collection reservoir. The open channels do not clog, an essential feature for transporting particles, and provide flexibility to move the collected sample on the device via SCF without any pumps.

1.4 References

1. G. M. Whitesides, *Nature*, 2006, **442**, 368-373.
2. L. J. Barkal, A. B. Theberge, C.-J. Guo, J. Spraker, L. Rappert, J. Berthier, K. A. Brakke, C. C. Wang, D. J. Beebe and N. P. Keller, *Nature communications*, 2016, **7**, 1-11.
3. T. De Groot, K. Veserat, E. Berthier, D. Beebe and A. Theberge, *Lab on a Chip*, 2016, **16**, 334-344.
4. Y. Lee, J. W. Choi, J. Yu, D. Park, J. Ha, K. Son, S. Lee, M. Chung, H.-Y. Kim and N. L. Jeon, *Lab on a Chip*, 2018, **18**, 2433-2440.
5. J. J. Lee, J. Berthier, K. A. Brakke, A. M. Dostie, A. B. Theberge and E. Berthier, *Langmuir*, 2018, **34**, 5358-5366.
6. S. B. Berry, J. J. Lee, J. Berthier, E. Berthier and A. B. Theberge, *Analytical Methods*, 2019, **11**, 4528-4536.
7. J. J. Lee, J. Berthier, A. B. Theberge and E. Berthier, *Langmuir*, 2019, **35**, 10667-10675.
8. B. P. Casavant, E. Berthier, A. B. Theberge, J. Berthier, S. I. Montanez-Sauri, L. L. Bischel, K. Brakke, C. J. Hedman, W. Bushman, N. P. Keller and D. J. Beebe, *Proceedings of the National Academy of Sciences*, 2013, **110**, 10111.
9. M. Zimmermann, H. Schmid, P. Hunziker and E. Delamarche, *Lab on a Chip*, 2007, **7**, 119-125.
10. E. Berthier, J. Warrick, H. Yu and D. J. Beebe, *Lab on a Chip*, 2008, **8**, 852-859.
11. J. H. Day, T. M. Nicholson, X. Su, T. L. van Neel, I. Clinton, A. Kothandapani, J. Lee, M. H. Greenberg, J. K. Amory, T. J. Walsh, C. H. Muller, O. E. Franco, C. R. Jefcoate, S. E. Crawford, J. S. Jorgensen and A. B. Theberge, *Lab on a Chip*, 2020, **20**, 107-119.
12. N. Shahrubudin, T. C. Lee and R. Ramlan, *Procedia Manufacturing*, 2019, **35**, 1286-1296.
13. N. Bhattacharjee, A. Urrios, S. Kang and A. Folch, *Lab on a Chip*, 2016, **16**, 1720-1742.
14. D. Bratton, D. Yang, J. Dai and C. K. Ober, *Polymers for Advanced Technologies*, 2006, **17**, 94-103.
15. Y. Xia and G. M. Whitesides, *Angew Chem Int Ed Engl*, 1998, **37**, 550-575.
16. J. C. Love, J. R. Anderson and G. M. Whitesides, *MRS Bulletin*, 2001, **26**, 523-528.
17. M. W. Toepke and D. J. Beebe, *Lab on a Chip*, 2006, **6**, 1484-1486.
18. M. A. Eddings, M. A. Johnson and B. K. Gale, *Journal of Micromechanics and Microengineering*, 2008, **18**, 067001.
19. A. Borók, K. Laboda and A. Bonyár, *Biosensors*, 2021, **11**, 292.
20. D. J. Guckenberger, T. E. de Groot, A. M. D. Wan, D. J. Beebe and E. W. K. Young, *Lab on a Chip*, 2015, **15**, 2364-2378.
21. E. Gencturk, S. Mutlu and K. O. Ulgen, *Biomicrofluidics*, 2017, **11**, 051502.
22. E. K. Sackmann, A. L. Fulton and D. J. Beebe, *Nature*, 2014, **507**, 181-189.
23. B. H. You, D. S. Park, P. C. Chen, S. D. Rani, D. E. Nikitopoulos, S. A. Soper and M. C. Murphy, presented in part at the ASME 2008 International Mechanical Engineering Congress and Exposition, 2008.

24. V. Piotter, T. Hanemann, R. Ruprecht and J. Haußelt, *Microsystem Technologies*, 1997, **3**, 129-133.
25. U. N. Lee, X. Su, D. J. Guckenberger, A. M. Dostie, T. Zhang, E. Berthier and A. B. Theberge, *Lab on a Chip*, 2018, **18**, 496-504.
26. S. Y. Teh, R. Lin, L. H. Hung and A. P. Lee, *Lab Chip*, 2008, **8**, 198-220.
27. M. T. Guo, A. Rotem, J. A. Heyman and D. A. Weitz, *Lab on a Chip*, 2012, **12**, 2146-2155.
28. C. N. Baroud, F. Gallaire and R. Dangla, *Lab on a Chip*, 2010, **10**, 2032-2045.
29. J. Berthier and K. A. Brakke, *The Physics of Microdroplets*, Wiley, 2012.
30. C.-G. Yang, Z.-R. Xu and J.-H. Wang, *TrAC Trends in Analytical Chemistry*, 2010, **29**, 141-157.
31. S. V. Murphy and A. Atala, *Nature biotechnology*, 2014, **32**, 773-785.
32. C. Mandrycky, Z. Wang, K. Kim and D.-H. Kim, *Biotechnology advances*, 2016, **34**, 422-434.
33. P. S. Gungor-Ozkerim, I. Inci, Y. S. Zhang, A. Khademhosseini and M. R. Dokmeci, *Biomaterials science*, 2018, **6**, 915-946.
34. U. N. Lee, J. H. Day, A. J. Haack, R. C. Bretherton, W. Lu, C. A. DeForest, A. B. Theberge and E. Berthier, *Lab on a Chip*, 2020, **20**, 525-536.
35. J. Cox, H. Mbareche, W. G. Lindsley and C. Duchaine, *Aerosol Sci Technol*, 2020, **54**, 572-584.
36. Z. Wang, T. Reponen, S. A. Grinshpun, R. L. Górny and K. Willeke, *Journal of Aerosol Science*, 2001, **32**, 661-674.
37. M. Pan, J. A. Lednicky and C. Y. Wu, *Journal of Applied Microbiology*, 2019, **127**, 1596-1611.

Chapter 2 | Fundamentals of Rapid Injection Molding for Microfluidic Cell-based Assays

Reproduced in part from U. N. Lee, E. Berthier, X. Su, J. Guckenberger, A. M. Dostie, T. Zhang, and A. B. Theberge, "Fundamentals of injection molding for cell-based microfluidics." Lab on a Chip, 2018, ***18****, 496–504.*

UNL collected all measurement data, EB and JG designed the device, XS conducted cell culture and imaging experiments, AMD and TZ conducted preliminary experiments, EB and ABT supervised and conceptualized the work.

Abstract: Microscale cell-based assays have demonstrated unique capabilities in reproducing important cellular behaviors for diagnostics and basic biological research. As these assays move beyond the prototyping stage and into biological and clinical research environments, there is a need to produce microscale culture platforms more rapidly, cost-effectively, and reproducibly. 'Rapid' injection molding is poised to meet this need as it enables some of the benefits of traditional high volume injection molding at a fraction of the cost. However, rapid injection molding has limitations due to the material and methods used for mold fabrication. Here, we characterize advantages and limitations of rapid injection molding for microfluidic device fabrication through measurement of key features for cell culture applications including channel geometry, feature consistency, floor thickness, and surface polishing. We demonstrate phase contrast and fluorescence imaging of cells grown in rapid injection molded devices and provide design recommendations to successfully utilize rapid injection molding methods for microscale cell-based assay development in academic laboratory settings.

2.1 Introduction

Microscale cell-based and organotypic models have matured significantly over the last decade.[1-6] As micro-technologies move beyond the proof-of-concept stage and into biological or clinical research, there is a critical need to produce larger quantities of devices with a higher level of reproducibility than is enabled by typical prototyping techniques.[Error! Bookmark not defined.,7] Here we demonstrate that 'rapid injection molding' is well poised to bridge the gap between proof-of-concept device development in bioengineering labs and the adoption by biological and clinical end users who require batches of hundreds to thousands of devices.

Traditional early-stage prototyping methods, such as computer numerical control (CNC) micromilling,[8] hot embossing,[9-12] soft lithography,[13,14] and three-dimensional (3D) printing[15-17] are inexpensive fabrication methods at low quantities with rapid iteration times during the device development phases. However, these methods typically require significant manual preparation steps (e.g. machine setup, master mold fabrication/PDMS preparation, device curing and cleaning) resulting in device-to-device variability and high device costs when part volumes are scaled up. Further, many prototyping techniques alter the materials or require specific materials (e.g., PDMS for soft-lithography and UV-curable resin for 3D printing) that can render the device incompatible with cell-based or other biology research applications.[18,19]

Injection molding, on the other hand, is the gold standard for device manufacturing and enables high-throughput manufacturing of devices (in volumes of hundreds of thousands to millions) at low per-device costs, while maintaining tight tolerances and high reproducibility.[20,21] Further, rapid injection molding enables device production in materials such as polystyrene (PS, typical material for cell cultureware),**Error! Bookmark not defined.**,[22] cyclic olefin copolymer (COC, superior optical properties for microscopy),[23,24] and polypropylene (PP, resistant to organic solvents, a consideration for some sample preparation methods).

Traditional high volume injection molding approaches utilize complex molds fabricated using high quality steel with high precision milling. The tooling of these molds is usually expensive (sometimes exceeding $50,000) and induces significant lead times of up to 12 weeks. However, the molds are made to be highly durable and sustain millions of plastic injections. The high mold cost is typically out of budget for academic research projects, which seldom require millions of devices.

'Rapid' injection molding solutions have emerged in the last 10 years to facilitate the use of injection molding. Companies such as Proto Labs® (Maple Plain, MN, USA) and ARRK (San Diego, CA, USA) offer turn-around times of ~2-15 days. Rapid injection molding sits at the intersection between prototyping methods and traditional high volume injection molding as it costs an order of magnitude less than high volume injection molding ($2,000 to $5,000 to produce a mold for rapid injection molding), allows the use of comparable materials and techniques, and offers rapid turn-around times.[25] It is worth noting that rapid injection molding approaches have been proposed in academic settings using milled molds or nickel-plated

wafers, often drawing on mold capabilities developed for hot embossing.[Error! Bookmark not defined.,26-28] These solutions may push the costs of the technique further down, though they require in-house expertise on these systems.

Rapid injection molding reduces the cost of traditional high volume injection molding by optimizing important steps in the process: (1) design verification and quoting is typically minimalistic and in certain cases is automated by proprietary computer software, (2) the molds are made of softer, less-durable, metals (e.g., aluminum or urethane) that can be produced faster and are only guaranteed for several thousand injections, and (3) the use of inserts that are much smaller and fit into a standard injection molding frame reduce the complexity of the mold tooling (also known as Master Unit Die - MUD Molds or quick change dies). Finally, rapid injection molding usually offers more limited surface polishing options that significantly add to the cost and therefore must be chosen sparingly to keep costs low. The shortcuts of rapid injection molding methods impose significant compromises on the fabrication capabilities and production quality. These can lead to potential sources of failure, particularly for the unique requirements of cell-based microscale systems.

Herein, we examine key features of importance for microfluidic device fabrication, with a focus on cell culture applications. We used 3D laser scanning confocal microscopy to quantify dimensions and image channel cross-sections across a range of aspect ratios in three materials (PS, COC, and PP). For cell culture applications, the roughness and thickness of the cell culture surface are important considerations for phase contrast and fluorescence microscopy. We tested the effect of polishing the metal mold on the surface roughness of the molded plastic; we probed the ability to make thin plastic microwells; and we tested the effects of polishing and plastic thickness on multicolor fluorescence microscopy. We show that injection molded channels can be solvent bonded to additional layers to create closed microchannels. Together this work highlights the versatility of rapid injection molding for open and closed microfluidic cell culture and imaging.

2.2 Comparison of common microfluidic fabrication methods

Rapid injection molding is a technique that is gaining popularity as it sits at the intersection of prototyping and traditional high volume injection molding. It enables the production of ~500-10,000 devices while keeping setup costs low and providing little inter-device variability (Figure 2.1A). These features make it an ideal option for the fabrication of microscale devices during the transfer from design prototyping to initial applications in biology research laboratories or for clinical studies.

In general, injection molding is a process whereby molten plastic is injected into a cavity formed by two (typically metal) molds; the plastic is allowed to cool, then ejected as a solid part (i.e., device). In the context of microfluidic devices, it can be difficult to maintain fidelity in fine features (particularly features with dimensions <0.5 mm). Rapid injection molding companies often utilize proprietary software to screen a customer's designs and flag features that are known to impact feature fidelity, such as the radii of curvature of edges, excessively thick/thin regions, or improper drafting. However, while the design criteria are well known and understood for large parts and macroscale features, we have found that many of the features

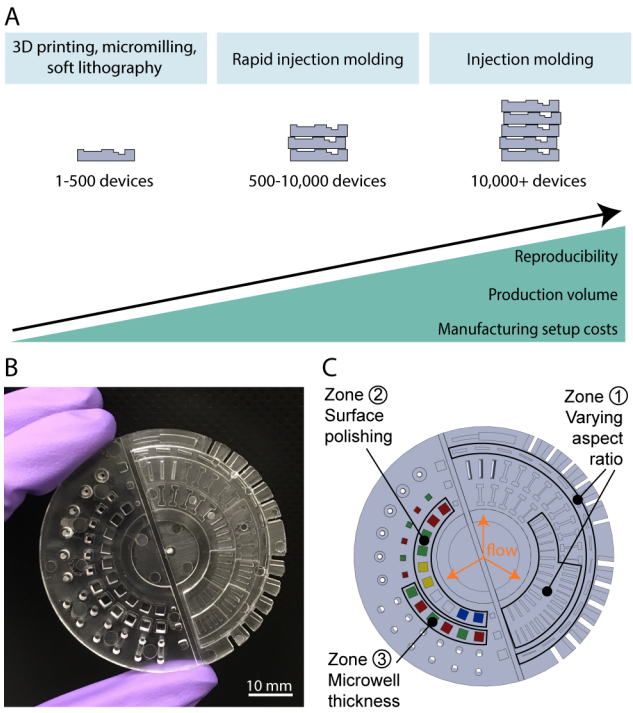

Figure 2.1. (A) Microscale device fabrication methods compared for their advantages and limitations. (B) Photograph of the PS device designed to test key characteristics of rapid injection molding for microscale

cell-based applications. Photos of PP and COC test devices are shown in Figure A1. (C) Schematic of test device highlighting features of interest designed to test key requirements for microscale cell-based applications including rectangular channels positioned parallel and perpendicular to the plastic flow (zone 1), microwells for phase contrast microscopy (zone 2), and microwells for fluorescence microscopy (zone 3).

flagged by the software can actually be fabricated. Therefore, we sought to systematically determine the limits of rapid injection molding for microscale systems and develop strategies to overcome these limitations.

To test the limits of rapid injection molding for microfluidic devices we designed a test device (Figure 2.1B and 2.1C) that contains typical features of microfluidic devices, such as channels of various aspect ratios (Figure 2.1C, zone 1). Further, we designed areas of the test device to simulate cell culture surfaces to assess (1) the impact of different polishing options on the ability to image cells using phase contrast microscopy (Figure 2.1C, zone 2) and (2) the ability to create thin microwells for fluorescence microscopy applications (Figure 2.1C, zone 3).

2.3 Effect of channel aspect ratio and orientation on deviation from designed dimensions

The channels included on the test device represent typical channel geometries commonly used in microfluidic cell culture applications. We designed channels with rectangular cross-sections of varying aspect ratios; the channel depths ranged from 150 μm to 500 μm, and the widths ranged from 200 μm to 700 μm. The channels were imaged using a confocal profilometer, and a cross-section of the 3D image (Figure 2.2A) was taken to measure the bottom width, top width, and height. Each of these measurements were compared to the designed dimensions in the CAD model. The devices were molded in polystyrene (PS), cyclic olefin copolymer (COC), and polypropylene (PP) – materials commonly used for cell culture and biological applications. It is worth noting that we used the same mold for all three materials (to reduce costs), and that the mold/parameters were optimized by Proto Labs® to accommodate the thermal shrinkage of PS. Since PP and COC have different thermal shrinkage rates than PS, we would expect deviations in the dimensions across the materials. Thus, data for PP and COC are provided in Appendix A (Figures A2

and A3) as a reference for the reader; we caution against strict comparisons of the dimensions between the three materials.

We present here the results from the PS device (Figure 2.2) as well as measurements collected from two different batches of PS devices, prepared on two separate metal molds, both with the same design (Figures A4 and A5). We find that the bottom widths are smaller than the top widths for all channel heights

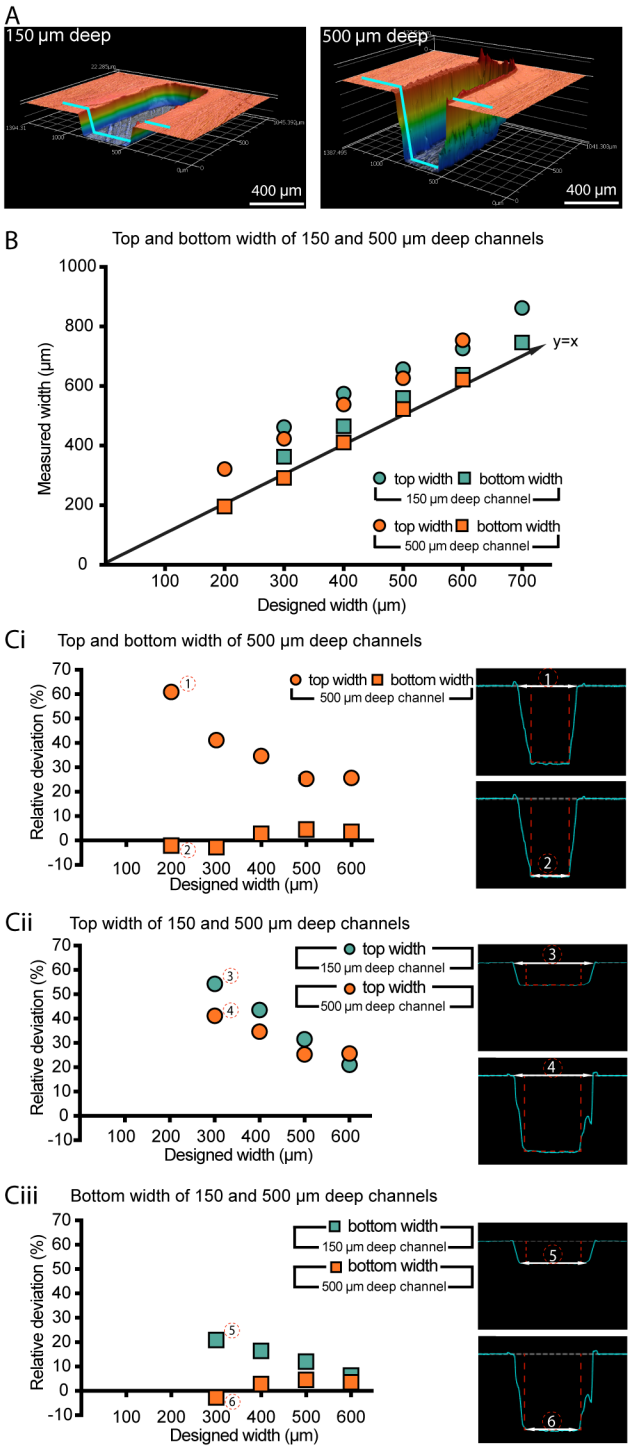

Figure 2.2. Quantification of dimensional differences between the device design and the injection molded device (PS device only). (A) Confocal microscope images of channels (designed width = 300 µm; left channel designed height = 150 µm, right channel designed height = 500 µm). The blue line indicates the cross section used for dimension measurements. Measurements of width were made at both the top and the bottom of the channel. (B) Comparison between the average measured width and the designed width for the 150 µm and 500 µm deep channels (the y=x line, representing ideal correspondence between designed and measured values). (Ci-Ciii) Plots of relative deviation for the parameters indicated (left) and corresponding confocal profilometer cross-sections (right). Data points represent the average of three devices produced by the same mold. In all cases, the standard error of the mean was smaller than the symbol plotted; the complete set of raw data is included in the SI, including separately plotted data points for the three replicate devices.

(Figure 2.2B) despite the fact that no drafting was used (i.e., the walls of the channel should be vertical). The difference in widths is approximately constant (in absolute value) across all channel widths and heights.

As shown in Figure 2.2B, the average measured bottom widths in the 500 μm deep channels were smaller than the corresponding average measured top widths by approximately 90-130 μm. The linear offset is a possible result of tolerancing issues during the machining of the mold (Proto Lab's CNC milling tolerance for metal molds is ± 3 thousands of an inch or 80 μm); further, although flat endmills were used, a small radius results when attempting to mill 90 degree angles. Additionally, the mold was polished by hand, (at an F1 polishing level, 'low cosmetic, most toolmarks removed'), limiting the accuracy of the polishing. Due to the microscale dimensions of the features, the top part of the feature on the mold (bottom of the channel) could have been polished to a greater extent than the bottom of the feature on the mold (top of the channel), resulting in the deviation seen in Figure 2.2. Processing considerations such as temperature, pressure, and time to cool affect which parts of the mold fill first and how completely they fill. It is likely that a combination of these factors contributed to the differences seen in the dimensions of the top and bottom width of the channels. Additionally, the linear absolute change means small features will have larger relative percent deviation from design (Figure 2.2Ci). The relative difference in widths was also larger for shallower channels (i.e., 150 μm) compared to deeper channels (i.e. 500 μm, Figure 2.2Cii-Ciii). Similar patterns were found for COC and PP (Figures A2 and A3).

The device was designed with a circular layout with the gate (i.e., the injection location of molten plastic) at the center to obtain a radial flow of plastic with a controlled direction and even equi-radial velocity (Figure A10A). As expected, our results show that the direction the molten plastic fills the mold is relevant when designing a microfluidic device for injection molding. Rectangular channels were oriented either perpendicular or parallel to the flow of plastic to determine if the direction of molten plastic flow around the features affects the fidelity of the channels (Figure 2.3A). The channels perpendicular to the flow of plastic deviate more in top width than the channels parallel to the flow of plastic (Figure 2.3B). For the perpendicular channels, the increase in deviation from the designed width could be a result of the molten plastic improperly filling behind the metal feature as it flows over it, compared to easily flowing on each side of a metal structure placed to the direction of the flow (Figure 2.3A). This observation indicates a

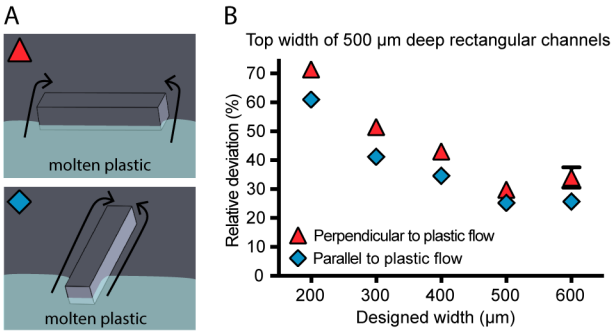

Figure 2.3. Effect of feature orientation relative to the flow of plastic in the mold for PS devices. (A) Schematic of molten plastic flow around mold for channels perpendicular (top) and parallel (bottom) to the flow of plastic. (Flow of plastic in the schematic is represented by light blue shading and arrows.) (B) Graph of average relative deviation in top width for rectangular channels parallel and perpendicular to the PS flow. Data points represent the average of three devices produced by the same mold. In cases where the standard error of the mean was smaller than the symbols plotted, error bars are not shown; the complete set of raw data is included in the SI, including separately plotted data points for the three replicate devices.

potential benefit of placing the gate of injection molded microfluidic device in the main axis of the channels to prevent a perpendicular flow of molten plastic across a channel. We present here the results from the PS device (Figure 2.3), and the equivalent information collected on COC and PP is included in the Appendix A (Figure A2 and A3) as well as measurements collected from two different batches of PS devices, prepared on two separate metal molds (Figure A4 and A5).

2.4 Optical microscopy and surface roughness

Optical microscopy is a widely used technique for imaging cell morphology that requires good optical properties of the microfluidic materials. The aluminum mold from which the plastic devices were produced was fabricated using CNC milling, which inherently leaves tooling marks in the metal mold. We endeavored to determine the level of mold polishing required to enable optical microscopy. Polishing the mold adds to the cost, with higher costs associated with higher polishing levels, so it is important to determine the minimum polishing that enables satisfactory imaging. We studied five levels of polishing offered by Proto Labs®: PM-F0: Non-cosmetic, finish to Proto Labs® discretion; PM-F1: Low-cosmetic, most toolmarks removed; SPI-C1: 600 grit stone; SPI-B1: 600 grit paper; SPI-A2: Grade #2 diamond buff (see Figure 2.1C, zone 2 of the test device).

We measured roughness using the root mean squared (RMS) height of the tooling and polishing marks on the microwell surfaces with 3D laser scanning confocal profilometry (Figure 2.4). The results indicate that the RMS increased with polishing from PM-F1 to SPI-B1 (Figure 2.4B), and the images (Figure 2.4A, top) show that from PM-F1 to SPI-B1 increased polishing only served to remove large tooling marks but increased smaller scale scratches on the device surface. The RMS decreased only at the highest level of polishing, SPI-A2 (Figures 2.4A, top and 2.4B). Correspondingly, only SPI-A2 polishing enabled sufficient clarity for phase contrast microscopy imaging of prostate epithelial cells (BHPrE1 cells) (Figure 2.4A, bottom). The data and images shown in Figure 2.4 correspond to the COC device. Surface roughness measurements for PS, another optically viable material for microscopy and common cell cultureware material, showed similar results to COC (Figure A8).

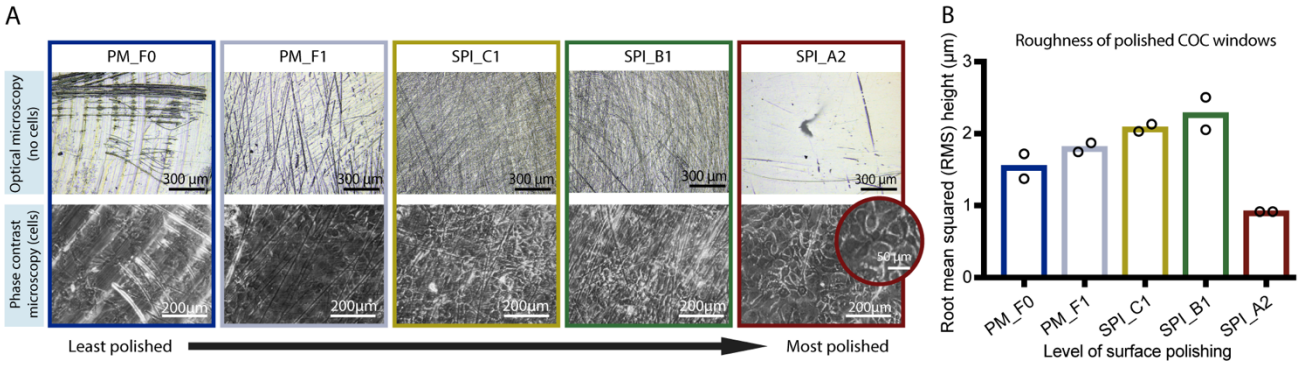

Figure 2.4. Effect of aluminum mold polishing on surface roughness of COC microwells and on clarity of phase contrast microscopy images of cells grown in COC microwells. The results indicate that the highest level of polishing (SPI_A2) is required for clear phase contrast images. Microwells corresponding to the data presented in this figure are shown in zone 2 of the test device schematic (Figure 2.1C), with the same color-coding to represent the level of polishing applied to the metal mold. Abbreviations "PM_F0" though "SPI_A2" correspond to the polishing level options offered by Proto Labs® (see further explanation in Results section). (A) Top row: Optical microscopy images of COC microwells without cells imaged using a 3D laser scanning confocal microscope. Bottom row: Phase contrast microscopy images (10x magnification) of prostate epithelial cells (BHPrE1) grown on COC microwells; original images are included in Figure A9. Images are representative of two replicate microwells from one device. (B) Surface roughness (root mean squared (RMS) height) of COC surfaces measured using 3D laser scanning confocal microscopy. The bars indicate the mean of two replicate microwells from one device (data points from two replicates are superimposed on the bars).

2.5 Fluorescence microscopy

Fluorescence microscopy is a ubiquitous and quantitative tool used in cell-biology research that often requires high-magnification imaging to observe sub-cellular features. In addition to polishing that affects the ability to resolve cellular features as described previously, the thickness of the plastic can affect the resolution of imaging (some microscope objectives are tuned to be used with cover slips of specific thickness with a specific refraction index). In our test device, we included microwells with plastic thicknesses ranging from 100 µm to 350 µm, increasing in 50 µm increments, and with alternating polishing levels between SPI_B1 and SPI_A2, the two highest levels of polishing available at Proto Labs® (see Figure 2.1C, zone 3 of the test device). These dimensions span typical thicknesses of glass cover slips. We measured the actual thickness of the floor of the COC microwells to be ~40-50 µm greater than designed (Figure A6A). The PS devices were ~5-30 µm greater than designed (Figure A6B) and the PP devices were

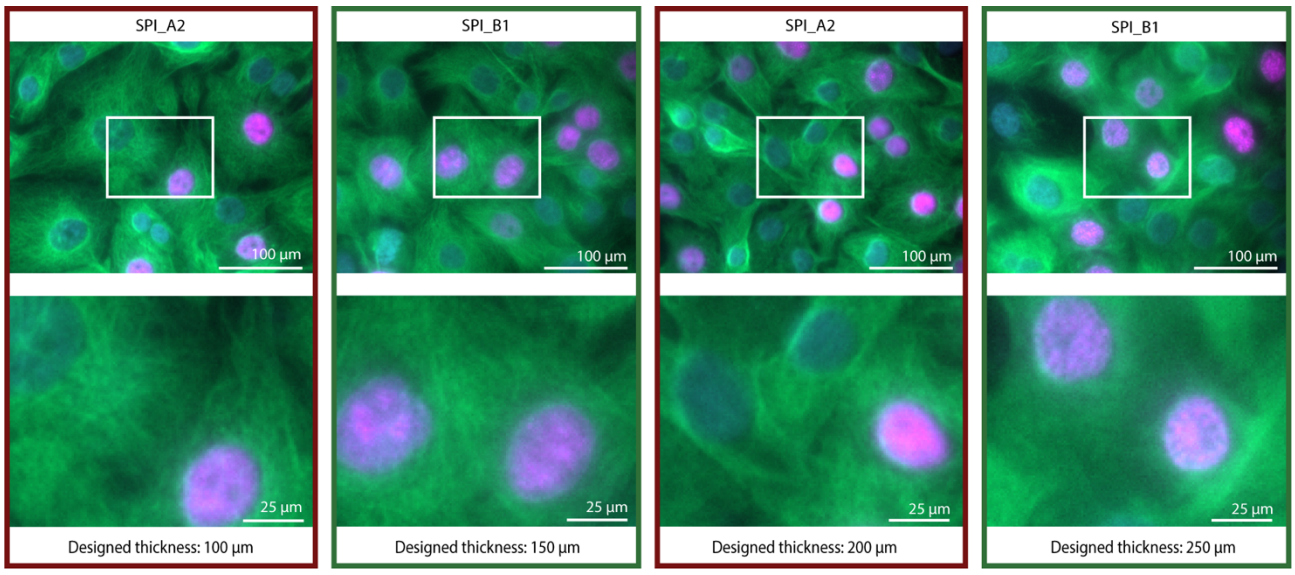

Figure 2.5. Fluorescence microscopy images of cells grown in COC microwells of varied thickness and polishing. Fluorescence images of prostate epithelial cells (BHPrE1) taken at 20x (0,40 NA) magnification with nuclear staining (DAPI, blue), proliferating nuclei (EdU, red), and tubulin (green). Zoomed in images of areas outlined in white are on the bottom row. The original images (with larger field of view) are included in Figure A7. The results indicate that the highest polishing level, SPI_A2, and a designed thickness of 100 µm enables clear images. Microwells corresponding to the data presented in this figure are shown in zone 3 of the test device schematic (Fig. 1C). The designed thickness is indicated in this figure; measurements of actual thickness are included in the SI, Figure A6A. Images bordered with red frames correspond to SPI_A2 polishing; green frames correspond to SPI_B1 polishing.

~0-20 μm greater than designed (Figure A6C). Thus, the COC microwell with a designed thickness of 100 μm resulted in an actual thickness of 150.4 ± 2.4 μm, corresponding closely to No. 1.5 glass coverslips (thickness of 160-190 μm), commonly used in microscopy. While microwells of 100 μm designed thickness formed in all COC and PP devices (n=50), the microwells did not form in PS devices (these molded as undesired through holes in the device) (Figure A6B). Creating thin plastic features of dimensions compatible with high-magnification microscopy is thus possible using rapid-injection molding. Further, our results indicated the highest Proto Labs® polishing level (SPI_A2, Grade #2 Diamond Buff) on the thinnest COC microwells (i.e., designed thickness 100 μm, actual thickness 150.4 ± 2.4 μm) enabled multicolor fluorescence microscopy. An example image showing clarity in the tubulin immunofluorescence stain and nuclear stains (DAPI and EdU) in BHPrE1 prostate epithelial cells is shown in Figure 2.5.

2.6 Fabricating closed channels with solvent bonding

The creation of microfluidic devices from injection molded devices often requires the bonding of an additional layer of plastic to create closed cavities.[Error! Bookmark not defined.,30,31] Figure 2.6A shows an example of a polystyrene cell culture device in which the channel walls and ceiling were produced by injection molding and the floor of the channel is a polystyrene sheet that is bonded to the injection molded device using acetonitrile solvent bonding. The device is based on a design previously published for primary testis cell culture studies.[32] Maintaining a planar surface to allow reliable solvent bonding presents design challenges in the context of injection molding. Areas of varying thickness result in regions of the device cooling and solidifying at different rates and thus variable shrinking arises. Thicker regions of the device can lead to a phenomenon called ‘sinking’ in which visible deformation of the plastic surface occurs. In the design presented, the channels were 1.0 mm in depth. As that thickness across the whole device would have led to sinking, the device was designed as an array of 1.5 mm thick oval ‘islands’ in which the channels were molded (Figure 2.6). The space in between these raised island structures also provided an area for solvent to evacuate during the solvent bonding process.

In practice, we found that the cross sections of the oval islands surrounding the channel were slightly curved (Figure 2.6B); potentially due to the uneven cooling rates of the thicker plastic in the island regions

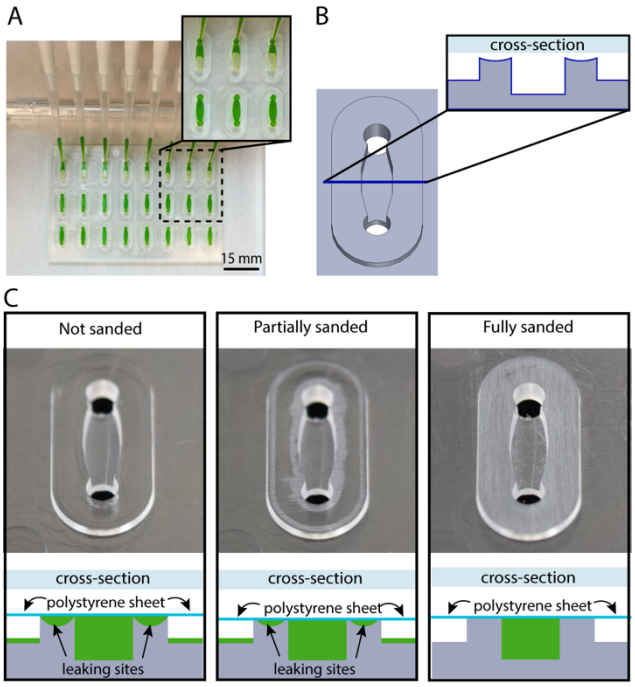

Figure 2.6. Closed channel cell culture device fabricated by solvent bonding a PS sheet (comprising the channel floor) and a PS injection molded device (comprising the channel walls and ceiling). (A) Closed channel cell culture device with multiplexed channel filling using a multichannel pipette. (B) Schematic of a single channel with oval island surrounding the channel. The cross-section (inset) shows that the oval island surrounding the channel is slightly curved due to plastic sinking caused by variable cooling rates of thick and thin regions of the injection molded device. (C) Schematic diagrams illustrating channel cross sections after solvent bonding to a PS sheet. For clarity the orientation of the schematic matches the orientation of the photographs directly above; when in operation, the device is flipped over such that the PS sheet forms the floor (as shown in A). The schematic diagrams indicate the results of filling the solvent bonded devices with fluid (green); leaking occurs when devices are assembled without sanding. Sanding provides a flat surface for solvent bonding enabling a leak-free device. Photographs show whitened areas of plastic removed by sanding the oval islands.

compared to the thinner plastic on the remainder of the device. The curvature of the island prevents the polystyrene sheet from properly bonding to the device and results in channel leakage (shown schematically in Figure 2.6C, bottom). To solve this problem, we manually sanded the surface of the device to remove the top layer of plastic until it was flat, enabling successful solvent bonding (Figure 2.6C, top) and a leak-free array of closed channel devices (Figure 2.6A).

2.7 Conclusion

We demonstrate here that rapid injection molding is an efficient and attractive technique to bring microscale platforms from the initial design stage to a reproducible, medium volume, application phase.

Rapid injection molding enables the production of microdevices in volumes of 500 – 10,000 at mold costs of $2,000-5,000 with little inter-device variability. Importantly, injection molding enables the selection of materials that have demonstrated advantages for cell culture (e.g., polystyrene) and optical properties (e.g., COC). We show that rapid injection molding induces a small amount of deformation to the rectangular cross-section of a channel, though channels with a width of as low as 200 μm were produced with good precision. Further, we show that rapid injection molding can produce chambers for cell culture that are compatible with optical microscopy and fluorescence microscopy – an essential feature for cell-based microfluidics and organotypic microscale models. Finally, rapid injection molding is compatible with microdevice construction using solvent bonding methods to create closed channels. Further, rapid injection molding is optimally suited for capillary-driven open microfluidic techniques in which the devices can be utilized directly after injection molding, without further fabrication steps.[33,34] With the right design considerations, rapid injection molding is a technique that is compatible with academic resources and that has the potential to enable the translation of technologies toward biological or clinical research.

2.8 Materials and methods

Device fabrication: Devices were designed using SolidWorks (2016). Devices were manufactured using the Protomold service by Proto Labs®; Appendix A provides considerations when working with and choosing rapid injection molding companies. The following methods were provided in brief from Proto Labs®. The device molds were micromilled from aluminum on a HAAS 3-axis CNC mill (HAAS Automation). The cost of the molds were as follows: the test device used in Figures 1-5 ($3,615) and the device for solvent bonding used in Figure 2.6 ($2,865). Devices were manufactured on an electric injection molding machine (Toshiba) using Styron® 666D (PS; AmSty), Pro-fax 6323 (PP; M. Holland), and ZEONEX® 480R polymer resin (COC; Zeon Chemicals). The test device (Figures 1-5) was manufactured in PS, PP, and COC from one mold, with the exception of those used in Figures A4 and A5. The closed cell culture device (Figure 2.6) was manufactured in PS. Surfaces on the molds for all devices were polished according to the schematic in Figure A10. PM-F0 (Blue): Non-cosmetic, finish to Proto Labs® discretion;

PM-F1 (Gray): Low-cosmetic, most toolmarks removed; SPI-C1 (Yellow): 600 grit stone; SPI-B1 (Green): 600 grit paper; SPI-A2 (Red): Grade #2 diamond buff.

Device cleaning: The devices were sonicated in 70% ethanol for 30 min using a M2800H ultrasonic cleaner (Branson). The devices were rinsed with fresh 70% ethanol and dried with compressed air. Note that this cleaning protocol is essential for cell viability; devices used directly from Proto Labs® without sonication resulted in poor cell viability as evaluated by cell morphology (likely due to the presence of mold release agents or other surface contaminates on the devices as received).

Solvent bonding to create closed channel devices: The injection molded device, comprised of the channel walls and ceiling (shown in Figure 2.6), was sanded using 1200 grit sand paper. A 0.125 mm PS sheet (Goodfellow) was used for the channel floor. Both components were cleaned following the sonication protocol described above and dried with compressed air. Two cleanroom wipes (TX 609, TexWipe) were placed under the clean device on a programmable stirring hotplate (HS61, Torrey Pines Scientific) set to 37°C. The PS sheet was trimmed to cover the channels (~ 45x70 mm). The PS sheet was set on the hotplate and acetonitrile (ACN) was deposited using a Pasteur pipette. The device was placed on top of the PS sheet with ACN. Excess ACN was removed using cleanroom wipes. A 310x77x6.35 mm aluminum bar (Alcoa) and 10 lb disc weight (CAP Barbell) were placed on top of the device for 5 min. The weight and aluminum bar were removed, and the solvent bonded device was left on the hotplate until the ACN fully evaporated (~15 min). The device was transferred off the hot plate and placed between two room temperature aluminum bars for 20 min. The device along with aluminum bar and weight were placed back onto the hotplate, and the temperature was increased to 80°C. The device was heated for 2 h and left on the hotplate to cool overnight. For the image shown in Figure 2.6A, 12.5 µL of 10% green food coloring (McCormick) was pipetted into each channel using an 8-channel multichannel pipette (Gilson).

3D laser scanning of rectangular channels and cell culture microwells

Device coating

Devices were coated with a gold/palladium (60:40) alloy for confocal profilometry and surface roughness measurements (Figures 2-4). The devices were sputtered with ~16 nm of the alloy in a Quorum Q150R

rotary-pumped sputter coater (Quorum Technologies) as follows: the pressure was reduced to 1e-1 mBar (3 min 43 s) and then to 6-8e-2 mBar (1 min); argon gas was released into the chamber (20 s) until the internal pressure reached 1 mBar; a gold/palladium alloy was sputtered at a current of 20 mA (2 min); the chamber was backfilled with argon gas until it reached atmospheric pressure. The process was repeated once more.

3D laser scanning confocal microscope measurements with VK Viewer

Surface roughness and rectangular channel profile data were obtained using a 3D laser scanning confocal microscope (VK-X150, Keyence). The device was placed on a silicon wafer on the microscope stage. A 10X objective lens (Nikon) was used for all images. In the VK-Viewer software (Keyence) the Z-origin was reset before every scan, and expert mode was enabled. The zoom was set to 1.0X, the upper and lower position of the device were manually set for each scan, and no fixed Z-distance was set. Auto gain was enabled, and the neutral density (ND) filter was set to 10%. Brightness was not adjusted. Measurement settings were as follows: mode: surface profile, area: standard, and quality: high-accuracy. The real peak detection (RPD) was enabled, and the Z pitch was set to 3.00 μm.

Keyence image processing in MultiFileAnalyzer

MultiFileAnalyzer VK-H1XME v. 1.3 (Keyence) was used to analyze the images. In each 3D image representing a rectangular channel, the top surface on either side of the channel was fitted to a horizontal plane to remove natural tilt of the device. The profiles of the rectangular channels were taken and measured for top width, bottom width, and height using point-point analysis. The surface roughness of the square microwells was measured by normalizing the area of the microwell to a horizontal plane. The entire area of the scanned microwell was used for root mean square (RMS) height analyses.

Microwell thickness measurements: The thickness of the microwells in the test device was measured using a 0-25 mm point and anvil micrometer (Fowler), with the micrometer tip placed in the center of the microwell.

Plasma treatment:

The devices were plasma treated using a Zepto plasma treater (Diener Electronic) for cell culture and liquid filling. (Devices used for 3D confocal imaging and surface thickness measurements were not plasma treated.) The chamber was pumped down to a pressure of 0.20 mbar, gas (air) was supplied (4 min, 0.25 mbar), and power enabled (2 min, 200 W).

Cell culture microwells:

Device preparation for fluorescence and phase contrast microscopy

After cleaning (see sonication protocol) and plasma treatment, devices were UV sterilized for 10 min in a Class II biosafety cabinet (Baker). 4 µL of 1% gelatin was pipetted into each microwell and incubated for at least 1 h at 37 °C. The gelatin was aspirated out of the microwell immediately prior to BHPrE1 cell seeding.

Maintenance of cells

BHPrE1 prostate epithelial cells[29] were cultured in DMEM/F12 medium with 5% fetal bovine serum (FBS, VWR), 100 units/mL penicillin and 100 µg/mL streptomycin (Pen Strep, Gibco 15140122), 0.4% bovine pituitary extract (BPE, Hammond Cell Tech), 0.005 µg/mL epidermal growth factor (EGF, Sigma), and 10 µg/mL insulin, 5.5 µg/mL transferrin, 6.7 ng/mL sodium selenite (purchased as 100x ITS, Gibco). Cells were used from passage 25-35. The cells were maintained in standard T25 culture flasks maintained at 37 °C with 5% carbon dioxide.

Cell culture in microwells

BHPrE1 cells were re-suspended at a density of 200 cells per µL. Then 4 µL of the suspended cells were seeded into each 2x2 mm microwell and cultured for 24 h. 5-ethynyl-2'-deoxyuridine (EdU, Invitrogen) was prepared according to the manufacturer's specifications and diluted in cell culture media to 10 µM. 4 µL of the diluted EdU was added to each microwell. After 24 h, the cells were fixed with 4% paraformaldehyde (PFA).

Cell staining and imaging

The fixed cells were permeabilized with phosphate buffered saline (PBS) containing 0.5% Triton X-100 for 20 min and then washed twice with PBS containing 3% bovine serum albumin (BSA). Click-iT reaction

cocktail (Invitrogen) was prepared following the manufacturer's instructions and added to the cells, then incubated at room temperature for 30 min, during which the fluorophore (red, 647 nm) was attached. Cells were washed once with PBS containing 0.1% Triton X-100 (washing buffer), blocked with PBS containing 3% BSA for 1 h, and incubated with alpha tubulin monoclonal antibody (YL1/2, MA1-80017, Thermo Fisher Scientific) at 1:500 dilution overnight at 4°C. Cells were washed three times with washing buffer. The cells were incubated with goat anti-rat secondary antibody (1:200, green, 488 nm, Jackson ImmunoResearch Laboratories) for 1 h at room temperature. The goat anti-rat secondary antibody was removed, a 1:2000 dilution of Hoechst (Invitrogen) was added, and the cells were incubated for 30 min. The cells were washed three times with washing buffer. Fluorescence images were taken using an Axiovert 200 inverted microscope (Zeiss) equipped with an AxioCam 503 mono camera using a 20x (0.40 NA) objective. Phase contrast images were taken on a Primovert microscope (Zeiss) with a MU1403B camera (Amscope). Brightness/contrast adjustments were made uniformly across all images, and the original unadjusted files are included in Figures A7 and A9.

2.9 References

1. S. N. Bhatia and D. E. Ingber, *Nat. Biotechnol.,* 2014, **32**, 760–772.
2. M. L. Kovarik, P. C. Gach, D. M. Ornoff, Y. Wang, J. Balowski, L. Farrag and N. L. Allbritton, *Anal. Chem.,* 2012, **84**, 516–40
3. D. Huh, Y.-S. Torisawa, G. A. Hamilton, H. J. Kim and D. E. Ingber, *Lab Chip*, 2012, **12**, 2156–2164.
4. E. K. Sackmann, A. L. Fulton and D. J. Beebe, *Nature*, 2014, **507**, 181–189.
5. F. An, Y. Qu, X. Liu, R. Zhong, Y. Luo. *Anal. Chem. Insights,* 2015, **10**, 39.
6. T. A. Duncombe, A. M. Tentori, and A. E. Herr, *Nat. Rev. Mol. Cell Biol.,* 2015, **16**, 554–567.
7. E. W. Young and D. J. Beebe, *Chem. Soc. Rev.,* 2010, **39**, 1036–1048.
8. D. J. Guckenberger, T. E. de Groot, A. M. D. Wan, D. J. Beebe and E. W. K. Young, *Lab Chip*, 2015, **15**, 2364–2378.
9. E. W. K. Young, E. Berthier, D. J. Guckenberger, E. Sackmann, C. Lamers, I. Meyvantsson, A. Huttenlochers and D. J. Beebe, *Anal. Chem*., 2011, **83**, 1408–1417.
10. R. Novak, N. Ranu, R.A. Mathies, *Lab Chip*, 2013, **13**, 1468-1471.
11. G. Mehta, J. Lee, W. Cha, Y. Tung, J.J. Linderman, and S. Takayama, *Anal. Chem*., 2009, **81**, 3714-3722.
12. S. Begolo, G. Colas, J. Viovy, and L. Malaquin, *Lab Chip*, 2011, **11**, 508-512.
13. D. B. Wolfe, D. Qin and G. M. Whitesides, *Methods Mol. Biol.,* 2010, **583**, 81–107.
14. D. Duffy, J. McDonald, O. Schueller, G. M. Whitesides, *Anal. Chem.,* 1998, **70,** 4974–4984.
15. A. K. Au, W. Lee, A. Folch, *Lab Chip*, 2014, **14**, 1294–1301.
16. B. C. Gross, J. L. Erkal, S. Y. Lockwood, C. Chen and D. M. Spence, *Anal. Chem*., 2014, **86**, 3240–3253.
17. N. Bhattacharjee, A. Urrios, S. Kang and A. Folch, *Lab Chip,* 2016, **16**, 1720–1742.
18. E. Berthier, E. W. K. Young, and D. J. Beebe, *Lab Chip*, 2012, **12**, 1224–1237.
19. P. M. van Midwoud, A. Janse, M. T. Merema, G. M. M. Groothuis, and E. Verpoorte, *Anal. Chem.,* 2012, **84,** 3938-3944.
20. V. Piotter, T. Hanemann, R. Ruprecht, and J. Haußelt, *Microsyst. Technol.,* 1997*,* **3**, 129-133.

21. B. H. You, D. S. Park, P. Chen, S. D. Rani, D. E. Nikitopoulos, S. A. Soper, and M. C. Murphy, *Nano-Manufacturing Technology; and Micro and Nano Systems*, 2008, **13**, 803-809.
22. Y. Wang, J. Balowski, C. Phillips, R. Phillips, C. E. Sims and N. L. Allbritton, *Lab Chip*, 2011, **11**, 3089–3097.
23. E. W. K. Young, E. Berthier, and D. J. Beebe, *Anal Chem*., 2013, **85**, 44–49.
24. S. Köhler, C. Benz, H. Becker, E. Beckert, V. Beushausen, and D. Belder, *RSC Adv.,* 2012, **2**, 520-525.
25. http://www.protolabs.com.
26. J. Rajaguru, M. Duke, and C. Au, *Int. J. Adv. Manuf. Tech*., 2014, **78**, 31-40.
27. T. S. Hansen, D. Selmeczi, and N. B. Larsen, *J. Micromech. Microeng*., 2009, **20**, 015020.
28. D. S. Kim, S. H. Lee, C. H. Ahn, J. Y. Lee and T. H. Kwon, *Lab Chip*, 2006, **6**, 794–802.
29. M. Jiang, D. W. Strand, S. Fernandez, Y. He, Y. Yi, A. Birbach, Q. Qiu, J. Schmid, D. G. Tang, S. W. Hayward, *Stem Cells*, 2010, **28**, 344–356.
30. D. Ogończyk, J. Wegrzyn, P. Jankowski, B. Dabrowski and P. Garstecki, *Lab Chip*, 2010, **10**, 1324–1327.
31. A. M. D. Wan, A. Sadri, and E.W.K. Young, *Lab Chip*, 2015, **15**, 3785-3792.
32. C. M. Carney, J. L. Muszynski, L. N. Strotman, S. R. Lewis, R. L. O'Connell, D. J. Beebe, A. B. Theberge, and J. S. Jorgensen, *Biol Reprod.,* 2014, **91**, 85.
33. B. P. Casavant, E. Berthier, A. B. Theberge, J. Berthier, S. I. Montanez-Sauri, L. L. Bischel, K. Brakke, C. J. Hedman, W. Bushman, N. P. Keller and D. J. Beebe, *Proc. Natl. Acad. Sci. U. S. A.*, 2013, **110**, 10111.
34. L. J. Barkal, A. B. Theberge, C. -J. Guo, J. Spraker, L. Rappert, J. Berthier, K. A. Brakke, C. C. C. Wang, D. J. Beebe, N. P. Keller, E. Berthier, *Nat Commun*., 2016, **7**, 10610.

Chapter 3 | Interfacial Tension Driven Open Droplet Microfluidics

Reproduced in part from J. W. Khor, U. N. Lee,* J. Berthier, E. Berthier,[#] A. B. Theberge,[#] "Interfacial tension driven open droplet microfluidics." bioRxiv, https://doi.org/10.1101/2021.07.29.454194.*
** Equal contribution*
[#]Co-corresponding authors

JK and UNL conducted the experiments, JK and JB developed the theory, EB and ABT supervised and al authors interpreted the results.

Abstract: We developed an open channel droplet microfluidic system that autonomously generates droplets by leveraging competing hydrostatic and capillary pressure. With only our open channel polytetrafluoroethylene (PTFE) device, pipettes, and commercially available carrier fluid, we produce hundreds of microliter droplets; tubing, electronics, or pumps are not required, making droplet technology feasible for research labs without external flow generators. Furthermore, we demonstrated conceptual applications that showcase the process of droplet generation, splitting, transport, incubation, mixing, and sorting in our system. Unlike conventional droplet microfluidics, the open nature of the device enables the use of physical tools such as tweezers and styli to directly access the system; with this, we developed a new method of droplet sorting and transfer that capitalizes on the Cheerios effect, the aggregation of buoyant objects along a liquid interface. Our platform offers enhanced usability, direct access to the droplet contents, easy manufacturability, compact footprint, and high customizability.

3.1 Introduction

We show for the first time droplet generation by an open microfluidic channel using passive forces alone; we also demonstrate downstream manipulations that are uniquely enabled by the open nature of the system. This work has potential to open new avenues in droplet microfluidics, a field which has grown immensely in the past decade.[1-11] Droplet microfluidics is an attractive technology because it is high throughput, miniaturizes chemical and biological processes, reduces reagent waste, and enables the use of precious or expensive reagents. The microliter to picoliter droplets act as chambers to conduct biological or chemical analyses and have many important applications in DNA sequencing, directed evolution, materials chemistry, and chemical reactions.[1-11] Additionally, droplet manipulations such as sorting,

mixing, and splitting are empowering for expanding the versatility and potential applications of droplet microfluidics.[1, 2, 5-11]

In our system, we autonomously generate droplets in an open channel without pumps or tubing by leveraging the inherent hydrostatic pressure difference between two immiscible fluids (the fluorinated carrier phase and aqueous phase), capillary pressure, and spontaneous capillary flow (SCF) — flow induced by capillary action.[12-17] In our autonomous droplet generating system, the top side of the channel is exposed to air, rather than being enclosed by a ceiling, which gives access to the channel where conventional droplet microfluidics with enclosed channels does not. Open channels are advantageous because a researcher can directly pipette into the channel or add/retrieve droplets, solid objects such as magnetic beads, or tissue samples as they wish. Previous work in open droplet microfluidics includes the analysis of different modes of immiscible fluid plug flow in an open channel with various solvents as carrier fluid.[18] Droplet manipulations (splitting, incubating, and merging) in an open channel were investigated where the droplets were pipetted by hand into the channel at specified locations prior to addition of the carrier fluid.[19] Additionally, liquid handling systems have been used with open systems to keep flow rates constant for investigations of shear on cells in a hanging droplet[20] and to generate droplets in open channels with syringe pumps.[21] Our open channel droplet generator presented here is distinct from this prior work in that it shows, for the first time, we demonstrate autonomous generation of droplets from an open capillary flow without the direct actuation of a pipette to generate each droplet. This feature is particularly complex as typical passive pumping or capillary flows do not produce the pressures or shear forces sufficient to generate traditional shear-based droplet generation. Furthermore, we demonstrate this droplet generation with much more traditional and functional biphasic liquids such as HFE-500 fluorinated oil, as opposed to the traditional organic solvents that have been more typical for open biphasic flows previously.[18, 19] The use of fluorinated oils is particularly important for compatibility with biological experiments.[2, 5, 7, 8, 22, 23] The importance of manipulations of droplets for cell biology was highlighted in Soitu *et al.*[1, 24-27] and Li *et al.*[1, 28-31] where droplets were formed under an immiscible phase by segmenting aqueous solution with a physical stylus and simple pipetting in an open system. While Soitu *et al.* also developed a method to generate

droplets in an open system, our system achieves similar droplet size (100 nL) without the use of pumps and tubing.[1, 24-27] Other methods to generate droplets using pipettes include simple agitation of a biphasic solution either with or without cavity-containing microparticles to create an emulsion of droplets in an immiscible phase.[1, 32, 33] Additionally, there are methods of autonomous droplet generation utilizing a closed channel but they have limited downstream analysis and manipulation capabilities.[34, 35]

Herein we describe our autonomous droplet generation system that achieves 100 nL - 120 µL size droplets in an open microfluidic channel. We developed a theoretical model to determine the conditions for droplet formation which is derived from the difference between hydrostatic pressure and capillary pressure across the aqueous plug. Both the experimental results and theoretical model show that interfacial tension, contact angle, and constriction width play critical roles in droplet generation. Thus far our open microfluidic system has only been used to generate droplets containing water and culture media, and additional work is needed to optimize the system with droplets containing cells and other biological materials. In fact, the goal of future studies is to implement open droplet technology with biological samples. As a first step toward this goal we focused on the physical parameters needed for droplet generation and developed a suite of droplet manipulation techniques that capitalize on the open nature of our devices, including novel methods for moving droplets with a specialized stylus or tweezers to sort and transfer droplets within a device or into another device or well plate. Applications best-suited for our medium-throughput droplet generator will leverage the ability to easily manipulate hundreds to thousands of droplets, scaling droplet generation through parallelization without pumps if needed.

3.2 Autonomous droplet generation in an open microfluidic channel

Our open droplet generation platform demonstrates the ability to autonomously generate droplets at 2 droplets/second without intervention, and the open surface nature of our channel provides direct access to manipulate droplets (Figure 3.1). There are five regions in the device; the origin of flow is at the (1) inlet reservoir which leads to the (2) converging region, followed by the (3) narrow constriction, (4) diverging region, and (5) outlet reservoir (Figure B1). The operation of the device is simple; the aqueous solution is pipetted into the converging region creating an aqueous plug. The anterior end of the plug meets the narrow

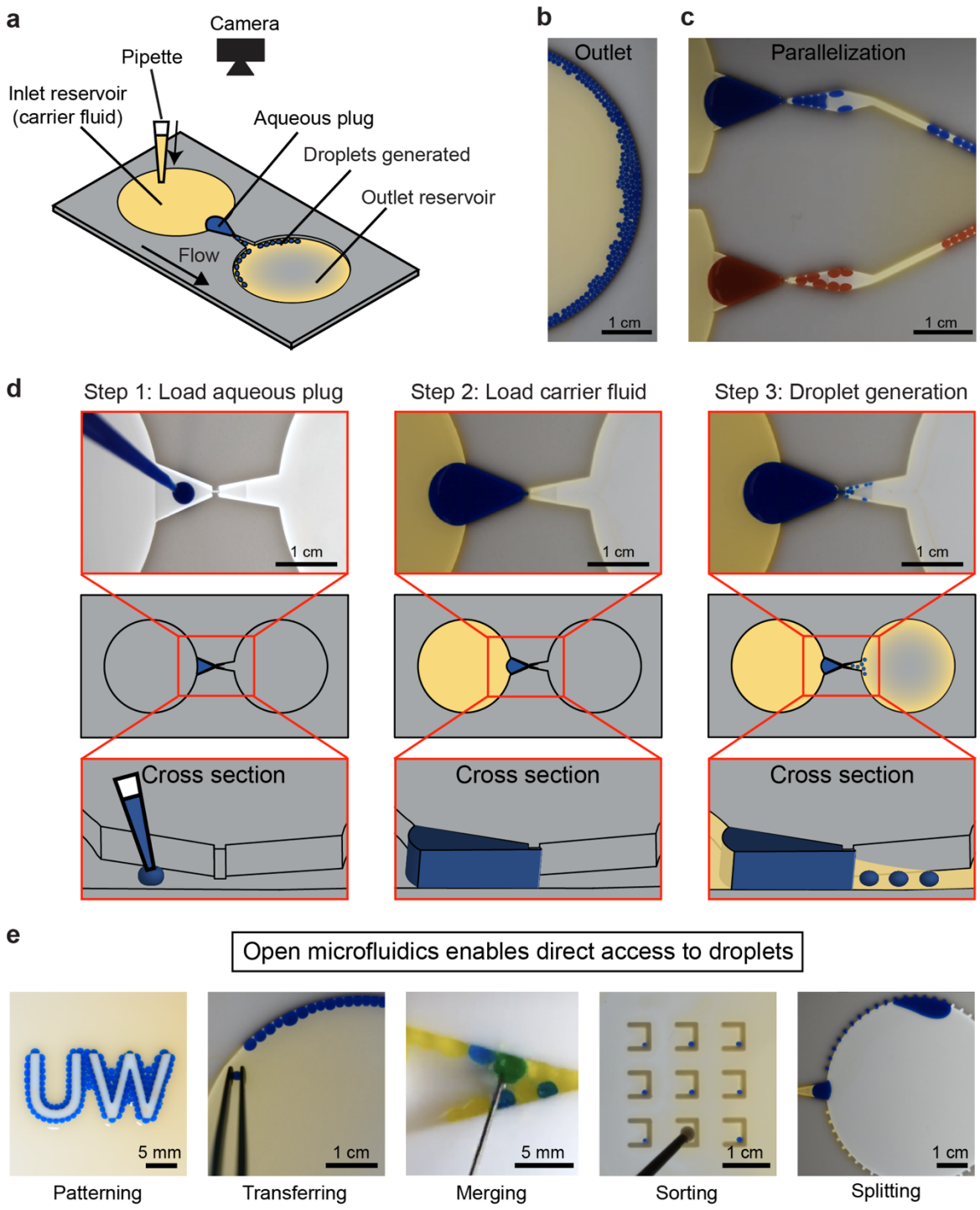

Figure 3.1. Device design, workflow, and manipulation of droplets. (A) Schematic representation of the device, (B) image of generated droplets in the outlet reservoir, and (C) droplets generated in parallel. (D) Workflow for droplet generation using passive forces derived from pressure (hydrostatic pressure and capillary pressure) in an open device. (E) Droplet manipulations downstream.

constriction and the plug is in full contact with the channel walls (Figure 3.1D, left). Next, the carrier fluid, a fluorinated oil, is pipetted in the inlet reservoir to establish a hydrostatic pressure that pushes the aqueous plug into the narrow constriction (0.2 mm - 3 mm in width) (Figure 3.1D, middle). As the anterior portion of the aqueous plug exits the narrow constriction, it pinches off into small droplets in the diverging region and flows to the outlet reservoir (Figure 3.1D, right). The angles of the converging and diverging region (45° and 20° respectively) were found to generate the most consistent and monodisperse droplets. Furthermore, a pair of square protrusions forms the narrow constriction which creates a large capillary pressure to oppose the hydrostatic pressure of the carrier fluid at the inlet reservoir. Hydrostatic pressure is governed by the carrier fluid height (determined by the dimensions of the device) and density, while capillary pressure is governed by interfacial tension, contact angle, and meniscus radius of curvature. As carrier fluid fills the inlet reservoir the hydrostatic pressure increases. At the narrow constriction and converging-diverging region there is a 0.2 mm tall step with grooves on both sides to allow carrier fluid to flow past the aqueous plug and prewet the channel walls prior to droplet generation. The low contact angle of the carrier fluid on the polytetrafluoroethylene (PTFE) channel surface enables prewetting of the channel walls by spontaneous capillary flow (SCF) which was found to be essential for continuous droplet generation.

One critical breakthrough from our prior work is the use of PTFE as the channel material. Previously, in our open channel, channels were fabricated from poly(methyl methacrylate) (PMMA) and could only transport water droplets with organic solvents which is not ideal for applications of droplet microfluidics because organic solvents are often cytotoxic and known to remove small molecules from the droplets.[18, 19] In other words, using a carrier fluid that is not toxic and possess desirable interfacial properties was essential to furthering biological applications of our technology. The wetting properties of fluorinated oil, HFE 7500, on PTFE and the high contact angle of the aqueous plug allowed for droplet generation and manipulation (Figure 3.1) to occur in our channel. Fluorinated oils are ideal for life science applications in droplet-based microfluidics because of their biocompatibility—they have been used in applications ranging from human cell culture to digital droplet polymerase chain reaction (ddPCR).[1-11, 22]

3.3 Condition for droplet generation

Droplet generation occurs when the aqueous plug overcomes the difference between hydrostatic and capillary pressure which pushes it into the narrow constriction. To note, a non-wetting plug should move spontaneously away from convergent geometries when no external forces of parallel direction are applied, and in our channel design, the hydrostatic pressure resulting from the carrier fluid is able to counteract this tendency.[13] Based on empirical observation from high-speed videos, the anterior portion of the aqueous plug is initially settled at the narrow constriction. As the anterior portion of the aqueous plug advances into the narrow constriction (plug advancement phase) it forms a bulbous shape (bulbing phase). Next, a liquid thread is formed (thread formation phase in Figure 3.2A and red arrow depicting the thread in Figure 3.2B), and the liquid thread diameter decreases until it pinches off and droplet formation occurs (pinch off phase). Figure 3.2B shows the droplet formation process for various surfactant concentrations, c, and constriction widths, *w*. We observed that the phases of the droplet formation process are nearly identical across the various surfactant concentrations and constriction widths used in this study (Figure 3.2B). We also observe

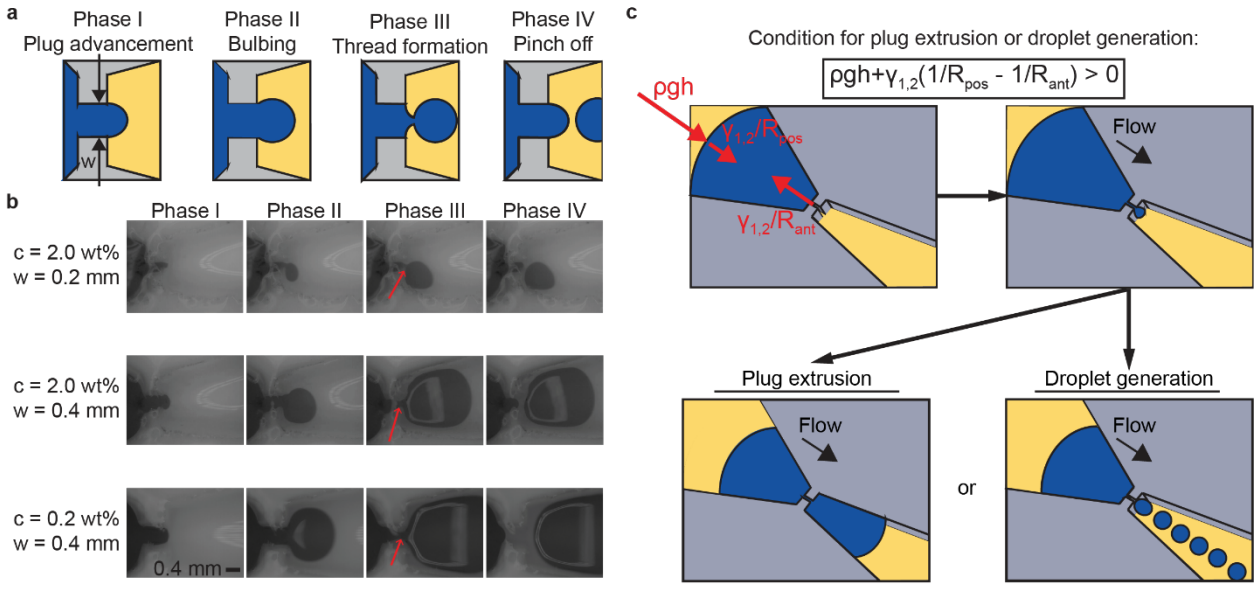

Figure 3.2. Snapshots of droplet formation with a high-speed camera and geometry of the open channel constriction for droplet generation. (A) Schematic of the phases observed during droplet formation. (B) Droplet formation in the constriction at various constriction width and surfactant concentration. Red arrow depicts the thread formation. (C) Hydrostatic pressure overcoming capillary pressure resulting in the aqueous plug being extruded or generating droplets at the constriction.

that the constriction geometry and surfactant concentration is a determining factor in the final droplet volume generated. For the aqueous plug interface to extend past the narrow constriction, the hydrostatic pressure, ρgh at the posterior side of the plug must overcome the capillary pressure, $\gamma_{1,2}(1/R_{pos} - 1/R_{ant})$ (Figure 3.2C). Then, two possible outcomes occur: plug extrusion or droplet generation. We define plug extrusion as the entire aqueous plug passing through the constriction and sometimes breaking into two or three segments when exiting the diverging region. Droplet generation is a consistent generation of droplets pinching off from the aqueous plug with a relative standard deviation in volume of 5% - 7%. The pressure difference when the aqueous plug interface extends past the narrow constriction is:

$$\rho gh + \gamma_{1,2}\left(\frac{1}{R_{pos}} - \frac{1}{R_{ant}}\right) > 0 \qquad \text{(Eq. 2)}$$

where g is the gravitational acceleration, $\gamma_{1,2}$ is the interfacial tension between carrier fluid and aqueous plug, ρ is the carrier fluid density, R_{pos} is the radius of curvature of the posterior plug interface, and R_{ant} is the radius of curvature of the anterior plug interface. The left-hand side of Eq. 2 must be greater than 0 for the aqueous plug interface to extend past the narrow constriction.

By rearranging the pressure difference involving the hydrostatic pressures and capillary pressures, the condition for the aqueous plug extrusion or droplet generation is:

$$w > \frac{2\gamma_{1,2}|coscos\,\theta_{1,2,s}|}{\rho gh} \qquad \text{(Eq. 3)}$$

where w is the constriction width, $\theta_{1,2,s}$ is the contact angle between aqueous plug, carrier fluid, and channel wall, and h is the carrier fluid height. Based on experimental observation, the aqueous plug height is equal to the carrier fluid height. For the theoretical derivation, please see Appendix B Note 1.

We display the theoretical threshold for when the aqueous plug extrusion or droplet generation occurs in a regime map (Figure 3.3A dashed line, from Eq. 3) at varying interfacial tension, contact angle, constriction width, and constriction height. In Figure 3.3A, we observed empirically that there exists a well-defined region (teal shaded region) where droplet generation occurs when constriction width is small ($w \leq 0.6$ mm) and the condition in Eq. 3) is met (discussion on units for Eq. 3) can be found in Appendix B

and Figure B2). In the droplet generation region (teal shaded region), the constriction width w, the channel height h, interfacial tension $\gamma_{1,2}$, and contact angle $\theta_{1,2,s}$ are the four factors that determine the volume of the droplets formed when carrier fluid density remains constant. The $\gamma_{1,2}$ and $\theta_{1,2,s}$ is varied by the concentration of the surfactant, c. We observed that at a constriction width of 0.2 mm, when $\gamma_{1,2}$ and $\theta_{1,2,s}$ increases (due to lowering fluorinated surfactant (FS) concentration from 2.0 wt% to 0.2 wt% or lower), the anterior portion of the aqueous plug cannot enter the narrow constriction and no plug extrusion occurs (Figure 3.3B). However, the aqueous plug can extrude from the narrow constriction if the constriction width increases to 0.4 mm at a FS concentration, c, of 0.2 wt%. This observation matches Eq. 3 and the regime map at Figure 3.3A; when $\gamma_{1,2}$ and $\theta_{1,2,s}$ increases, the minimum width that allows plug extrusion is larger as well. Note that plug extrusion is possible without droplet generation (w = 3.0 mm, c ≥ 0.2 wt%). At the highest $\gamma_{1,2}$ and $\theta_{1,2,s}$ (0.0 wt% FS), the anterior portion of the aqueous plug cannot enter the narrow constriction for any of the constriction width dimensions tested, thus plug extrusion does not occur (Figure 3.3B, consistent with the phase diagram in Figure 3.3A).

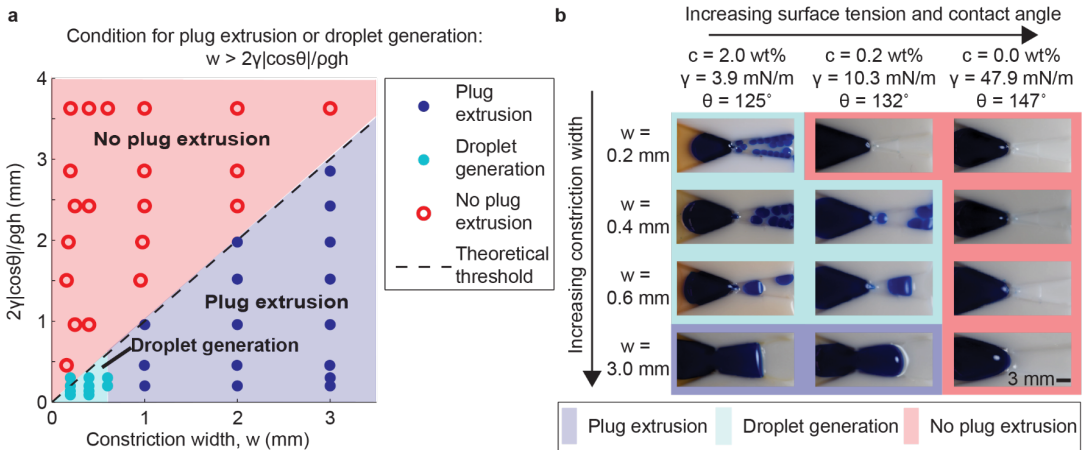

Figure 3.3. Conditions for plug extrusion and droplet generation. (A) Regime map of plug extrusion and droplet generation with theoretical threshold (dashed line per Eq. 3); experimental data points of plug extrusion (purple filled circle), droplet generation (teal filled circle), and no plug extrusion (red open circle). The regions, predicted by the theoretical model, are plug extrusion (purple shaded region), droplet generation (teal shaded region), and no plug extrusion (red shaded region). Full table of parameters available in Table B1. (B) Montage of plug extrusion and droplet generation when varying constriction width, fluorinated surfactant concentration (c, wt%), interfacial tension $\gamma_{1,2}$, and contact angle $\theta_{1,2,s}$.

Figure 3.4 shows the generated droplet volume as a function of constriction width, surfactant concentration, constriction length, and constriction height (data point presented as mean ± SD, n ≥ 90). Figure 3.4A depicts the effect of surfactant concentration (c = 2 wt% and c = 0.2 wt%) and constriction width (w = 0.2 mm and w = 0.4 mm) on generated droplet volume. The droplet volume generated increases with increasing constriction width w and decreasing surfactant concentration (interfacial tension $\gamma_{1,2}$ and contact angle $\theta_{1,2,s}$).

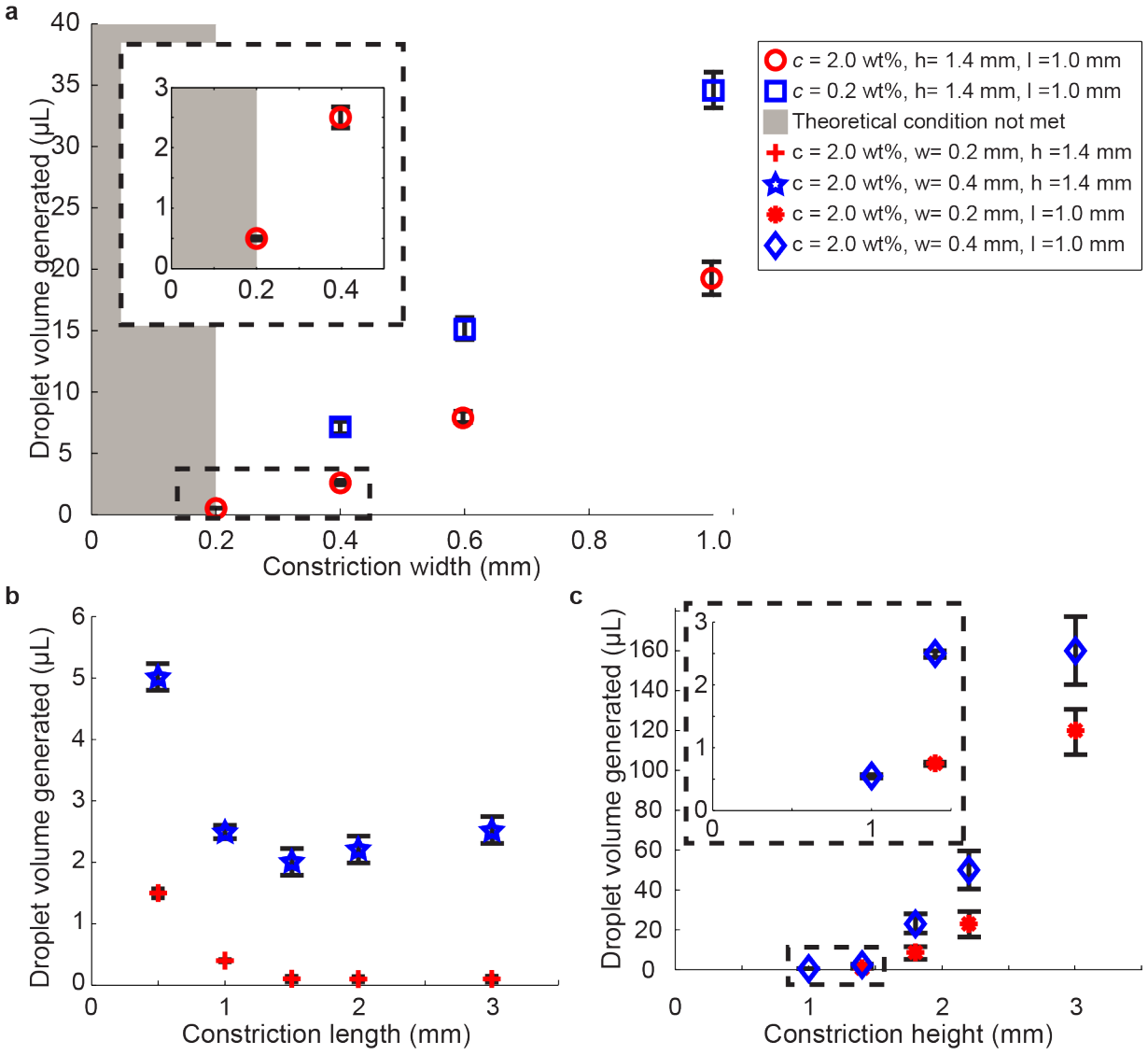

Figure 3.4. Plot of generated droplet volume as a function of (A) constriction width and surfactant concentration, (B) constriction length, and (C) constriction height. The shaded gray region is where the condition for the aqueous plug extrusion or droplet generation in equation (2) is not met. (Data point presented as mean ± SD, n ≥ 90). Table of parameters available in Table B2.

Similarly when varying constriction length, l at w = 0.2 mm and w = 0.4 mm, we found that the generated droplet volume decreases as constriction length increases (Figure 3.4B). However, it is important to note that the standard deviation of the generated droplet volume is much larger when the constriction length is larger than 1 mm. When varying constriction height, h at w = 0.2 mm and w = 0.4 mm, we found that the generated droplet volume increases as constriction height increases (Figure 3.4B).

Overall, the smallest droplet volume generated in our experiments is 0.52 ± 0.025 μL and w = 0.4 mm is 2.39 ± 0.175 μL. The relative standard deviation of our droplet generation method ranges between 5% and 7% while conventional methods range between 1% and 3%[36, 37] which shows that the monodispersity of our system is relatively close to conventional methods, with room for improvement. We believe the relative standard deviation can be reduced if we have better control of maintaining relatively constant hydrostatic pressure, a focus of future redesigns. We also note that the physics underlying the droplet formation process is scalable to smaller length scales, therefore smaller droplet volumes will be achievable in future work if alternative fabrication processes such as advanced CNC milling or cleanroom fabrication processes are used to create devices with smaller constriction widths. Here, we chose 0.2 mm as the minimum constriction width due to the limitations of our current CNC milling process.

3.4 Downstream droplet manipulation in open microfluidic devices

Droplet manipulation is essential for utilizing droplet microfluidics to study biology and chemistry. We demonstrate droplet manipulations to present the possibilities of conducting future biological and chemical studies with this device. In open systems, contamination and evaporation may be problematic if not controlled. Methods to address evaporation and contamination such as secondary containment and sacrificial liquid droplets[38] or wells have been successfully employed with primary human samples.[39] The open surface of the device enables us to create new methods to physically move the droplets such as using specialized tweezers or a needle to reach into the device and move or mix targeted droplets chosen in real-time at the discretion of the researcher. We use these manipulations for chemical reactions followed by droplet sorting.

Droplet transport and droplet sorting is an integral component of droplet microfluidics workflows. We developed a new method to selectively transfer single droplets to locations both on and off the open droplet generating device by picking them up with PTFE-coated tweezers or moving them with a PTFE stylus. The PTFE-coated tweezers and styli transport droplets laterally by utilizing the Cheerios effect, which is the phenomenon of multiple objects aggregating due to the objects deforming the liquid interface (Figure 3.5A).[40-44] The PTFE-coated tweezers and styli are placed at the surface of the carrier fluid, causing

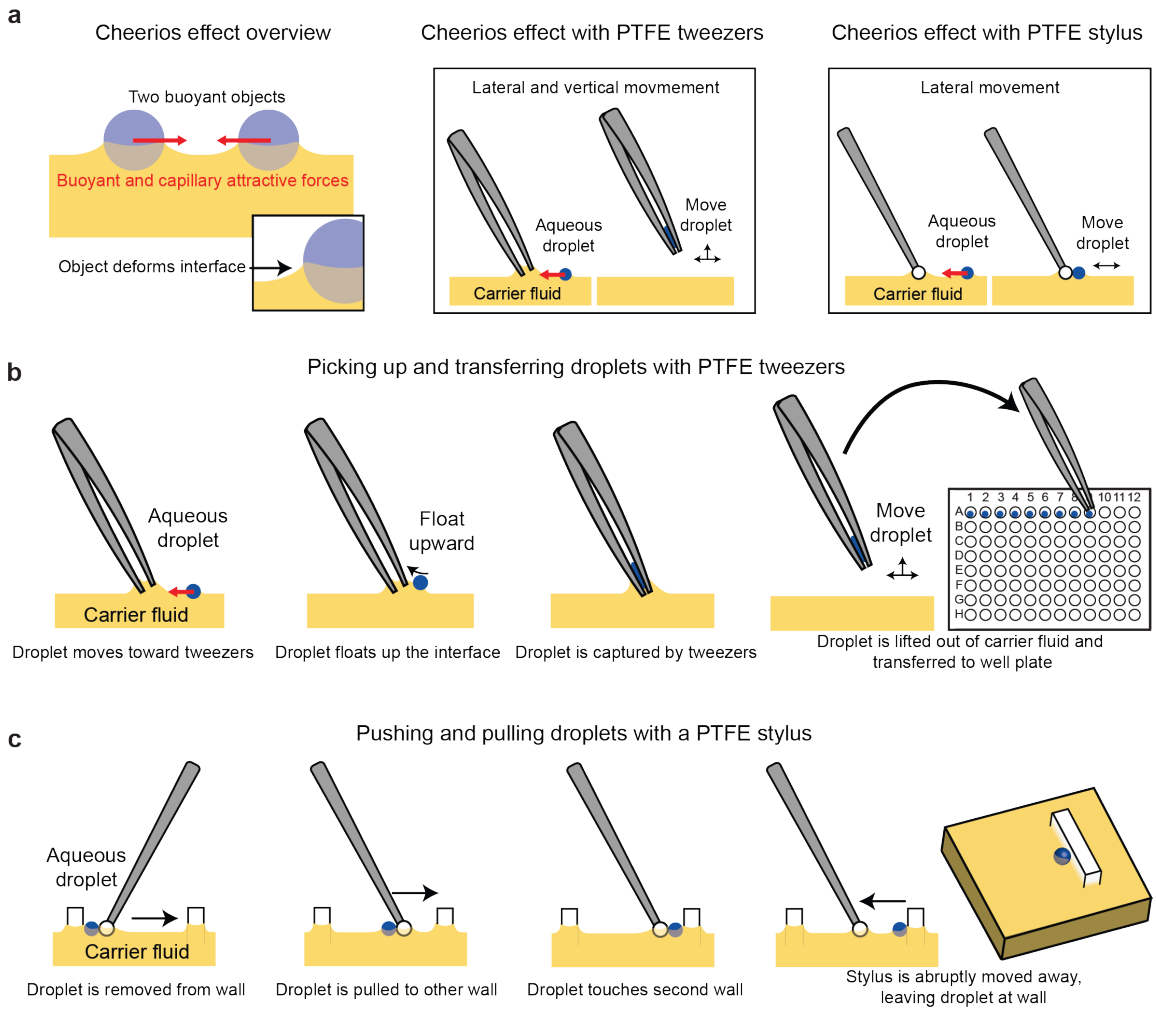

Figure 3.5. The Cheerios effect enables droplet transport. (A) Two neighboring buoyant objects aggregate due to the Cheerios effect.[42, 44] The buoyant object deforms the surface of the liquid resulting in a rising interface, and when a second buoyant object is near it tends to float up the rising interface. The tweezers and PTFE stylus behave similarly because they also deform the surface so the droplets tend to aggregate towards them. (B) Picking up droplets from an open microfluidic device and transferring them to another location (e.g., well plate) with PTFE-coated tweezers. (C) Transporting droplets from one wall to another with a PTFE ball mounted on a stylus.

the carrier fluid to wet the tweezers or stylus and form a rising interface. The droplets are buoyant and when they are near the meniscus created by the tweezers or stylus they then move toward the upward rising fluid interface. Additionally, once the droplet is captured between the tweezers, the droplet rises up the tweezers due to the tendency for droplets to move towards divergent geometries (Figure 3.5B).[13] This allows droplets to be picked up and transferred to another location (e.g., well plate). To detach the droplet from the tweezers or stylus the user can abruptly move it away from the droplet which causes detachment due to inertia. Further, walls or other features (Figures 3.5C, 3.6B, and 3.6C) have menisci which enables droplets to again move up the rising interface to rest on the wall.

PTFE tools are important for droplet transport because the PTFE prevents the aqueous droplet from strongly adhering to the tweezers, facilitating droplet release. Using a similar mechanism, we use a stylus with a PTFE bead adhered to the tip to gently move droplets around the reservoir for sorting and patterning droplets (Figure 3.6B and 3.6C). To summarize, the PTFE stylus enables lateral droplet transport and the PTFE-coated tweezers enables both lateral droplet transport and vertical droplet transport (i.e., picking up droplets). In future work, this approach could be used to sort droplets based on a reaction outcome or transfer droplets to a different part of a chip for further use in analysis or reactions.

While we focused on moving individual droplets to highlight the ability to move droplets selectivity, this method can be multiplexed using an array of styli (for example, a three-pronged stylus could be used to move three droplets at once from the columns of the array similar to Figure 3.6C). The direct access to the droplets is unique to our open channel systems and allows users to directly extract and/or manipulate the contents of the channel. This is enabling for users who cannot rely on power-heavy solutions in conventional droplet microfluidics like acoustophoresis, electrophoresis, and electrowetting-on-dielectric (EWOD) or users who would like the flexibility to manipulate droplets at any point in their device, without the need to pre-pattern electrodes.[10]

For applications requiring automation, this method could be automated by mounting the stylus on a robotic XYZ controller interfaced with a fluorescent or colorimetric readout in the droplets to facilitate sorting based on a chemical/biochemical readout. The flexibility to move droplets on demand—both on-

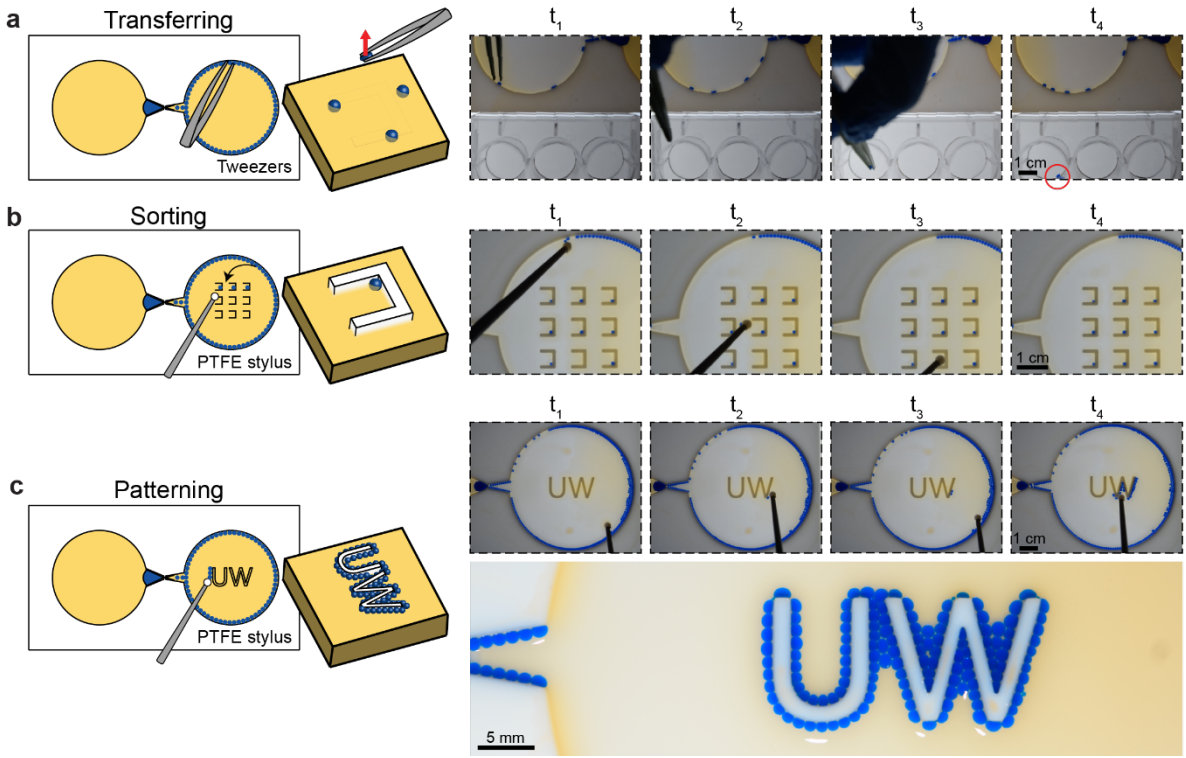

Figure 3.6. Open surface of the open microfluidic channel enables on-demand direct manipulation of droplets. (A) Selectively retrieving droplets from an open microfluidic device and transferring them to a well plate with PTFE-coated tweezers. (B) Sorting droplets into individual chambers with a PTFE ball mounted on a stylus. (C) PTFE stylus is used to transfer droplets to the "UW" pillar.

and off-chip—shows great promise for being able to conduct multistep chemical and biological experiments and incorporating analytical readouts that are best implemented outside of the original microfluidic chip embodiment.

In Figure 3.6C, the generated droplets are patterned by transporting them toward the "UW" feature using a PTFE bead to outline the feature. It is important to note that droplets were transported to sharp corners of the "W" with ease using the PTFE bead. In contrast, traditional droplet microfluidics would require pumps and valves to change the trajectory of the droplets. Furthermore, our channel design is not constrained by requiring prior knowledge of the location to which the droplets will be transported. This allows our channel design to be modular by being able to continuously upgrade or add new features (e.g., replacing "UW" feature with another feature) directly on the channel. Open microfluidics can be leveraged

to make droplet studies user-friendly, customizable, and adaptable for integration of physical probes and tools downstream.

The ability to take small aliquots of a droplet after it is generated is useful for downstream analysis or processing steps, particularly when working with small volumes of precious reagents.[1-11] We demonstrated that we can split smaller droplets off from a large aqueous plug with a crenulation feature along the outlet reservoir wall (Figure 3.7A). In this case, the constriction allows aqueous plug to extrude and flow along the crenulations. As the plug travels along the crenulations via SCF, it fills the crenulation; as the posterior end of the large plug fully passes the crenulation it shears off leaving the crenulation filled with a small droplet. The droplets in the crenulations can then be retrieved with a pipette.

In Figure 3.7B, two droplet merging is demonstrated by disrupting the interface of the droplets using a simple needle. The needle is moved back and forth between the two droplets to disrupt their interface resulting in their merging. In future work, the merging step could also be automated using a needle mounted on an XYZ controller as described for the droplet transport with tweezers and styli mentioned above. This merging technique with the automated system makes it comparable to prior droplet fusion methods (such as electrofusion or fusion based on electrowetting on dielectric), which often require the placement of specific components (e.g., electrodes) in the device design.[1, 10] Our new fusion method allows users to induce fusion on demand at any location in the open device; the location need not be decided prior to the experiment.

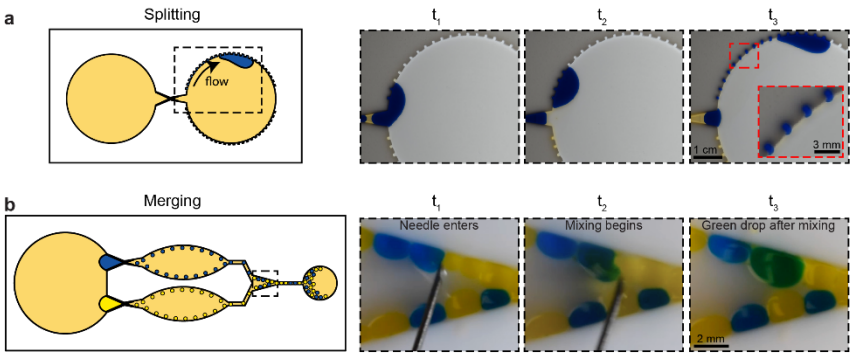

Figure 3.7. Splitting and merging droplets in an open droplet generator. (A) Crenulations along the outlet reservoir capture portions of an aqueous plug, and as the plug passes the crenulation, a small droplet splits off and remains in the crenulation. (B) A yellow and blue droplet are merged by mixing with a needle to form a green droplet.

3.5 Sorting reacted products in droplets

Droplet merging and sorting opens up applications for chemical reactions, biochemical assays, and other multi-reagent processes.[45] Selective droplet merging is demonstrated in Figure 3.8 using droplets of KSCN and $Fe(NO_3)_3$ mixed with blue dye for visualization. Droplets of the two reagents are formed using two parallel open-channel droplet generators. Then, two droplets are randomly selected from the outlet reservoir

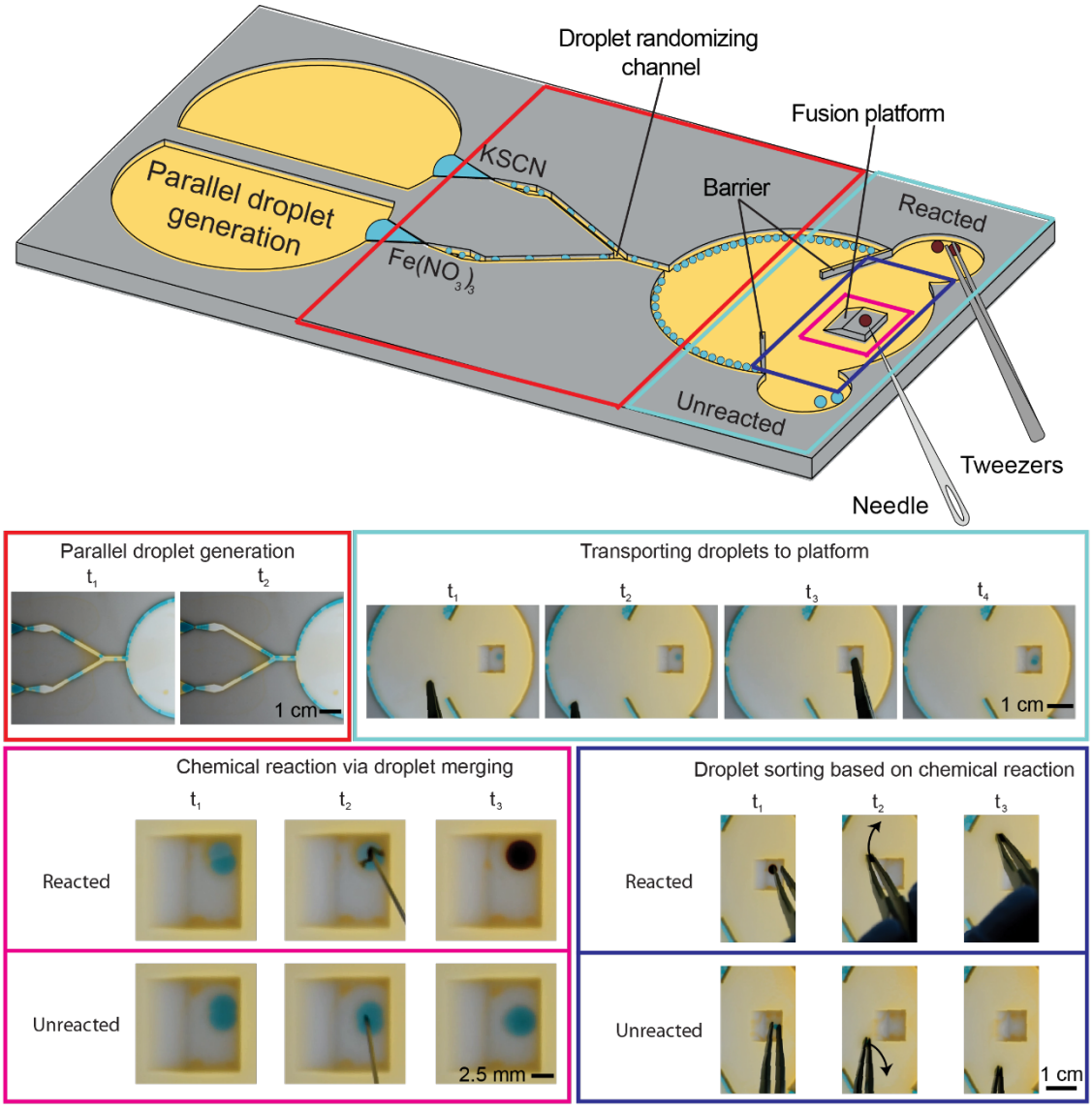

Figure 3.8. Model chemical reaction using capillary-driven open droplet microfluidics. Droplets containing KSCN and $Fe(NO_3)_3$ are generated in parallel. Two droplets are randomly selected and moved to the fusion platform with tweezers. The droplets are merged with a needle; if a colored complex ($Fe(SCN)_3$) forms, the droplet is sorted to the reacted chamber; droplets without $Fe(SCN)_3$ are sorted to the unreacted chamber.

and transported to a platform with a pair of PTFE-coated tweezers (yielding three possible combinations: two droplets containing KSCN, two droplets containing $Fe(NO_3)_3$, or a droplet containing KSCN and a droplet containing $Fe(NO_3)_3$). On the platform, the droplets are merged by disrupting the interfaces of the droplet pair with a needle. When a droplet containing KSCN and a droplet containing $Fe(NO_3)_3$ merge, they change color from blue to red due to the formation of $Fe(SCN)_3$. Merged droplets are then sorted to chambers categorized by reacted and unreacted droplets using PTFE-coated tweezers.

The purpose of this proof-of-concept workflow is to demonstrate the ability to perform a reaction and sort droplets based on "hits" (in this case droplets containing the reaction product $Fe(SCN)_3$). This suggests the potential for conducting droplet sorting tasks in applications like single cell encapsulation, directed evolution of enzymes, and process optimization of synthetic reactions to synthesize small molecules or novel materials.

3.6 Conclusion

Overall, our open droplet microfluidic system is the first of its kind that can autonomously generate droplets by utilizing hydrostatic pressure and capillary pressure. Further, our open system enables manipulation of droplets (including patterning, transferring, splitting, merging, and sorting) due to unobstructed access to the droplets along the entire length of the device. This offers opportunities that simply are not possible in closed channel devices, where the ceiling obstructs access. We acknowledge that there are limitations of our system —chiefly, the number of droplets generated (2 droplets/second) in our device is not at the level of high throughput droplet microfluidic systems where droplets are generated at thousands of droplets per second. Thus, we envision applications of our method will capitalize on aspects uniquely enabled by the open channel (such as the ability to manipulate droplets with implements like tweezers or a needle and the ability to add and remove solid objects like beads or pieces of tissue) that are suited for medium-throughput experiments (hundreds to thousands of droplets in total). Additionally, the ability to parallelize the channel without adding pumps to drive the flow allows for the droplet generation to be scaled up without adding additional equipment for each new droplet generator. Additionally, this method is currently limited to use with PTFE. Although many plastics were tested (i.e., PMMA,

polystyrene, polypropylene, etc.) with this channel design, only PTFE was successful in droplet generation with fluorinated oil carrier phases due to its high hydrophobicity. Fortunately, PTFE is a biocompatible material and is suitable for biological applications and it has excellent solvent compatibility for chemical applications.[46] Our method opens up numerous areas for future work—both on biological and chemical applications and in further understanding the physics underlying droplet formation and droplet transport via the Cheerios effect.

3.7 Materials and methods

Channel design and fabrication. The channels were designed in Solidworks (Dassault Systemes SE) and postprocessed in Fusion 360 (Autodesk, Inc.). Then, they were fabricated out of 3.2 mm thick PTFE (McMaster-Carr Supply Co.) on a Datron NEO mill (Datron Dynamics Inc.). After the channels were milled, they were rinsed with deionized water (DIW), sonicated in 70% ethanol for 30 min, and then rinsed again with DIW. Finally, the channels were dried with compressed air.

The channel height is 1.6 mm, and the width of the narrow constriction ranges between 0.2 mm and 3.0 mm. There is also a platform with a height of 0.2 mm at the narrow constriction and converging-diverging region to allow the aqueous plug to be pinned at the constriction entrance to produce consistent droplet generation. The channel has a square cross section. The converging part of the tapered channel is 45°, and diverging is 20° as these angles were found to be the best at generating monodisperse droplets consistently. The square protrusions that form the channel constriction are 1 mm wide. CAD files and engineering drawings (Appendix B Note 4, Figures B3-B6) are included in Appendix B.

General reagents. Carrier fluids used were pure HFE 7500 (The 3M Co.), HFE 7500 with 0.002 wt%, 0.02 wt%, 0.2 wt%, and 2 wt% Rhodamine fluorosurfactant (RAN Biotechnologies Inc.). The Rhodamine fluorosurfactant (FS) is a mix of fluorosurfactant 008FS (008-FluoroSurfactant) and Rhodamine-functionalized fluorosurfactant Rhod-FS (FS-Rhodamine) (FS is a mix of 008FS and Rhod-FS with weight ratio of 3:1 respectively). The aqueous phase, DIW, is mixed with blue food dye (McCormick Corp.).

Image acquisition setup. A Nikon-D5300 DSLR camera attached to a jig with adjustable distance was used to record the experimental results at the top view of the channel and at a frame rate of 30 fps. For the

high-speed video in Figure 3.2B, a Chronos 1.4 high-speed camera (Kron Technologies Inc.) was installed on a stereoscope (United Scope LLC) to record the droplet generation at 2577 fps.

Droplet generation. A 180 μL DIW plug containing food dye was pipetted on the platform in the channel and then 2 mL of carrier fluid was pipetted into the inlet reservoir of the channel to generate water droplets ranging from 0.52 μL to 34.55 μL (see Figure 3.1D). Generated droplet volume takes 1 – 2 minutes to stabilize and generate consistent droplet volume.

It was found that droplet generation is initiated faster when the channel is placed at a slight incline of 3°. Placing the channel on an incline did not result in a significant change in the generated droplet volume. Thus, in the proof of concept demonstrating the sorting of reacted products in droplets (Figure 3.8), the channel was placed at an incline.

Contact angle and interfacial tension measurements. Contact angles and interfacial tension values reported in Figure 3.3 were measured on a Kruss Drop Shape Analyzer model DSA025 (Kruss GmbH). Contact angles of the aqueous droplet on the PTFE substrate were measured using the sessile droplet method. When needed, the sessile droplet method is conducted with the sessile droplet submerged in a second liquid to measure the contact angle in a quartz cuvette. In this experiment, the droplet was DIW with blue dye submerged in HFE7500 at various FS concentrations (0 wt%, 0.002 wt%, 0.02 wt%, 0.2 wt%, or 2 wt%) and the substrate was PTFE.

Interfacial tension was measured using the pendant drop method where the fluid body is deposited by a motorized syringe pump until it achieves a pendant shape. From deriving the force balance between the interfacial tension and gravity, the interfacial tension is extracted from the droplet shape. When needed, the pendant drop method is conducted with the pendant drop submerged in a second liquid to measure the interfacial tension in a quartz cuvette. In this experiment, the droplet was DIW with blue dye submerged in HFE7500 at various FS concentrations (0 wt%, 0.002 wt%, 0.02 wt%, 0.2 wt%, or 2 wt%).

Droplet volume determination. A custom MATLAB script was written to determine the droplet volume. Using image processing, droplets were identified in the experimental videos and the area they encompass was calculated by counting the number of pixels of the droplet. From there, we calculated the effective

diameter of the droplets from the area and depending on if droplet diameter was larger than channel height h, the droplets were approximated as either spherical or cylindrical shape. When droplet diameter is less than the channel height, droplets have a spherical-like shape and when droplet diameter is larger than the channel height, droplets have a cylindrical-like shape. To calculate droplet volume:

If droplet diameter is larger than channel height h,

$$V = \pi r^2 h \quad \text{(Eq. 4)}$$

If droplet diameter is smaller than channel height h,

$$V = \frac{4}{3}\pi r^3 \quad \text{(Eq. 5)}$$

N ≥ 90 droplets were analyzed per data point. The mean (markers) and standard deviation (error bar) of the droplet volume are plotted in Figure 3.4.

This method of computing droplet volume is an estimation from fitting droplets to simple shapes (sphere and cylinder) and was determined to be satisfactory (See Appendix B Figure B7, $R^2 = 0.9799$) for this work as the droplets do not spread much. As can be seen in Appendix B Figure B7, the Matlab code computed small droplet volume accurately while larger computed droplet volumes were overestimated. The overestimation is due to the droplets spreading out as Bond number increases making its droplet height shorter which is not accounted for by the code.

Droplet sorting and merging (Figure 3.6 & 3.7). For transporting a droplet, either a pair of tweezers or a PTFE bead attached to a stylus was used. The stylus was 3D-printed with grey resin (RS-F2-GPGR-04, Formlabs Inc.) and has a ⅛" PTFE ball (McMaster-Carr Supply Co.) adhered to the tip with silicone sealant (Gorilla, Maine Wood Concepts Inc.). The tweezers were a pair of PTFE tweezers with slim, rounded, and smooth tips (McMaster-Carr Supply Co.). For merging droplets, a stainless-steel stitching needle (AEHO crafts) or medical grade No. 22 hypodermic needle was used.

KSCN and $Fe(NO_3)_3$ aqueous solution preparation (Figure 3.8). Green food dye (McCormick Corp.) was added to solutions of 0.1 M of KSCN (Thermo Fisher Scientific Corp.) and 0.05 M of $Fe(NO_3)_3$ (Thermo Fisher Scientific Corp.) until they were approximately the same shade of blue. KSCN is clear

while $Fe(NO_3)_3$ is yellow which is why the blue food dye was not added by exact measurements. The workflow of droplet generation, selection, fusion, and sorting (Figure 3.8) is described in the results section.

3.8 References

1. A. R. Abate, T. Hung, P. Mary, J. J. Agresti and D. A. Weitz, *Proceedings of the National Academy of Sciences*, 2010, **107**, 19163.
2. J. J. Agresti, E. Antipov, A. R. Abate, K. Ahn, A. C. Rowat, J.-C. Baret, M. Marquez, A. M. Klibanov, A. D. Griffiths and D. A. Weitz, *Proceedings of the National Academy of Sciences*, 2010, **107**, 4004.
3. K. Doufène, C. Tourné-Péteilh, P. Etienne and A. Aubert-Pouëssel, *Langmuir*, 2019, **35**, 12597-12612.
4. R. Seemann, M. Brinkmann, T. Pfohl and S. Herminghaus, *Rep Prog Phys*, 2012, **75**, 016601.
5. L. Shang, Y. Cheng and Y. Zhao, *Chemical Reviews*, 2017, **117**, 7964-8040.
6. H. Song, D. L. Chen and R. F. Ismagilov, *Angewandte Chemie International Edition*, 2006, **45**, 7336-7356.
7. S. Y. Teh, R. Lin, L. H. Hung and A. P. Lee, *Lab Chip*, 2008, **8**, 198-220.
8. A. B. Theberge, F. Courtois, Y. Schaerli, M. Fischlechner, C. Abell, F. Hollfelder and W. T. S. Huck, *Angewandte Chemie International Edition*, 2010, **49**, 5846-5868.
9. H.-D. Xi, H. Zheng, W. Guo, A. M. Gañán-Calvo, Y. Ai, C.-W. Tsao, J. Zhou, W. Li, Y. Huang, N.-T. Nguyen and S. H. Tan, *Lab on a Chip*, 2017, **17**, 751-771.
10. C.-G. Yang, Z.-R. Xu and J.-H. Wang, *TrAC Trends in Analytical Chemistry*, 2010, **29**, 141-157.
11. P. Zhu and L. Wang, *Lab on a Chip*, 2017, **17**, 34-75.
12. E. Berthier, A. M. Dostie, U. N. Lee, J. Berthier and A. B. Theberge, *Analytical Chemistry*, 2019, **91**, 8739-8750.
13. J. Berthier and K. A. Brakke, *The Physics of Microdroplets*, Wiley, 2012.
14. J. Berthier, K. A. Brakke and E. Berthier, *Open Microfluidics*, Wiley, 2016.
15. B. P. Casavant, E. Berthier, A. B. Theberge, J. Berthier, S. I. Montanez-Sauri, L. L. Bischel, K. Brakke, C. J. Hedman, W. Bushman, N. P. Keller and D. J. Beebe, *Proceedings of the National Academy of Sciences*, 2013, **110**, 10111.
16. J. J. Lee, J. Berthier, K. E. Kearney, E. Berthier and A. B. Theberge, *Langmuir*, 2020, **36**, 12795-12803.
17. J. J. Lee, J. Berthier, A. B. Theberge and E. Berthier, *Langmuir*, 2019, **35**, 10667-10675.
18. J. J. Lee, J. Berthier, K. A. Brakke, A. M. Dostie, A. B. Theberge and E. Berthier, *Langmuir*, 2018, **34**, 5358-5366.
19. S. B. Berry, J. J. Lee, J. Berthier, E. Berthier and A. B. Theberge, *Analytical Methods*, 2019, **11**, 4528-4536.
20. T. E. de Groot, K. S. Veserat, E. Berthier, D. J. Beebe and A. B. Theberge, *Lab on a Chip*, 2016, **16**, 334-344.
21. C. Li, M. Boban and A. Tuteja, *Lab on a Chip*, 2017, **17**, 1436-1441.
22. M. S. Chowdhury, W. Zheng, S. Kumari, J. Heyman, X. Zhang, P. Dey, D. A. Weitz and R. Haag, *Nature Communications*, 2019, **10**, 4546.
23. J. Clausell-Tormos, D. Lieber, J. C. Baret, A. El-Harrak, O. J. Miller, L. Frenz, J. Blouwolff, K. J. Humphry, S. Köster, H. Duan, C. Holtze, D. A. Weitz, A. D. Griffiths and C. A. Merten, *Chem Biol*, 2008, **15**, 427-437.
24. C. Soitu, A. Feuerborn, C. Deroy, A. A. Castrejón-Pita, P. R. Cook and E. J. Walsh, *Science Advances*, 2019, **5**, eaav8002.

25. C. Soitu, A. Feuerborn, A. N. Tan, H. Walker, P. A. Walsh, A. A. Castrejón-Pita, P. R. Cook and E. J. Walsh, *Proceedings of the National Academy of Sciences*, 2018, **115**, E5926.
26. C. Soitu, N. Stovall-Kurtz, C. Deroy, A. A. Castrejón-Pita, P. R. Cook and E. J. Walsh, *Advanced Science*, 2020, **7**, 2001854.
27. E. J. Walsh, A. Feuerborn, J. H. R. Wheeler, A. N. Tan, W. M. Durham, K. R. Foster and P. R. Cook, *Nature Communications*, 2017, **8**, 816.
28. C. Li, Z. Hite, J. W. Warrick, J. Li, S. H. Geller, V. G. Trantow, M. N. McClean and D. J. Beebe, *Science Advances*, 2020, **6**, eaay9919.
29. C. Li, D. J. Niles, D. S. Juang, J. M. Lang and D. J. Beebe, *SLAS Technol*, 2019, **24**, 535-542.
30. C. Li, J. Yu, P. Paine, D. S. Juang, S. M. Berry and D. J. Beebe, *Lab on a Chip*, 2018, **18**, 2710-2719.
31. C. Li, J. Yu, J. Schehr, S. M. Berry, T. A. Leal, J. M. Lang and D. J. Beebe, *ACS Applied Materials & Interfaces*, 2018, **10**, 17065-17070.
32. L. Chen, V. Yadav, C. Zhang, X. Huo, C. Wang, S. Senapati and H.-C. Chang, *Analytical Chemistry*, 2021, **93**, 6456-6462.
33. J. de Rutte, R. Dimatteo, M. van Zee, R. Damoiseaux and D. Di Carlo, *bioRxiv*, 2020, DOI: 10.1101/2020.03.09.984245, 2020.2003.2009.984245.
34. K. Langer, N. Bremond, L. Boitard, J. Baudry and J. Bibette, *Biomicrofluidics*, 2018, **12**, 044106.
35. B.-U. Moon, N. Abbasi, S. G. Jones, D. K. Hwang and S. S. H. Tsai, *Analytical Chemistry*, 2016, **88**, 3982-3989.
36. C. N. Baroud, F. Gallaire and R. Dangla, *Lab on a Chip*, 2010, **10**, 2032-2045.
37. Y. Gai, J. W. Khor and S. K. Y. Tang, *Lab on a Chip*, 2016, **16**, 3058-3064.
38. E. Berthier, J. Warrick, H. Yu and D. J. Beebe, *Lab on a Chip*, 2008, **8**, 852-859.
39. J. H. Day, T. M. Nicholson, X. Su, T. L. van Neel, I. Clinton, A. Kothandapani, J. Lee, M. H. Greenberg, J. K. Amory, T. J. Walsh, C. H. Muller, O. E. Franco, C. R. Jefcoate, S. E. Crawford, J. S. Jorgensen and A. B. Theberge, *Lab on a Chip*, 2020, **20**, 107-119.
40. D. Y. C. Chan, J. D. Henry and L. R. White, *Journal of Colloid and Interface Science*, 1981, **79**, 410-418.
41. I. Ho, G. Pucci and D. M. Harris, *Physical Review Letters*, 2019, **123**, 254502.
42. J. Lucassen, *Colloids and Surfaces*, 1992, **65**, 131-137.
43. D. Stamou, C. Duschl and D. Johannsmann, *Phys Rev E Stat Phys Plasmas Fluids Relat Interdiscip Topics*, 2000, **62**, 5263-5272.
44. D. Vella and L. Mahadevan, *American Journal of Physics*, 2005, **73**, 817-825.
45. E. Brouzes, M. Medkova, N. Savenelli, D. Marran, M. Twardowski, J. B. Hutchison, J. M. Rothberg, D. R. Link, N. Perrimon and M. L. Samuels, *Proceedings of the National Academy of Sciences*, 2009, **106**, 14195.
46. E. Dhanumalayan and G. M. Joshi, *Advanced Composites and Hybrid Materials*, 2018, **1**, 247-268.

Chapter 4 | Layer-by-Layer Fabrication of 3D Hydrogel Structures Using Open Microfluidics

Reproduced in part from U. N. Lee, J. H. Day,* A. J. Haack,* R. C. Bretherton, W. Lu, C. A. DeForest,[#] A. B. Theberge,[#] and E. Berthier,[#] "Layer-by-layer fabrication of 3D hydrogel structures using open microfluidics." Lab on a Chip, 2020, **20**, 525–536.*
**Equal contribution*
[#]Co-corresponding authors

UNL, JHD, AJH, and RCB conducted the experiments, WL collected preliminary data, CAD, ABT, and EB supervised and UNL, JHD, AJH, ABT, and EB interpreted the results.

Abstract: Patterned deposition and 3D fabrication techniques have enabled the use of hydrogels for a number of applications including microfluidics, sensors, separations, and tissue engineering in which form fits function. Devices such as reconfigurable microvalves or implantable tissues have been created using lithography or casting techniques. Here, we present a novel open microfluidic patterning method that utilizes surface tension forces to form hydrogel layers on top of each other, in a patterned 3D structure. We use a patterning device to form a temporary open microfluidic channel on an existing gel layer, allowing the controlled flow of unpolymerized gel in device-regions. After layer gelation and device removal, the process can be repeated iteratively to create multi-layered 3D structures. The use of open-microfluidic and surface tension-based methods to define the shape of each individual layer enables patterning to be performed with a simple pipette and with minimal dead-volume. Our method is compatible with unmodified (native) biological hydrogels, and other non-biological materials with precursor fluid properties compatible with capillary flow. With our open-microfluidic layer-by-layer fabrication method, we demonstrate the capability to build agarose, type I collagen, and polymer-peptide 3D structures featuring asymmetric designs, multiple components, overhanging features, and cell laden regions.

4.1 Introduction

Hydrogels are configurable and functional materials whose 3D geometries can be patterned to obtain desired functions ranging from mechanical responses (e.g., microfluidic valves, pumps) to organotypic functions (e.g., biological models, implantable materials). Many of these applications have simple geometric requirements, such integration in microfluidic devices as valves,[1, 2] for encapsulating colorimetric indicators,[3] or for chemical separation of desired analytes.[4, 5] For cell culture applications, patterned

hydrogels are used for encapsulating cells in a controlled position relative to additional cell types, microchannels, or extracellular matrix components.[6-14] Reliable and low-entrance barrier solutions to these applications would have the potential of widespread adoption in biology, fluidics, and engineering labs that seek prototyping solutions. Here, we present a method for multilayer hydrogel patterning in three dimensions that uses a simple setup: patterning devices are positioned above a substrate to guide the flow of hydrogel precursors using surface tension forces. Hydrogel materials are delivered with standard pipettes, minimizing dead volume, a key consideration when patterning expensive hydrogels and/or including rare cell types.

There are many established methods for hydrogel patterning, each with their own set of benefits and limitations. Researchers may choose one method based on unique application considerations. Amongst these methods, photopolymerization techniques are robust and offer resolution on the order of microns,[1, 6, 10, 12, 13, 15-19] however photo-initiators have been shown to cause cellular damage,[20, 21] and the necessity for chemical functionalization of the gel precludes the use of native (unmodified) gels. Other broadly used hydrogel patterning methods include inkjet[22-24] and microextrusion[25-29] printing. In these methods, the hydrogel is jetted through a nozzle that exposes any cells encapsulated within the hydrogel to shear stress, which can mechanically damage the cells and limit the types of cells that can be patterned.[30-32] Inkjet and extrusion based printing methods can also require optimization depending on the viscosity and type of gel used. Many of these hydrogel patterning techniques can require large volumes of fluid to fill vats, fluidic channels, or tubing used in typical gel 3D printing setups, limiting the use of rare cell types or expensive gels. Casting hydrogels using a fabricated negative mold provides an alternative approach, but the complexity of the gel structures obtainable is limited due to demolding considerations.[7, 33-35] A hydrogel patterning method that does not rely on photoinitiators, external pressure, tubing, or reservoirs of gel could reduce material waste and alleviate some of the stresses that can affect cell health, rendering it well suited for applications that require fragile, primary, or rare cell types.

In this manuscript, we present a novel layer-by-layer patterning method that uses open microfluidic principles and surface tension driven flow to deposit and sequentially form hydrogel layers in user-defined

patterns, each delivered directly using a pipette. To form each hydrogel layer in a controlled shape, we use a 'patterning device,' which is either a plastic physical 'rail' or a hydrophilic track delineated on a hydrophobic flat surface; both enable the pre-gel solution to flow via capillary action without external pressure and constrain the pre-gel solution under the rail footprint via capillary pinning.[36, 37] The patterning device is placed above an existing hydrogel layer at a designed height. Most of the structures presented in this work were made with layer heights between 100-500 µm, although the method is not limited to heights within this range; demonstrations of the range of layer heights achieved are included in Figure C1-4. The gap between the patterning device and the existing hydrogel layer forms an open microfluidic 'channel' in which liquid pre-gel solution can flow, where the channel 'ceiling' is the patterning device, the 'floor' is the previous gel layer, and the 'sides' are free air-liquid interfaces (Figure 4.1). The patterning device can be removed once the gel layer has formed, and another patterning device can be applied to pattern the next layer, providing the ability to build three-dimensional structures layer-by-layer. This work builds on prior publications demonstrating the use of rails to pattern a single hydrogel layer to partition a well plate for coculture[37-40] where due to the design constraints of the previous rail devices, the patterning device could not be removed once the hydrogel was polymerized, and thus a three dimensional hydrogel structure could not be fabricated. Here, we built multilayer hydrogel structures from native and engineered hydrogels which

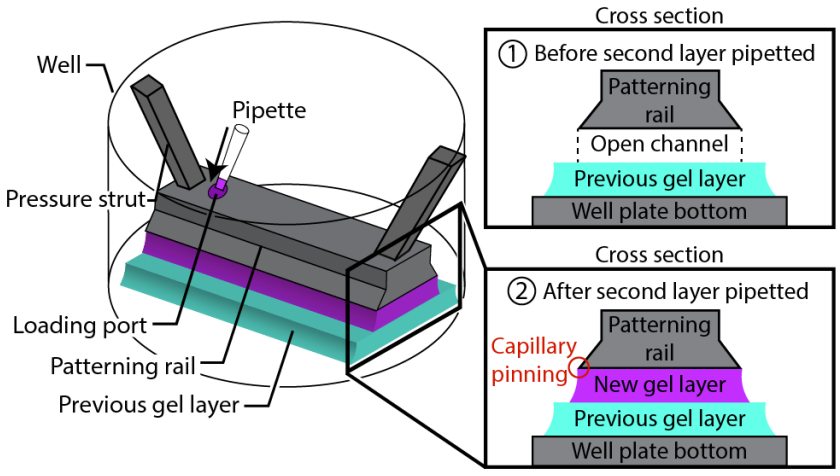

Figure 4.1. Schematic showing the mechanism of layer-by-layer gel patterning using open microfluidics. An open channel is created above an existing gel layer using a rail-based patterning device.

included unsupported overhanging features, objects comprising multiple materials and components both within a layer and across layers, asymmetric designs, and a cell-laden gel architecture. We also demonstrate the capability to spatially control the initial structure of engineered enzymatically degradable dynamic poly(ethylene glycol) (PEG)-based hydrogels. The ability to establish a full layer in a single dispensing step is distinct from extrusion or inkjet patterning methods, which require multiple passes of material deposition for a single layer. Further, in contrast to methods that use photopolymerizable gels and light as a means of patterning hydrogels, which then require washing away of unused, pre-gel solution,[1, 6, 16, 17] we limit waste; all of the pre-gel solution that is dispensed is polymerized and incorporated as part of the patterned material.

4.2 Conditions for layer-by-layer patterning

Our layer-by-layer patterning method uses open microfluidic principles to create temporary open channels on a plastic or existing hydrogel surface allowing pre-gel solution to flow in a spatially controlled area defined by a patterning rail or hydrophilic track (Figure 4.1). The gel can then be polymerized to create a patterned layer of hydrogel tens to hundreds of micrometers thick. The input of gel is powered by spontaneous capillary flow (SCF), which describes the surface tension-based flow of fluids in channel geometries that can have any number of open-air interfaces along the fluid path.[36, 40] The geometric control of the gel layer is obtained by abrupt changes in geometry (in the case of a patterning rail) or hydrophilicity (in the case of hydrophilic tracks) which prevent fluids from flowing past these capillary pinning points. Together, the principles of SCF and capillary pinning enable the creation of a patterned gel layer with simple laboratory equipment (e.g., pipettes) in existing laboratory platforms (e.g., well plates) without requiring actuators, electronics, or pressure sources.

Figure 4.2 shows a specific embodiment of the patterning technique where a patterning rail is used to define the outline of a virtual open microfluidic channel. The patterning rail is placed at the location where the gel will be patterned and sits tens to hundreds of micrometers over the surface of the material below. The geometrical shape of the patterning area is designed to enable the spontaneous capillary flow of pre-gel solution throughout the open channel made between the patterning rail and the surface of the material

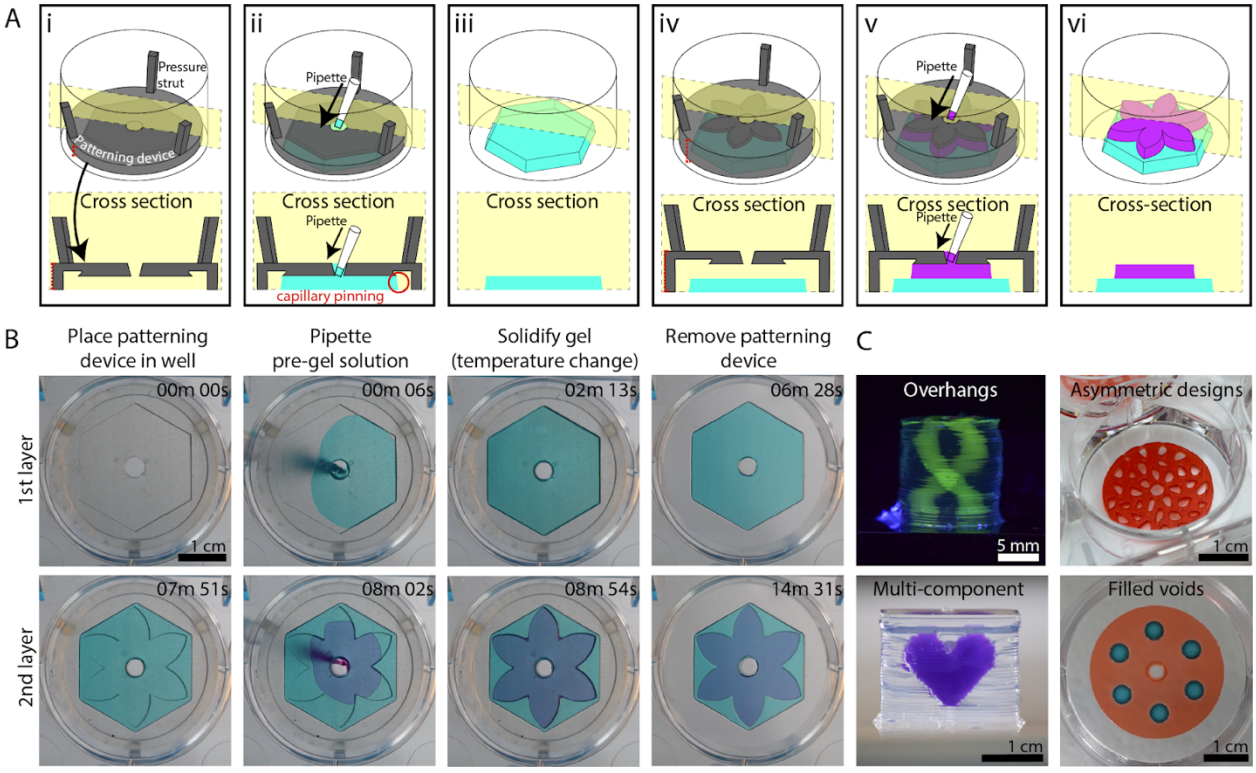

Figure 4.2. Rail-based open microfluidic layered patterning of unmodified hydrogels. (A) Schematic of patterning two layers of gel. (Ai) Patterning device (rail) is placed in a 6-well plate; the patterning region sits 250 µm above the well plate surface. Red dotted line on the left indicates portion of patterning device that is adjusted to determine the thickness of the gel layer. (Aii) Pre-gel solution is pipetted into the pipette port. (Aiii) Patterning device is removed after the pre-gel solution is solidified. (Aiv-Avi) Second layer is patterned using the same steps for the first layer. Red dotted line on the left in Aiv indicates distance between the well plate and the rail after an initial layer of gel is patterned. Note that the dotted line is longer than the red line seen in Ai. Cross-sections of patterning devices show capillary pinning (red circle) and 45° angle around the edges of the device to prevent capillary rise along the vertical face of the patterning device. A magnified schematic is included in Figure C8; an engineering drawing of the hexagon and petal devices is included in Figure C9. (B) Images of the patterning process for 1.5% low gelling temperature agarose dyed for visualization with teal and magenta India ink. Image was taken from the underside of a 6-well plate. (C) Various agarose structures built using rail-based open microfluidics to showcase the power of the method. Cylindrical structure with hollow unsupported winding tubes (double helix) (top, left), asymmetric geometries patterned in a well plate (top, right), a multicomponent structure (bottom, left), and a single layer of gel with islands of voids filled with a second gel in a single pipetting step (bottom, right).

below; capillary pinning enables the pre-gel solution to remain in the defined pattern. The patterning devices can be fabricated in hard plastic, such as resin that is 3D printed from a stereolithography 3D printer or polystyrene (PS) sheets that are CNC milled. The patterning device shown in Figure 4.2 fits inside of a 6-well plate, but the method is not limited to a 6-well plate form. The device sits flush to the floor of the

well plate with spacers to control the height of the gel layer being formed (dotted red line in Figure 4.2Ai and iv, Figure C8, Figure C9) and pressure struts to maintain concentric alignment of the rail within the well.

In this manuscript, we patterned 100-500 μm thick gel layers; numerical simulations of SCF suggest thinner layers (reduced h in Eq. 2) are achievable and, in fact, make it easier to satisfy the condition for SCF in our system which is defined by:

$$\frac{h}{w} < \frac{cos\theta_1 + cos\theta_2}{2} \quad \text{(Eq. 6)}$$

Where h is the height of the patterned layer (defined by the distance between the patterning area of the rail and the underlying substrate), w is the width of the rail perpendicular to the direction of flow, 1 is the contact angle of the hydrogel on the patterning device, and 2 is the contact angle of the hydrogel on the underlying substrate (conventionally equal to zero when flowing hydrogel over an existing hydrogel layer of the same type). To note, viscosity does not play a role in the condition for flow but does play a role in the dynamics of the flow. Higher viscosity pre-gel solutions will flow slower in the generation of a layer, ultimately extending fabrication times. A derivation of Eq. 6 from the generalized Cassie equation is provided in the Appendix C.

When pre-gel solution is loaded into a patterning setup, it fills the 'virtual channel', and remains suspended between the patterning device and the underlying substrate until a polymerization trigger is introduced. Although temperature change was used for polymerization in this work, the ability to polymerize a layer after it has been patterned makes it possible to build multilayered structures of any hydrogel whose pre-gel solution can meet the condition for SCF. After a single layer of pre-gel solution is patterned and solidified (Figure 4.2Ai and 4.2Aii), the patterning device is removed (Figure 4.2Aiii), and a new patterning device is placed over the gel layer to define a new area for the next layer of gel (Figure 4.2Aiv). The patterning process is repeated for each additional layer (Figure 4.2Av and 4.2Avi). With this

method we can deposit an entire layer in one pipetting step, as opposed to alternative nozzle-based 3D patterning methods which require multiple passes of material deposition for a single layer.

It is possible to pattern a pre-gel solution on top of an existing hydrogel layer using our method because capillary pinning still occurs at the junction of the edge of the patterning area and the previous hydrogel layer, maintaining a defined pattern (Figure 4.2B). However, gel overflow is observed for certain features (corresponding to Figure 4.2B), overflow of dispensed fluid at the edges of the 'flower' patterning device occurs because the surface tension of the pre-gel solution, which tends to favor a rounded fluid front, overcomes pinning at the acute internal angles of the patterning device. Due to the manual nature of our method in its current form, applications requiring only a few layers are more suitable for immediate use of the technology. However, we also present several structures with multiple layers (>30) to demonstrate the ability of our layer-by-layer fabrication method to create three-dimensional structures. Figure 4.2C highlights some of these features we achieved with our layered patterning method which include unsupported overhangs, asymmetric geometries, multicomponent structures and cell-laden patterns. These structures are described in more detail in the subsequent figures.

4.3 Multimaterial patterning

The ability to pattern multiple materials in a single structure is of great interest for a variety of applications ranging from creating regions of varying material properties for studying molecular transport,[43, 44] to controlling the gel porosity in specific regions of a microfluidic device for use in chemical separation assays.[4] Patterning multiple materials is also of great importance to organotypic modelling. The cellular environment in biological tissue is heterogeneous in nature, and recapitulating this environment requires spatial control of cells in relation to multicomponent hydrogels and extracellular matrix materials. Our open microfluidic layered patterning method presents a new approach to building multicomponent structures. Figure 4.3A shows how different materials can be introduced at every layer to create a structure with differential material properties in the Z-direction. In Figure 4.3A, an agarose structure was erected beginning with a concentration of 2% wt/v and decreasing 0.25% wt/v every five layers to a final concentration of 0.75% wt/v. Each concentration is dyed a different color for visualization. The resulting

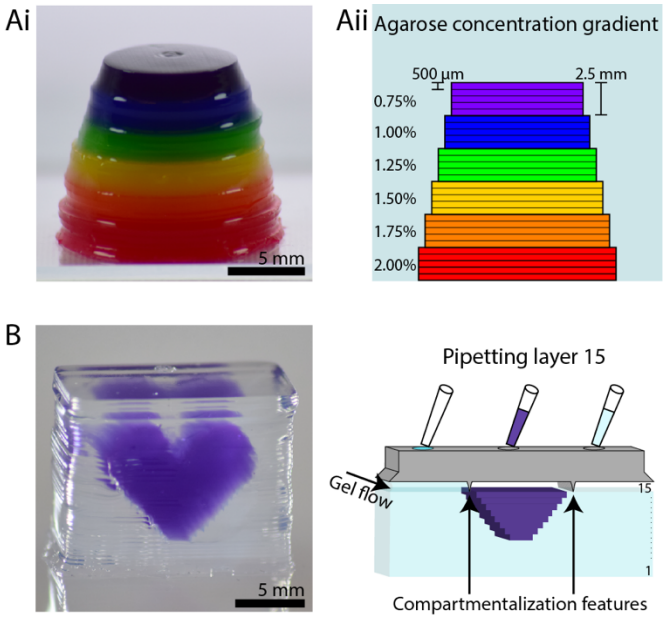

Figure 4.3. Constructing heterogeneous structures. (A) Structure with multiple agarose concentrations. (Ai) Photo of agarose structure (dyed for visualization, with each color representing a different concentration) in ascending layers. Layers are 500 µm thick, and each color contains 5 layers. (Aii) Cross-sectional schematic showing the agarose concentrations in each layer. (B) Purple agarose heart inside a colorless agarose cube demonstrating the ability to pattern materials of different composition *within* a layer (left). Schematic of patterning layer 15 of the 34-layered structure with compartmentalization features to segregate the different gels (right). Layers are 500 µm thick.

structure has a stepwise concentration gradient in the Z-direction. The agarose concentrations were chosen here as a proof of concept to demonstrate the ability to pattern different compositions across layers. These concentrations also fall within the range of relevant concentrations used for transport models of biological systems such as the brain extracellular space; our layered patterning method has the potential to be extended for brain extracellular matrix modeling application in future work.[44, 45]

The ability to pattern multiple materials *within the same layer* is essential to creating a structure with spatial organization in all three dimensions. Work by others to enable single layer printing of multiple gels through a multi-nozzle 3D printing system has demonstrated the interest of this capability in 3D bioprinting.[29, 46] To demonstrate the ability to pattern materials with different compositions within a layer using our method, we built a purple agarose heart within a colorless agarose cube (Figure 4.3B, left). In this case, we added a simple ridge to the patterning rail to segregate the regions of different materials (purple

and colorless agarose). Thus, different solutions agarose of agarose dyed different colors were allowed to flow within each layer in a defined pattern (Figure 4.3B, right).

4.4 Constructing unsupported overhanging features

A design challenge for patterning three-dimensional hydrogel structures is building unsupported features (i.e., features that cantilever into air rather than building on base material underneath). Other systems for patterning soft materials have utilized sacrificial material as a support, which is removed in a post-processing step either physically or chemically.[23, 29, 47] The structural integrity of the desired product must be maintained after the supports are removed, which restricts the types of materials that can be used. Using our method, a dissolvable sacrificial gel approach could be employed; we also show that it is possible to create overhanging, unsupported structures without the use of sacrificial material by incrementally offsetting the patterning device from the edge of the previous layer such that each layer extends past the limits of the previous layer (Figure 4.4A). To exemplify this concept, the schematic in Figure 4.4B illustrates a rail design without an overhang (left) and with an overhang (center and right).

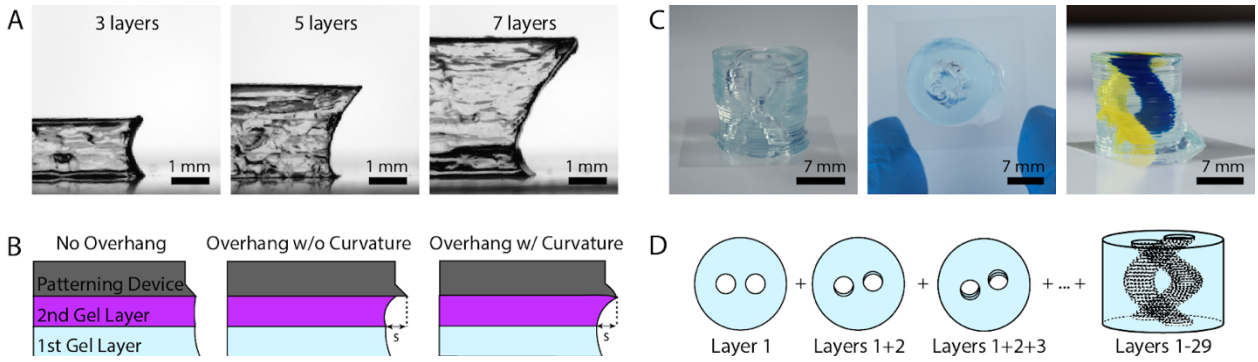

Figure 4.4. Rail-based open microfluidic layered patterning of overhanging features. (A) Imaging of a cross section of an overhanging agarose structure at three different points of production, 3 layers (left), 5 layers (center) and 7 layers (right). (B) Schematic for rail design of overhanging features showing no overhang, an overhang without curvature and an overhang with downward curvature; the latter rail design was used to print the structures shown in A and C. (C) Images of cylindrical structure with hollow unsupported winding tubes (double helix) made from agarose, showing side view (left), top down image (center), and side view where tubes are filled with yellow and blue India ink dyes for visualization (right). Full description of design in Appendix C and Figure C10. (D) Schematic showing the process for building the double helix structure, where the blue color represents the patterned agarose. Each layer is rotated about the center from the previous layer, forming a hollow helix within a cylinder of agarose.

We found the length of overhang achievable was improved by the addition of a downward curvature to the edge of the patterning device to allow for favorable flow over the edge of the previous gel layer (Figure 4.4B, right). Without the added curvature, the bottom of the fluid front pins to the edge of the previous layer as expected, but the top of the advancing pre-gel solution does not continue along the patterning device (Figure 4.4B, center). The curvature decreases the relative ratio of the air-liquid interface to the patterning device-liquid interface; minimizing this ratio is favorable for SCF.[36] Thus, the agarose fluid front continues along the surface of the patterning device, increasing the overhang capacity. Each patterning device has a different radius of curvature based on the curvature of the previous patterning device. Detailed descriptions of how these dimensions were determined are included in the Appendix C and Figure C10, and the dimensions are given in Table C1. To fully demonstrate the capabilities of our method to produce geometries with overhanging features, we built an agarose cylinder with hollow winding tubes in the shape of a double helix (Figure 4.4C and 4.4D). The helix consists of 30 layers, each 500 μm thick, and has a total rotation of 270 degrees.

Previously, other fabrication methods have utilized a sacrificial material to create void spaces and channels through a three-dimensional hydrogel structure[29, 38] or have employed a casting method to create fluidic channels.[7] Furthermore, laser photoablation can be used to create microchannels through hydrogels with high resolution,[48] and recently multiphoton lithography has been used to photodegrade microchannels within cell-laden PEG-based hydrogels.[15] The approach we have taken here and the helix geometry proof of concept structure demonstrates the broader capacity to create gels with three-dimensional tubing and void spaces, thereby opening up the possibility of creating three-dimensional fluidic channels spanning multiple planes through a hydrogel structure without reliance on a sacrificial material or post-fabrication step.

4.5 Integrated fluidic channels for single-step void filling

We also demonstrate that it is possible to add open microfluidic functionality to the top of the patterning device, where the flow is also driven by capillary action.[49] This capability can be utilized as another method by which multiple materials can be deposited in a single layer (Figure 4.5). We used open

channels to deliver blue colored agarose to the voids in the red colored agarose layer below, which enables a single pipetting step to fill all six voids (Figure 4.5B).

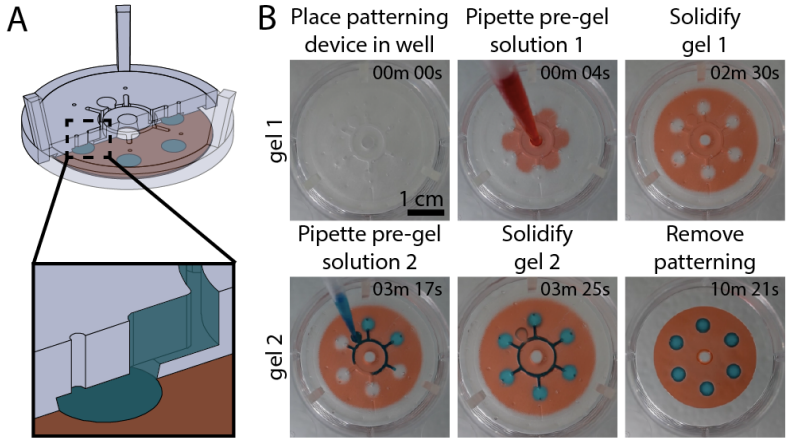

Figure 4.5. Integrated fluidic channels in patterning device for depositing second material in a layer. (A) Cross-sectional schematic representation of 'void-filling' patterning device with underlying layer. (B) Video stills of patterning red colored agarose (250 µm thick) and filling voids with blue colored agarose (750 µm thick).

4.6 Cell-laden collagen I patterning

Agarose is a useful hydrogel for characterizing the possible geometries and limitations of our patterning method as its structural properties make it ideal for withstanding a three-dimensional structure. Further there are many applications in which agarose patterning is useful, such as spatially defined microbial culture.[50] However, agarose does not contain extracellular matrix components and does not facilitate mammalian cell adhesion. Further, layer delamination may occur because agarose lacks intrinsic cross-linking characteristics, and the temperature dependent gelation of agarose can affect its flow depending on the starting temperature of the precursor solution. Given these limitations, we also characterized our method for use with other, cell compatible materials including unmodified type I collagen and engineered enzymatically degradable PEG-based hydrogels.

Many materials such as collagen do not have the mechanical properties necessary to create free-standing 3D structures without the use of a second support material. To overcome this challenge, we utilized the ability to pattern a single layer with multiple materials to create an agarose 'support' structure for

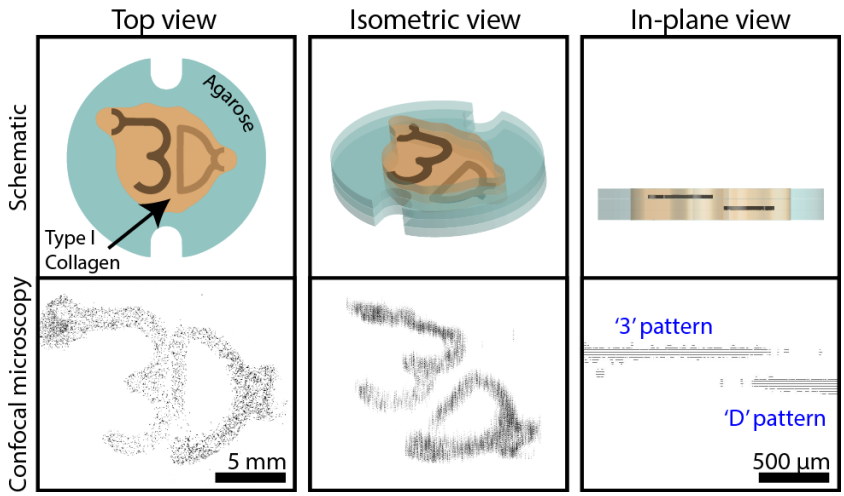

Figure 4.6. Schematics and confocal images of human fetal lung fibroblasts in a type I collagen structure. Cells were stained with Calcein AM (shown in black). The top view comprises 130 fields of view (which each contain 27 Z-stacked images) stitched together. Cells that make up the "3" and "D" are each printed in separate 100 µm thick collagen layers that are separated from each other by a 200 µm thick cell-free collagen layer. Z-step value was increased tenfold in isometric view for visualization purposes. Original confocal image file is included in Figure C5. Schematic of the workflow used to achieve this structure is shown in Figure C6; note: the additional features on the top left of the "3" and the right of the "D" were an intentional part of the design, used as loading ports for the pre-gel solution.

unmodified type I collagen (7.5 mg/mL). Type I collagen was chosen because it is abundant in biological systems. Here, we demonstrate an alternative method for patterning layers of commercially available concentrations of unmodified collagen (Figure 4.6). Briefly, we patterned an agarose border on each layer, which was subsequently filled with cell-free collagen. Cell-laden collagen was then patterned over the newly established layer of collagen (Figure C6). Figure 4.6 shows 130 confocal image stacks stitched together of Calcein AM stained human fetal lung fibroblasts in a type I collagen structure. Cells in this structure were 87% viable, quantified using live/dead (Calcein AM/ethidium homodimer) staining (Figure C5). The '3' and 'D' patterns represent two cell populations that were printed on two different layers, each 100 µm thick and separated by a 200 µm thick cell-free layer. A workflow schematic of the layer-by-layer collagen patterning process is shown in Figure C6.

4.7 Stimulus-responsive hydrogel structure

Stimulus-responsive biomaterials, often referred to as "4D biomaterials", add a temporal dimension of control to a 3D material.[51,52] Through well-defined molecular topology, these dynamic hydrogels can be

chemically or physically modulated on demand in response to precise combination of environmental inputs (e.g., light, small molecules, cell-secreted enzymes, exogenous enzymes) following Boolean logic.[53, 54, 55, 56, 15] Here, we introduce and utilize novel 4D peptide-polymer hydrogels that can be enzymatically degraded with cell-secreted matrix metalloproteases (MMPs) and/or exogenously added sortase (SrtA). Transpeptidation by SrtA has been demonstrated as a rapid, bio-orthogonal means of encoding dynamic behavior into gels but offers no spatial control over degradation.[57, 58] Here, we used our 3D patterning method to create a stimulus-responsive cell-laden PEG-based hydrogel multimaterial structure featuring different enzymatically degradable crosslinkers (Figure 4.7). Since these responsive PEG-peptide materials are formed through spontaneous reaction of two components in water (here, strain-promoted azide-alkyne cycloaddition),[41] their formation cannot readily be patterned using conventional techniques (e.g., extrusion,

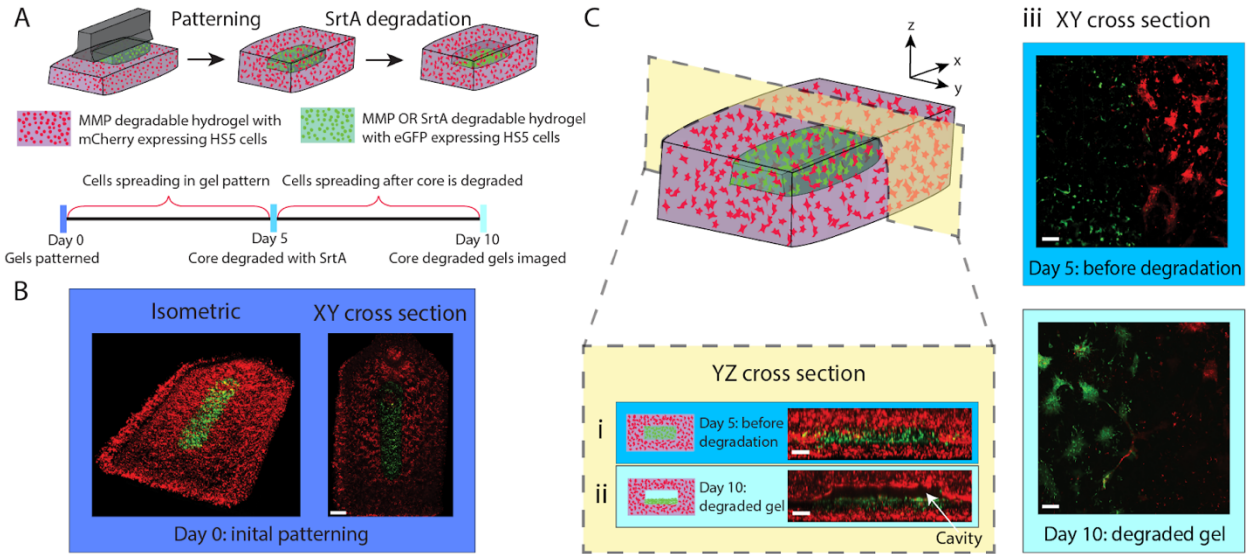

Figure 4.7. Layer-by-layer patterning of enzymatically degradable PEG-based hydrogel structures. (A) Timeline of degradation experiment, highlighting SrtA treatment on Day 5 that triggers degradation of the eGFP$^+$-cell-containing core. (B) Confocal images acquired immediately after multimaterial gel patterning. eGFP-expressing HS5 cells (green) were encapsulated in the MMP- OR SrtA-degradable core, mCherry-expressing cells (red) are in the surrounding MMP-only degradable hydrogel. Scale bar is 1 mm. (C) YZ cross-sectional view of gels (Ci) on Day 5 immediately preceding SrtA treatment, and (Cii) after 10 days of culture (5 days post core degradation), where released eGFP$^+$-cells settle to the bottom of the empty cavity to form a monolayer on the intact gel layer below. Scale bars are 200 µm. (Ciii) Confocal images (XY cross sections) at the interface between the bottom and middle layers on day 5 (prior to SrtA treatment) and day 10. eGFP$^+$-cells exhibit a 3D spread morphology on day 5, but transition to a 2D monolayer after release. Scale bars are 200 µm.

photopolymerization), which has placed limitations on their usage in tissue engineering.

To demonstrate 3D fabrication of cell-laden multimaterial structures and their spatially coded responsiveness, we generated a structure whose inner cavity could undergo triggered degradation (Figure 4.7A). To achieve this geometry, the structure was fabricated with a PEG-based gel with two different crosslinkers; the crosslinker in the inner cavity was degradable by SrtA OR MMP, while the crosslinker in the outer structure could only be degraded by MMPs. The total height of the structure was 0.5 mm, allowing for diffusion of nutrients through the gel when the final structure was submerged in media after fabrication. A schematic of the fabrication process and dimensions can be found in Figure C11. The inner core height was designed as 100 μm with a width of either 1.0 mm or 0.5 mm. Confocal images in Figure 4.7 and Figure C12 are of the larger (1.0 mm designed width of degradable cavity) geometry, and Figure C13 shows confocal images of both geometries. Fluorescent HS5 cells were encapsulated in the gel multimaterial, with cells in the outer MMP-degradable regions expressing mCherry and those in the SrtA- OR MMP-degradable inner cavity expressing eGFP. Figure 4.7A shows the timeline and schematic of the fabrication; further details are included in the Experimental section. Briefly, cells were cultured in the patterned gel for five days before SrtA treatment. At that point, the gel was treated with SrtA to facilitate degradation. The structure was incubated in DMEM media for an additional five days after the degradation before imaging. Confocal images before SrtA treatment (day 5) show the core of the structure intact with eGFP-expressing cells (green) distributed throughout the gel core and those expressing mCherry in the surrounding regions (Figure 4.7Ci). After triggered degradation of the inner cavity and extended culture (day 10), the resulting structure is a fully enclosed void space (Figure 4.7C and Figure C12), with released $eGFP^+$-cells settling to the bottom of the degraded core to form a monolayer (Figure 4.7Cii). Owing to the MMP-degradability of both the inner and outer layers, cells can actively remodel and spread within the hydrogel materials. As demonstrated, our generalizable patterning technique adds another dimension of control to responsive biomaterials; we view this as tremendously valuable for gel types that are incompatible with traditional additive manufacturing techniques, including the many that form through spontaneous reactions.[59]

4.8 Hydrophilic tracks for layer-by-layer patterning

For each structure presented in Figures 4.2-4.7, we used a separate patterning rail (fabricated by 3D printing or CNC milling) for each layer (Figure 4.8Ai). While this method is convenient for development of our method, fluid patterning by SCF can also be achieved without a physical rail by using a flat surface with patterned hydrophilic and hydrophobic regions to guide fluid flow by SCF into a desired pattern; the fluid flows along the hydrophilic tracks and pins at the hydrophilic/hydrophobic boundary (Figure 4.8Aii).

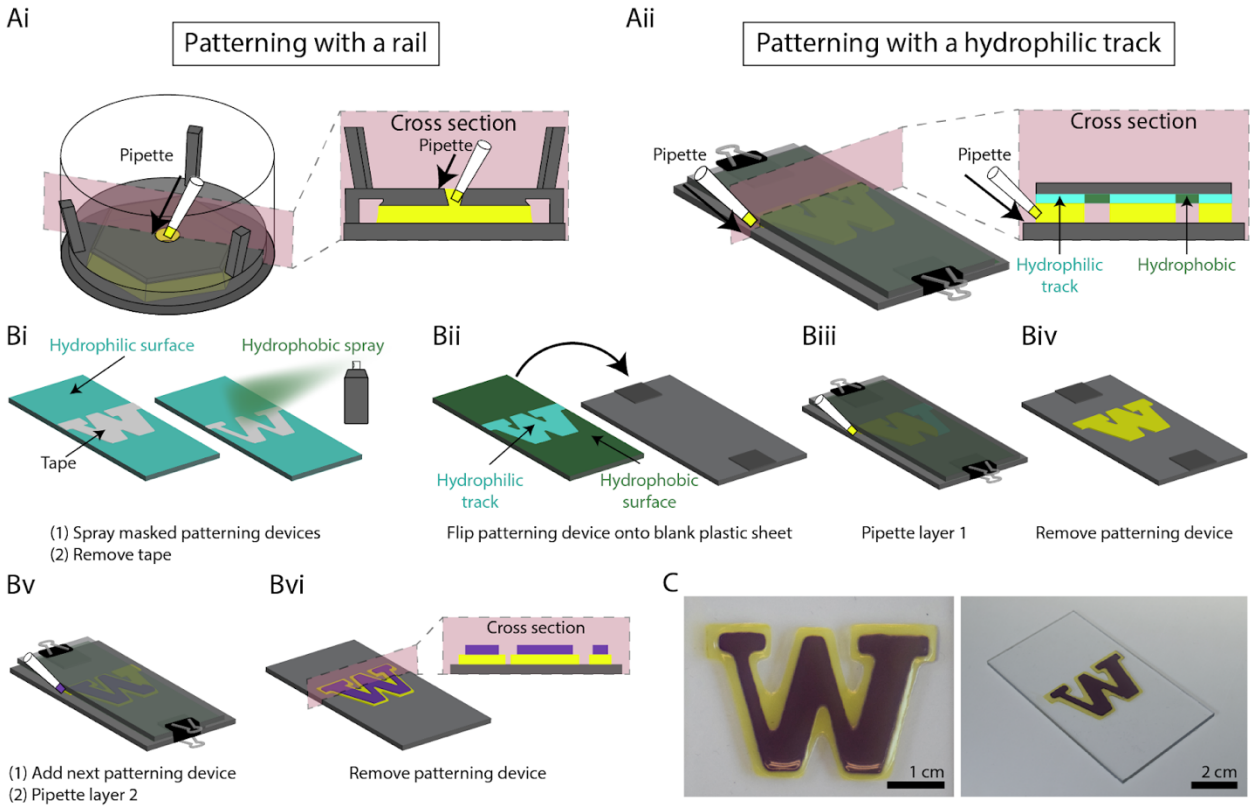

Figure 4.8. Layer-by-layer hydrogel patterning without a rail. (A) Overview of two patterning processes contrasting (Ai) patterning with a rail and (Aii) patterning with hydrophilic tracks. (Bi) Plasma treated polystyrene (PS) sheets were masked with tape, and a hydrophobic spray was applied. After the hydrophobic layer had set, the tape was removed. (Bii) The hydrophobic side of the PS sheet placed face down onto a clean, plasma treated PS sheet with stacked coverslips as spacers to create a gap between the two sheets. (Biii) The patterning device was secured to the spacers and bottom substrate with binder clips and the pre-gel solution was pipetted in the gap between the patterning device and bottom substrate at both sides of the 'W'. (Biv) The patterning device was removed after the gel solidified. (Bv) Additional coverslips were stacked on the existing spacers to create a larger gap for the second layer, and the second patterning device was aligned by eye, placed and secured with binder clips. The second layer of pre-gel solution was then pipetted in the same way. (Bvi) The patterning device was removed to reveal the 2-layered hydrogel structure. The thickness of each layer was 500 µm (C) Top view (left) and isometric (right) photo of two-layered agarose 'W'.

This concept builds on past work where localized hydrophilic/hydrophobic patterning on a single flat surface was used to constrain fluids to a hydrophilic pattern.[60, 61] Here, we extended this patterning concept to create a two-layered hydrogel structure, showing that the hydrophilic/hydrophobic patterning template can be removed after each hydrogel layer is created to iteratively build up multiple layers of hydrogel structures (Figure 4.8B). In the present embodiment, we plasma treated a polystyrene sheet and masked the area we wanted to preserve as hydrophilic with tape (i.e., the "W" shape shown in Figure 4.8Bi). A commercially available hydrophobic treatment spray was applied to create a hydrophobic background. The tape was then removed after the hydrophobic treatment, revealing a hydrophilic patterning region surrounded by a hydrophobic background. We built a two layer hydrogel (agarose) "W" structure on a polystyrene base substrate. Using stacked, glass coverslips as spacers above the polystyrene base substrate, we created a 500 μm gap between the base substrate and the hydrophilic/hydrophobic patterning surface. The pre-gel solution flowed in this gap via SCF, as previously described, pinned at the interface between the hydrophilic and hydrophobic region creating the "W" pattern set by the hydrophilic region (Figure 4.8B-C). This result demonstrates that our open microfluidic layer-by-layer method can be implemented without a physical rail, opening up the potential for future embodiments in which the hydrophilic/hydrophobic regions are patterned via reversible or actuatable approaches.

4.9 Conclusion

A novel open microfluidic method for layer-by-layer patterning of 3D hydrogel objects has been demonstrated. Our method uses fundamentally different principles—surface tension forces and open microfluidics—from existing methods to pattern hydrogel structures. Hydrogel waste is minimized in our layer-by-layer patterning method because it uses simple pipettes (with no dead volume) rather than requiring large vats of material or dispensing containers common in some hydrogel 3D printing methods, opening up the potential to use expensive hydrogels, rare cells such as primary patient samples, or precious reagents in small volume, a benefit of microfluidics.

We demonstrated the compatibility of our method with three materials: agarose, collagen, and PEG-based engineered hydrogels. Though each material type was amenable to 3D-patterned deposition, it is

important to note that different gel precursors and patterned geometries have their own set of limitations and may require device optimization to achieve a desired structure. We fabricated structures that comprised representative features—specifically features that are enabled by additive manufacturing. In terms of feature geometry, we specifically found limitations in flowing around sharp corners as demonstrated in the roundedness of the acute angle of the "W" in Figure 4.8. Filling out sharp corners is also challenging such as the corner of a square, particularly at higher layer heights (Figure C1).

Complementing our efforts to define gel geometry with a physical rail, we have demonstrated that similar multilayer structures can be generated using patterned hydrophilic/hydrophobic surface coatings. Our hydrogel patterning method, used with surface chemistries that allow for rapid reversible patterning of hydrophilic and hydrophobic regions, could be amenable to rapid automation. Further improvements in processing time could be achieved through reaction conditions (e.g., temperature) optimized for specific gelation chemistries. Importantly, using the embodiment shown in the present manuscript, we demonstrated layered patterning of cell-laden structures using standard cell culture materials and procedures without subjecting the fluid to external pressure, suggesting that this method has the potential to be extended for use with other cell types. Our capacity to control the location of different gel materials within and between layers suggests the possibility to create 3D organoid models by directing the patterning of cell types and culture materials in 3D space. Building open microfluidic channels directly into the patterning device (Figure 4.5) can enable efficient delivery of reagents, cells, or other components into void spaces with a single dispensing step. Moreover, as demonstrated, our method can be used to create overhanging structures and hollow tubes, extending the capability of adding fluidics (e.g., channels, voids) throughout the gel itself, thus opening up possibilities for complex three-dimensional models and systems. Finally, we demonstrated the capability to pattern engineered dynamic hydrogels that could not be extruded or photopolymerized, enabling the 3D spatial control of multimaterial structures that respond dynamically to their environment, yielding a new breed of 4D functional materials.

4.10 Materials and methods

Patterning Device Design and Fabrication (Figures 4.2-4.6): Patterning devices were designed in Solidworks 2017 and 3D printed out of clear resin (RS-F2-GPCL-04) using a Form 2 stereolithography 3D printer (Formlabs) (Figures 4.2-4.6) or milled (Figure 4.6) on a computer numerical control (CNC) mill (PCNC770, Tormach). The patterning devices were sonicated in isopropyl alcohol (IPA) for 10 minutes and again in clean IPA for 5 minutes to remove excess uncured resin. The devices were dried with compressed air and cured under a 395-405 nm 20W UV lamp (Quans) for 1 hour.

Plasma Treating Patterning Devices (Figures 4.2-4.7): The patterning devices were plasma treated for increased wettability using a Zepto plasma treater (Diener Electronic). The chamber was pumped down to a pressure of 0.20 mbar, gas (free air) was supplied (4 min, 0.25 mbar), and power enabled (2 min, 200 W).

Agarose Gel Composition: Low gelling temperature agarose (MilliporeSigma) was dissolved in deionized water to a concentration of 15 mg/mL and dyed for visual aid with food dye (Spice Supreme), fluorescein labeled dextran (70,000 MW, Invitrogen), or India ink (Dr. Ph Martin's). All agarose structures used 1.5% wt/v gel except for the multicomponent structure in Figure 4.3A.

Fabrication of Overhanging Structures (Figure 4.4): For the seven layer overhang structure, each layer height was 500 m. Layers 2 and 3 were designed to be 239.9 m of overhang, whereas the following layers were designed to be 479 m of overhang (*s* in Figure 4B). A schematic of the patterning device design and detailed dimensions can be found in Appendix C.

Fabrication of Hollow Double Helix (Figure 4.4): Using the patterning device in a 6-well plate, each layer was allowed to set at room temperature for approximately 10-20 minutes prior to removal of the patterning rail. Each helix was constructed over 2-3 days; the total fabrication time if done at once was about 10 hours. Sacrificial water was added to the empty wells in the 6-well plates to prevent drying when stored overnight. More details on the design of each layer can be found in Appendix C.

4.Type I collagen solutions were neutralized by mixing rat tail collagen (Corning #354249) with 500 mM HEPES in a 9:1 ratio, respectively. Cell suspensions containing human fetal lung (HFL) fibroblasts (ATCC) at concentrations of ~9 million cells/mL were then added to the collagen solutions in a 1:2 ratio,

respectively, to give a final collagen concentration of 5 mg/mL and a final cell concentration of ~3 million cells/mL. Cell-laden structures were incubated at 37 °C for 24 hours in Dulbeco's modified eagle medium (Gibco) prior to imaging. Cells were stained with Calcein AM and ethidium homodimer (MilliporeSigma). Cell-laden structures were imaged with a Leica TCS SP5 II confocal microscope and a 17.9 m Z-step. Images were processed in FIJI software.

Patterning Type I Collagen (Figure 4.6): Patterning collagen was achieved with the addition of a flattening step (Figure C6). This step involves placing a patterning device over the collagen layer prior to gelling such that the collagen will wet the pattern on the device, creating a flat surface to guide flow for the next layer. When the collagen is gelled and the device removed, the height of the resulting gel layer is precisely set in the shape and location of the pattern to be flowed in the next layer. Each layer was patterned at room temperature and immediately placed in a cell culture incubator until the next layer was patterned. The entire structure took ~5 hours to fabricate.

PEG Hydrogel Fabrication: PEG hydrogels were generated through strain-promoted azide-alkyne cycloaddition (SPAAC) between PEG-tetraBCN (4 mM) and peptide di-azide crosslinkers (8mM) with the inclusion of 1mM N_3-GRGDS-NH_2 to promote cell adhesion to the hydrogel.[15, 41] More information on hydrogel and peptide synthesis can be found in Appendix C. To prevent cell and gel adhesion to the rails upon removal, 3D printed patterning rails were not plasma treated and were incubated in 1% Bovine Serum Albumin (MilliporeSigma) in water for 1-2 hours prior to patterning. Gel precursors were mixed with cell suspension, patterned using 3D printed rails, with each layer polymerized for 15 minutes at 37°C. The design consists of 3 layers, and 4 patterning steps and the entire fabrication process took ~1.5-2 hours.

HS5 Cell Culture in PEG Hydrogels: HS5 transformed human bone-marrow stromal cells expressing either eGFP or mCherry were the generous gift of Dr. Brian Hayes at the Fred Hutchison Cancer Research Center. Cells were cultured in Dulbecco's Modified Growth Medium (DMEM) (Gibco) containing 10% Fetal Bovine Serum (FBS) and 1% Penicillin/Streptomycin and passaged at a 1:5 ratio at confluence. During passage, cells were encapsulated in 4 mM PEG gels as described above at a density of 20 x 10^6 cells/mL. Encapsulated cells were cultured for 5 days, degraded through treatment with an evolved Sortase

A pentamutant [SrtA(5M)][42] on day 5, and then cultured for an additional 5 days prior to imaging on day 10. Gels were imaged by confocal point scanning microscopy on a Leica SP8 microscope. Whole gel z-stacks were obtained at 10x magnification with a 5 μm z-step. Detector gain and laser power compensation were applied during acquisition to account for light attenuation through the gel.

PEG Hydrogel Degradation using SrtA(5M): A SrtA(5M) working solution consisting of 50μM SrtA(5M), 18 mM triglycine (Chem Impex; Wood Dale, IL), and 1.8 mM $CaCl_2$ (Sigma Aldrich; St. Louis; MO) was prepared in 1X PBS. More information on recombinant expression and purification of the SrtA(5M) can be found in Appendix C. To initiate degradation of SrtA-susceptible regions, media was aspirated from the patterned gels and replaced with 600 μL of SrtA(5M) working solution. After 90 minutes of enzyme treatment, the SrtA(5M) working solution was aspirated from gels and replaced with DMEM supplemented with 10% FBS.

Hydrophobic coating for patterning (Figure 4.8): Rectangular polystyrene (PS) pieces were cut using a CNC mill (DATRON neo) to the same width as the designed "W" pattern. All PS pieces were plasma treated using the same protocol for the 3D printed patterning devices. The 'W' pattern, was cut from masking tape (3M) using a plotter cutter (Graphtec CE6000-40) and then applied to the plasma treated side of the PS, such that the edges of the 'W' lined up with the edges of the PS. Two coats of Step 1 of Rust-Oleum Neverwet™ hydrophobic treatment were applied, allowed to dry for 10 minutes, and then three coats of Step 2 were applied, and left to dry for an additional 10 minutes. The masking tape was removed, revealing a hydrophilic pattern with hydrophobic surroundings. Neverwet™ may affect cell viability and we do not intend to use this reagent with cell culture.

Patterning hydrogels using hydrophilic/hydrophobic interfaces (Figure 4.8): Two No. 1.5 coverslips (Fisherbrand) were stacked on top of a PS base at both ends. Double-sided tape was placed between each coverslip to prevent slipping during assembly. The total height of the coverslips and double-sided tape was measured to be 500 m with a caliber. The patterning piece (described above in the preceding section) was placed facedown over the coverslips and base. Binder clips were used to secure the PS layers and coverslips. A picture of the setup for the first layer can be found in Figure C7. 1.5% w/v agarose was dyed

purple and yellow using India Ink (Dr. Ph Martin's). The first layer was patterned by placing the pipette at the edge of the hydrophilic patterning region in between the patterning piece and the base. Both ends of the W were used as inlets. The agarose was allowed to solidify for 10 minutes before the patterning device was removed. To achieve the second layer, two additional coverslips and double-sided tape were added to increase the distance between the base and the second patterning device, which was aligned by eye. The gel loading and setting process for the second layer was the same as for the first layer.

Image Processing: Images were processed using Adobe Photoshop CC 2018 using a uniform brightness/contrast adjustment.

4.11 References

1. D. J. Beebe, J. S. Moore, J. M. Bauer, Q. Yu, R. H. Liu, C. Devadoss and B.-H. Jo, *Nature*, 2000, **404**, 588-590.
2. S. B. Kim, Y. Zhang, S. M. Won, A. J. Bandodkar, Y. Sekine, Y. Xue, J. Koo, S. W. Harshman, J. A. Martin, J. M. Park, T. R. Ray, K. E. Crawford, K.-T. Lee, J. Choi, R. L. Pitsch, C. C. Grigsby, A. J. Strang, Y.-Y. Chen, S. Xu, J. Kim, A. Koh, J. S. Ha, Y. Huang, S. W. Kim and J. A. Rogers, *Small*, 2018, **14**, 1703334.
3. J. Choi, Y. Xue, W. Xia, T. R. Ray, J. T. Reeder, A. J. Bandodkar, D. Kang, S. Xu, Y. Huang and J. A. Rogers, *Lab on a chip*, 2017, **17**, 2572-2580.
4. A. E. Herr, A. V. Hatch, D. J. Throckmorton, H. M. Tran, J. S. Brennan, W. V. Giannobile and A. K. Singh, *Proceedings of the National Academy of Sciences*, 2007, **104**, 5268.
5. C.-C. Kang, K. A. Yamauchi, J. Vlassakis, E. Sinkala, T. A. Duncombe and A. E. Herr, *Nature Protocols*, 2016, **11**, 1508.
6. V. Chan, P. Zorlutuna, J. H. Jeong, H. Kong and R. Bashir, *Lab on a chip*, 2010, **10**, 2062-2070.
7. Y. Ling, J. Rubin, Y. Deng, C. Huang, U. Demirci, J. M. Karp and A. Khademhosseini, *Lab on a chip*, 2007, **7**, 756-762.
8. G. Ongo and D. Juncker, Kaohsiung, Taiwan, 2018.
9. B. H. Chueh, Y. Zheng, Y. S. Torisawa, A. Y. Hsiao, C. Ge, S. Hsiong, N. Huebsch, R. Franceschi, D. J. Mooney and S. Takayama, *Biomed Microdevices*, 2010, **12**, 145-151.
10. W.-G. Koh and M. V. Pishko, *Analytical and Bioanalytical Chemistry*, 2006, **385**, 1389-1397.
11. K. C. Hribar, K. Meggs, J. Liu, W. Zhu, X. Qu and S. Chen, *Scientific Reports*, 2015, **5**, 17203.
12. M. S. Hahn, J. S. Miller and J. L. West, *Advanced Materials*, 2006, **18**, 2679-2684.
13. V. A. Liu and S. N. Bhatia, *Biomedical Microdevices*, 2002, **4**, 257-266.
14. S. Khetan and J. A. Burdick, *Soft Matter*, 2011, **7**, 830-838.
15. C. K. Arakawa, B. A. Badeau, Y. Zheng and C. A. DeForest, *Advanced Materials*, 2017, **29**, 1703156.
16. J. Liu, D. Gao, H. F. Li and J. M. Lin, *Lab on a chip*, 2009, **9**, 1301-1305.
17. J. Decock, M. Schlenk and J.-B. Salmon, *Lab on a chip*, 2018, **18**, 1075-1083.
18. S. J. Bryant, J. L. Cuy, K. D. Hauch and B. D. Ratner, *Biomaterials*, 2007, **28**, 2978-2986.
19. G. Papavasiliou, P. Songprawat, V. Pérez-Luna, E. Hammes, M. Morris, Y.-C. Chiu and E. Brey, *Tissue Engineering Part C: Methods*, 2008, **14**, 129-140.
20. C. G. Williams, A. N. Malik, T. K. Kim, P. N. Manson and J. H. Elisseeff, *Biomaterials*, 2005, **26**, 1211-1218.
21. L. Xu, N. Sheybani, W. A. Yeudall and H. Yang, *Biomaterials Science*, 2015, **3**, 250-255.

22. T. Boland, X. Tao, B. J. Damon, B. Manley, P. Kesari, S. Jalota and S. Bhaduri, *Materials Science and Engineering: C*, 2007, **27**, 372-376.
23. C. Xu, W. Chai, Y. Huang and R. R. Markwald, *Biotechnology and Bioengineering*, 2012, **109**, 3152-3160.
24. T. Xu, W. Zhao, J.-M. Zhu, M. Z. Albanna, J. J. Yoo and A. Atala, *Biomaterials*, 2013, **34**, 130-139.
25. A. Bandyopadhyay, V. K. Dewangan, K. Y. Vajanthri, S. Poddar and S. K. Mahto, *Biocybernetics and Biomedical Engineering*, 2018, **38**, 158-169.
26. S. Sakai, K. Mochizuki, Y. Qu, M. Mail, M. Nakahata and M. Taya, *Biofabrication*, 2018, **10**, 045007.
27. J.-H. Shim, J.-S. Lee, J. Y. Kim and D.-W. Cho, *Journal of Micromechanics and Microengineering*, 2012, **22**, 085014.
28. F. Pati, J. Jang, D.-H. Ha, S. Won Kim, J.-W. Rhie, J.-H. Shim, D.-H. Kim and D.-W. Cho, *Nature Communications*, 2014, **5**, 3935.
29. T. J. Hinton, Q. Jallerat, R. N. Palchesko, J. H. Park, M. S. Grodzicki, H.-J. Shue, M. H. Ramadan, A. R. Hudson and A. W. Feinberg, *Sci Adv*, 2015, **1**, e1500758-e1500758.
30. R. Chang, J. Nam and W. Sun, *Tissue Engineering Part A*, 2008, **14**, 41-48.
31. K. Nair, M. Gandhi, S. Khalil, K. C. Yan, M. Marcolongo, K. Barbee and W. Sun, *Biotechnology Journal*, 2009, **4**, 1168-1177.
32. A. Blaeser, D. F. Duarte Campos, U. Puster, W. Richtering, M. M. Stevens and H. Fischer, *Advanced Healthcare Materials*, 2016, **5**, 326-333.
33. S. Cosson and M. P. Lutolf, *Scientific Reports*, 2014, **4**, 4462.
34. F. Chiellini, R. Bizzarri, C. K. Ober, D. Schmaljohann, T. Yu, R. Solaro and E. Chiellini, *Macromolecular Rapid Communications*, 2001, **22**, 1284-1287.
35. Y. Zheng, J. Chen, M. Craven, N. W. Choi, S. Totorica, A. Diaz-Santana, P. Kermani, B. Hempstead, C. Fischbach-Teschl, J. A. López and A. D. Stroock, *Proceedings of the National Academy of Sciences*, 2012, **109**, 9342.
36. B. P. Casavant, E. Berthier, A. B. Theberge, J. Berthier, S. I. Montanez-Sauri, L. L. Bischel, K. Brakke, C. J. Hedman, W. Bushman, N. P. Keller and D. J. Beebe, *Proceedings of the National Academy of Sciences*, 2013, **110**, 10111.
37. S. B. Berry, T. Zhang, J. H. Day, X. Su, I. Z. Wilson, E. Berthier and A. B. Theberge, *Lab on a chip*, 2017, **17**, 4253-4264.
38. W. Lee, V. Lee, S. Polio, P. Keegan, J.-H. Lee, K. Fischer, J.-K. Park and S.-S. Yoo, *Biotechnology and Bioengineering*, 2010, **105**, 1178-1186.
39. Y. Lee, J. W. Choi, J. Yu, D. Park, J. Ha, K. Son, S. Lee, M. Chung, H.-Y. Kim and N. L. Jeon, *Lab on a chip*, 2018, **18**, 2433-2440.
40. J. Berthier, K. A. Brakke and E. Berthier, *Open Microfluidics*, Scrivener Publishing LLC, **Beverly, MA, USA** 2016.
41. C. A. DeForest and D. A. Tirrell, *Nature Materials*, 2015, **14**, 523.
42. I. Chen, B. M. Dorr and D. R. Liu, *Proceedings of the National Academy of Sciences*, 2011, **108**, 11399.
43. E. J. Su, S. Jeeawoody and A. E. Herr, *APL Bioengineering*, 2019, **3**, 026101.
44. C. Curtis, D. Toghani, B. Wong and E. Nance, *Colloids and Surfaces B: Biointerfaces*, 2018, **170**, 673-682.
45. P. Zarrintaj, S. Manouchehri, Z. Ahmadi, M. R. Saeb, A. M. Urbanska, D. L. Kaplan and M. Mozafari, *Carbohydrate Polymers*, 2018, **187**, 66-84.
46. E. Sodupe-Ortega, A. Sanz-Garcia, A. Pernia-Espinoza and C. Escobedo-Lucea, *Materials*, 2018, **11**.
47. D. F. Duarte Campos, A. Blaeser, M. Weber, J. Jäkel, S. Neuss, W. Jahnen-Dechent and H. Fischer, *Biofabrication*, 2012, **5**, 015003.
48. N. Brandenberg and M. P. Lutolf, *Advanced Materials*, 2016, **28**, 7450-7456.

49. D. Juncker, H. Schmid, U. Drechsler, H. Wolf, M. Wolf, B. Michel, N. de Rooij and E. Delamarche, *Analytical Chemistry*, 2002, **74**, 6139-6144.
50. D. G. Priest, N. Tanaka, Y. Tanaka and Y. Taniguchi, *Scientific Reports*, 2017, **7**, 17750.
51. E. R. Ruskowitz and C. A. DeForest, *Nature Reviews Materials*, 2018, **3**, 17087.
52. Y. C. Li, Y. S. Zhang, A. Akpek, S. R. Shin and A. Khademhosseini, *Biofabrication*, 2016, **9**, 012001.
53. B. A. Badeau and C. A. DeForest, *Annual Review of Biomedical Engineering*, 2019, **21**, 241-265.
54. P. M. Gawade, J. A. Shadish, B. A. Badeau and C. A. DeForest, *Advanced Materials*, 2019, **31**, 1902462.
55. E. R. Ruskowitz, M. P. Comerford, B. A. Badeau and C. A. DeForest, *Biomaterials Science*, 2019, **7**, 542-546.
56. B. A. Badeau, M. P. Comerford, C. K. Arakawa, J. A. Shadish and C. A. DeForest, *Nature Chemistry*, 2018, **10**, 251.
57. J. Valdez, C. D. Cook, C. C. Ahrens, A. J. Wang, A. Brown, M. Kumar, L. Stockdale, D. Rothenberg, K. Renggli, E. Gordon, D. Lauffenburger, F. White and L. Griffith, *Biomaterials*, 2017, **130**, 90-103.
58. E. Cambria, K. Renggli, C. C. Ahrens, C. D. Cook, C. Kroll, A. T. Krueger, B. Imperiali and L. G. Griffith, *Biomacromolecules*, 2015, **16**, 2316-2326.
59. S. R. Caliari and J. A. Burdick, *Nature methods*, 2016, **13**, 405-414.
60. H. S. Lim, J. T. Han, D. Kwak, M. Jin and K. Cho, *Journal of the American Chemical Society*, 2006, **128**, 14458-14459.
61. J. Berthier and K. A. Brakke, *The Physics of Microdroplets*, Wiley, Hoboken, NJ, USA, 2012.

Chapter 5 | Minaturizing Wet Scrubbers for Aerosolized Droplet Capture

Reproduced in part from U. N. Lee, T. L. van Neel,* F. Y. Lim, JW. Khor, J. He, R. S. Vaddi, A. Q. W. Ong, A. Tang, J. Berthier, J. S. Meschke, I. V. Novosselov,[#] A. B. Theberge,[#] E. Berthier,[#] "Miniaturizing wet scrubbers for aerosolized droplet capture." Analytical Chemistry, 2021, **93**, 11433–11441.*
** Equal contribution*
[#]Co-corresponding authors

UNL and TLV designed the device and conducted the experiments, FYL provided expertise in microbes, JK conducted some simulations, JH, RS, AQWO, and AT conducted trainings and provided expertise on capture efficiency experiments, JSM provided expertise in bioaerosols, IVN, ABT, and EB supervised and UNL, TLV, ABT and EB interpreted the results.

Abstract: Aerosols dispersed and transmitted through the air (e.g., particulate matter pollution, bioaerosols) are ubiquitous and one of the leading causes of adverse health effects and disease transmission. A variety of sampling methods (e.g., filters, cyclones, impactors) have been developed to assess personal exposures. However, a gap still remains in the accessibility and ease-of-use of these technologies for people without experience or training in collecting airborne samples. Additionally, wet scrubbers (large non-portable industrial systems) utilize liquid sprays to remove aerosols from the air; the goal is to "scrub" (i.e., clean) the exhaust of industrial smokestacks, not collect the aerosols for analysis. Inspired by wet scrubbers, we developed a device fundamentally different from existing portable air samplers by using aerosolized microdroplets to capture aerosols in personal spaces (e.g., homes, offices, schools). Our aerosol-sampling device is the size of a small teapot, can be operated without specialized training, and features a winding flow path in a supersaturated relative humidity environment enabling droplet growth. The integrated open mesofluidic channels shuttle coalesced droplets to a collection chamber for subsequent sample analysis. Here, we present the experimental demonstration of aerosol capture into water droplets. Iterative study optimized the non-linear flow manipulating baffles and enabled an 83% retention of the aerosolized microdroplets in the confined volume of our device. As a proof-of-concept for aerosol capture into a liquid medium, 0.5-3 μm model particles were used to evaluate aerosol capture efficiency. Finally, we demonstrate the device can capture and keep a bioaerosol (bacteriophage MS2) viable for downstream analysis

5.1 Introduction

We inhale a variety of aerosols (e.g., dust particles, ultrafine particulate matter (PM), biologically derived aerosols, and potentially infectious bioaerosols) on a daily basis.[1-3] When aerosols come into contact with the incredibly large surface area of the lungs, it can trigger and exacerbate allergic reactions, cause serious infections, and induce severe toxic reactions, particularly in immunocompromised individuals.[3-5] Despite years of research on the effects of aerosols on human health, our understanding of the extent specific types of aerosols can have on our short- and long-term health has focused largely on a number of salient aerosol types (e.g., cigarette smoke, PM2.5 particles)[6, 7] and environmental settings (hospitals, farms, etc.).[8-11] This is in part due to the fluctuating and highly personalized nature of an individual's exposure as the formation, dispersion, and transport of aerosols is influenced by both physical (e.g., size, shape, density of aerosols) and environmental (e.g., air currents, humidity, temperature) factors.[12, 13] Coupled with the limitations in personal sampling and ability to analyze chemical and biological composition of the collected sample, researchers and clinicians are still unable to pinpoint the patient-specific triggers for the millions of people worldwide affected by environmentally-induced respiratory illnesses. There is a need for a portable and easy-to-operate air-sampling device to inform individuals of their environmental exposures and provide information on personalized health triggers (Figure 5.1). In this work, we developed a lightweight and low-cost portable device that can be used without technical training; it utilizes liquid to capture aerosols for subsequent analysis—effectively miniaturizing technology used in industrial wet scrubbers. We aimed to maximize the time aerosolized microdroplets interact with aerosols to improve capture.

To date, a variety of passive[14] and active[15, 16] sampling devices have been developed for the collection of bioaerosols, including filter collection, centrifugal collection, electrostatic precipitation, liquid impingement, and impaction and direct collection onto growth media.[17-21] Information on aerosol concentration and size distribution can also be obtained in real-time using aerosol particle counters,[22-24] however, these monitors do not collect particles nor retain viable samples for further specific identification and analysis.[25] With respect to direct personal exposure monitoring, some of the aerosol collection methods

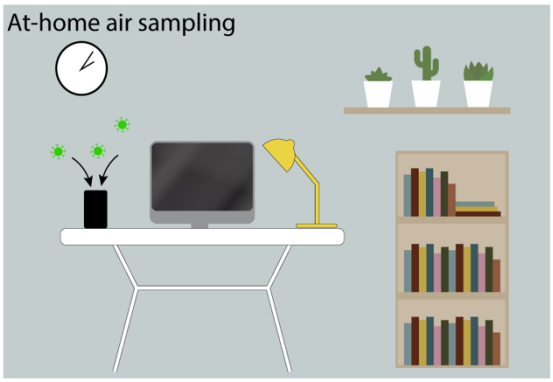

Figure 5.1. Schematic representation of our battery-powered air-sampling device (small black box to the left of the computer) collecting aerosols in a home environment to provide information on the landscape of aerosols in the room. The concept is that our device can be placed in any environment (e.g., homes, schools, hospitals, playgrounds, farms) and then sent back to a lab for analysis. See Figure 5.2 for a photograph of the battery-operated, compact device.

may not be practical; for example, filter collection and analysis is limited by high elution volumes, bulky setup, and high-power requirements. Due to the development in miniaturization of sampling pumps and electronics, exposure measurement methods including biological aerosol collectors[22-26] have rapidly advanced and gained popularity.[16, 27-30] For non-spore forming infectious bioaerosols (e.g., viruses and vegetative bacterial cells), desiccation during sampling is problematic for downstream viability analyses and infectivity studies.[31] Although bulk liquid and hydrated gel components integrated in established sampling devices have been shown to improve viability and culturability,[32] their large collection volume and substantial power requirements limit their applicability in personal samplers and analysis techniques where small collection volume and direct integration with microfluidic devices is desired.

An alternative to collection into bulk liquids are liquid droplet sprays similar to ones used in wet scrubbers.[33] These systems have been most effective for removing aerosols larger than 1 μm from the air, but they are large (ranging from the size of a small appliance to an industrial smokestack) and have high energy consumption.[34] The physical phenomena governing the capture of aerosol by droplets in gas flows has been simulated for wet scrubbers[35-37] and has shown that it is possible to increase the capture efficiency of aerosols (including those smaller than 1.0 μm) by decreasing the droplet size and increasing droplet residence time in the scubber.[37] The overall collection efficiency can be approximated by summing the

modes of capture – diffusion, interception, inertial impaction, and gravitational settling[36] – though most of these require large distances of timescales to operate effectively, which is difficult to achieve in a small scale device. The relationship between aerosol size and predominant mode of capture has previously been evaluated; impaction was found to be a predominant mode for the capture of aerosol sizes (d_p) > 5 μm, and diffusion for d_p < 1 μm.[35] At d_p < 0.05 μm, impaction and interception are negligible and diffusion can be considered as the sole mode of capture. Interception is unaffected by flow rate, but changes with droplet size and packing.[38] Industrial wet scrubbers generate the required liquid droplets using large spray towers. Alternatively, an attractive method for generating liquid microdroplets is ultrasonic atomizers due to their compact size and use in existing consumer products such as industry for home humidifiers. Recent studies using ultrasonic atomizers to generate sprays of liquid microdroplets showed a decrease in PM2.5 and PM10 concentration over time when the microdroplets were injected near burning incense.[39]

In this work, we harnessed the benefits of microdroplet liquid sprays to fill the need for an accessible and portable, at-home air-sampling device that collects aerosols in a liquid compatible with downstream analysis methods. To our knowledge, our device is the first battery-powered air-sampling device that uses aerosolized microdroplets to capture aerosols for analysis. We demonstrate the function and performance of the device using model fluorescent aerosol. Our results inform how the approach can be used for bioaerosol collection. The portable air-sampling device generates a mist of 4 μm liquid droplets and mixes it with aerosols. The device guides the mixture in a non-linear path to keep microdroplets suspended in the open spaces of the device for as long as possible. The droplet residence time (time the droplet spends suspended in a gas flow) along with droplet packing (number of droplets present) has been shown to increase capture efficiency.[37] We demonstrate that aerodynamic features enable the capture of the generated mist in a reduced volume and present optimization criteria for device geometry. By leveraging the principles of open microfluidics, we created a pathway via horizontal and vertical open mesofluidic channels for the coalesced droplets to travel and collect for future downstream analysis.[40, 41] We evaluate the effect of flow patterns on droplet retention efficiency and the model aerosol capture efficiency for a 0.5-3.0 μm size range. Finally, we demonstrate the device can capture and keep a bioaerosol viable for downstream analysis.

5.2 Design considerations

We developed a portable air-sampling device, approximately the size of a small teapot, that can be placed in many environments (homes, schools, hospitals, playgrounds, farms) for aerosol capture. Major considerations for the device included how to keep the device within a comfortable size to place on a desk, battery-powered to avoid the need of a power outlet, and simple to operate in a variety of environments. An additional consideration included maintaining the captured bioaerosols in liquid to ensure their viability and compatibility with rapid downstream analysis, a point of interest for future studies. While we focused the demonstration herein on manipulating airflow for microdroplet retention, we also used model inert particles to demonstrate the capability of the air-sampling device with bioaerosol applications in mind. An air-sampling device based on aerosolized microdroplets has the potential to capture a wide range of aerosols[34] and is amenable for use with a variety of liquid capture solutions (i.e., water, surfactant, media, and solvents). Given the efficacy of wet scrubbers, we chose to incorporate liquid droplets in our portable sampling device. Our air-sampling device consists of a small fan, an ultrasonic atomizer (droplet generator), and a 3D printed body (Figure 5.2A). The fan draws in air from the environment, and an ultrasonic atomizer generates 4 µm liquid droplets which move in the same direction as the air flow; the goal is for the liquid droplets to capture aerosols that enter through the fan. In our device, the microdroplets have an initial

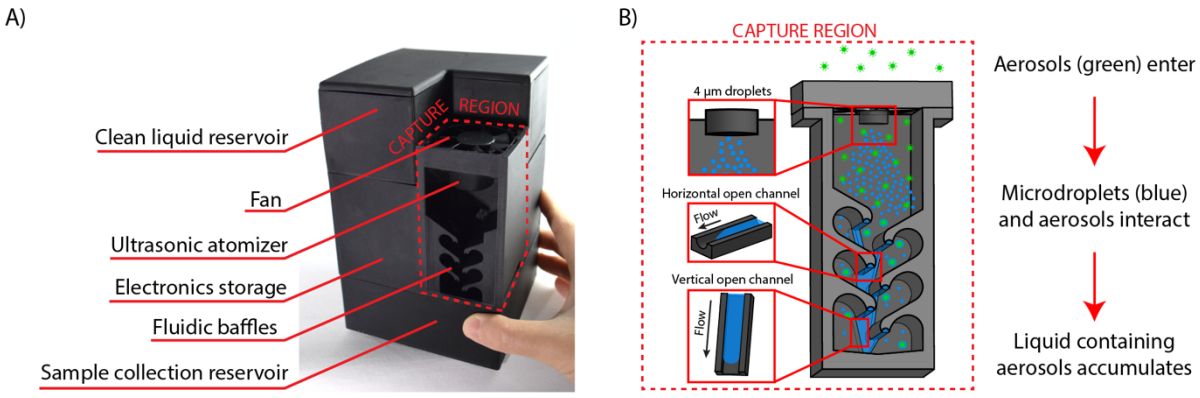

Figure 5.2. Portable droplet-based air-sampling device. (A) Photograph of device. (B) Schematic of capture region workflow. An ultrasonic atomizer generates 4 µm droplets (top), and horizontal (middle) and vertical (bottom) open mesofluidic channels collect coalesced droplets and aerosols. Aerosols enter through the fan, microdroplets intercept the aerosols, and six angled baffles guide the airflow to increase capture of aerosols. Front wall of the device has been removed for visualization of the device.

velocity that is independent of the air flow generated by the fan. Although the fan flow rate is tunable by adjusting the voltage delivered to the fan, the aerosol experiments and simulations in this manuscript were conducted with a flowrate of 6.3 slpm. Additionally, the initial velocity of the microdroplets is constant due to the designed frequency of the ultrasonic atomizer. The microdroplets and aerosols are carried in a non-linear path by the airflow generated by the fan and coalesce on fluidic baffles which will be discussed further in Figures 5.3 and 5.4. The baffles contain open mesofluidic channels that guide the coalesced droplets to a collection reservoir at the bottom of the device (Figure 5.2B). The clean liquid reservoir and sample collection reservoir were designed to each hold up to 200 mL of fluid for an operation time of 1 hour but the device is amenable to other volumes and operation times (Figure 5.2A). Electronic components (fan and ultrasonic atomizer) were made compatible for battery operation to improve overall portability, but the battery also limits the operation time (Figure D1). Due to the low pressure drop of the flow path, the device can be operated using low-cost fans, i.e., does not require pumps, typical for most of the widely used air-sampling devices today (e.g., Anderson cascade impactors, Burkard personal volumetric air sampler, Coriolis biological air sample, cyclones, and impingers).

5.3 Flow guiding baffles and open fluidic channels

The capture region of the air-sampling device was designed to increase interactions and mixing of microdroplets and aerosols. In traditional wet scrubbers, the droplet paths are linear, so to increase microdroplet residence times, it is necessary to increase the height of the device. In order to minimize the device size and maintain portability, we designed fluidic baffles that generate recirculation zones with longer residence time than the main airflow (Figure 5.3Ai). Air and droplets follow the flow paths and populate regions under each baffle due to a low Stokes Number (<0.03). Internal geometry of the flow channel consists of a series of horizontal open channels underneath the baffles, connected by a vertical open channel along the back wall (Figure 5.2B). The constriction bends to form an impinging jet on the upper surface of each baffle (Figure 5.3). The behavior of impinging jets has been described in the literature[42-44] and their comprehensive analysis is beyond the scope of this paper. However, for the purpose of this work, it is important to understand that angled impinging jets create stagnation regions (Figure 5.3Ai, left).

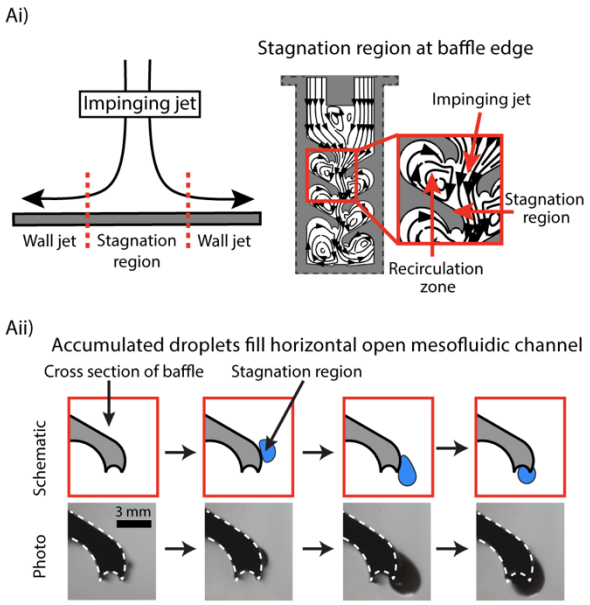

Figure 5.3. Impinging jet, stagnation region, and horizontal mesofluidic channels. (Ai) Basic schematic representation of an impinging jet (left) and the stagnation region in the device (right). (Aii) Droplets accumulate at a stagnation region on the baffle and migrate down the edge of the baffle, where it travels into the horizontal and vertical channels. Images were taken with a device that did not have a back wall, and water was colored dark blue to enable better visualization of the droplet.

In our device, the stagnation regions occur at the edge of the baffles; a portion of the jet follows the curve of the baffle (creating recirculation zones), and the remaining jet joins the bulk flow in the constriction (Figure 5.3Ai, right). Microdroplet growth and transition to liquid effluent is likely due to two complementary mechanisms: (i) microdroplet coalescence and (ii) heterogeneous growth in a supersaturated environment. These are similar to the growth of combustion-generated particles, where recirculating leads to the formation of large super-aggregates.[45, 46] It is challenging to model these processes, however, the highest probability of droplet coalescence and heterogeneous growth occurs in regions with long residence time and high droplet concentration. In our geometry, these conditions are present at the stagnation regions and in the recirculation zone. Once larger droplets are formed, they either settle on the surface due to gravity or via inertial impaction associated with the impinging jet. On the surface, these larger droplets migrate to the edge under the aerodynamic load acting on the droplet[47-50] or by gravity and are collected in the horizontal open mesofluidic channel embedded in the edge of the baffle (Figure 5.3Aii). The horizontal open channel guides the aerosol-laden sample toward the back wall where it meets the

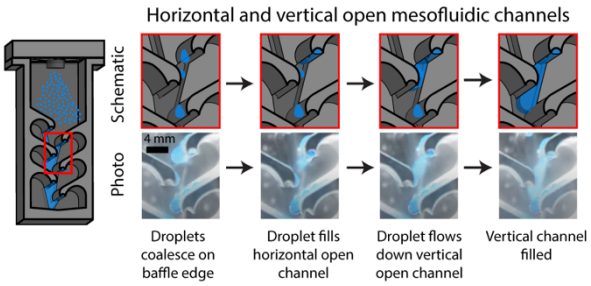

Figure 5.4. Schematic (top) and photo (bottom) progression of filling the mesofluidic channel at the edge of a baffle. Video was taken using a clear device to enable better visualization of the channel.

vertical open channel; this vertical open channel connects all of the baffles and drains the sample into a collection reservoir (Figure 5.4).

5.4 Computational modeling of airflow and effects of baffle geometry

Computational modeling aimed to (1) better visualize formation of recirculation zones and air flow around the baffles and (2) improve droplet retention within the device (reducing droplet loss through the outlet). The microdroplet-aerosol collisions were increased by incorporating baffles thus promoting the formation of recirculation zones. The multiple impinging jet flow pattern enables inertial impaction of droplets onto surfaces for capture. Using Computational Fluid Dynamics (CFD) COMSOL Multiphysics), we performed a parameter space optimization of the features in the capture region, specifically looking at how they affected airflow (Figure 5.5), and ultimately improved droplet retention (Figure 5.6). We solved for a mean air velocity field and pressure at a steady-state. We modeled a 2D cross-section to reduce computational load.[51] Recognizing the challenges associated with modeling and validation of aerosol-laden flow,[52] here CFD was used as a comparative tool to inform device design iterations and not as an absolute or quantitative method. The full details of the model are presented in the experimental section. Briefly, the following boundary conditions were used: a fully developed flow rate profile was used for the inlet with a zero-pressure outlet; all other walls were modeled with a no-slip boundary condition.

Experimentally, we observed droplets accumulating on all surfaces in the device, coalescing to form larger droplets, and being shuttled away by the mesofluidic channels to the collection area. Modeling the

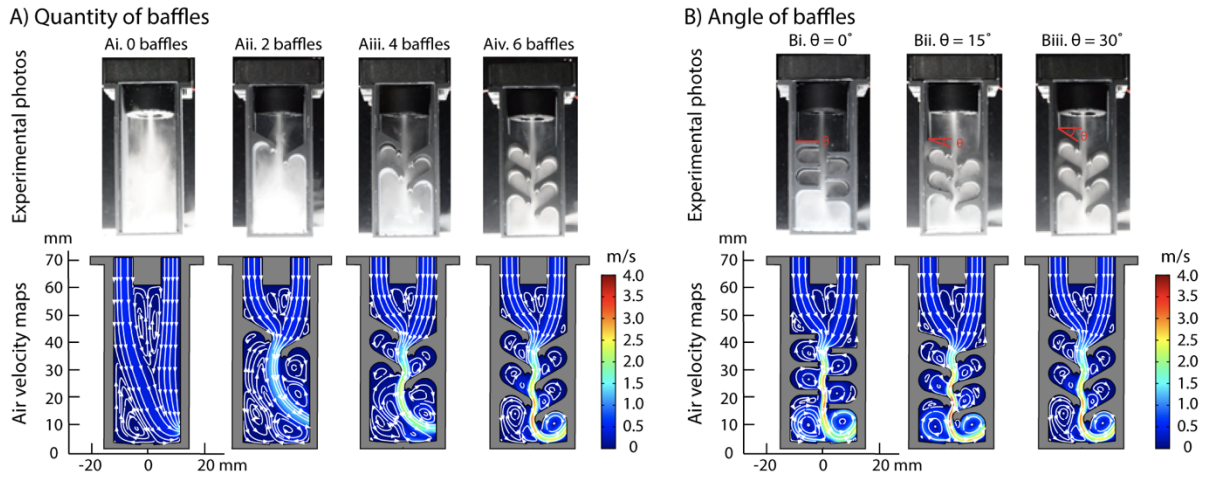

Figure 5.5. Effect of baffle quantity and angle on airflow. Experimental photos showing droplets in device and mean airflow velocity maps of a 2-D cross section of the device with (A) 0, 2, 4, and 6 baffles (all at a 30° angle) and (B) 0°, 15°, and 30° baffle angles. Images were taken from different timepoints and should not be compared with one another. Colors represent velocity and indicate the fluid flow (airflow) modeled. White lines and arrows represent direction of flow. Devices used in photos do not have front or back walls to enable visualization of the droplets.

mean airflow in the device enabled us to extract details such as the direction and pattern of the airflow; the flow within the device is laminar with a calculated Reynolds Number of less than 1200. To understand the effect of baffle geometry on recirculation zone formation and air flow, we varied the quantity and angle of the baffles (Figure 5.5). More recirculation zones were created with each additional set of baffles (Figure 5.5A). The baffles also increased the probability of droplet capture due to (i) increased surface to volume ratio and (ii) greater number of impinging jet regions where the high velocity interacts with the wall. This is supported by experimental droplet retention results shown in Figure 5.6. Further, each extra set of baffles constricts the main airflow resulting in an increased velocity of the impinging jet, allowing for more effective liquid transport from the stagnation regions to the mesofluidic channel (Figure 5.3). The horizontal space between the baffles controls the airflow constriction, but if too small can also cause backflow in the device. The number of stagnation regions increases with the quantity of baffles, providing more areas of high coalescence for droplets (Figure 5.3A). Finally, the pressure above the top baffles increases with each

additional set of baffles and decreases as the angle increases (Figure D2). Based on these observations, the six-baffle design was used in aerosol capture efficiency studies to be discussed in Figure 5.7.

5.5 Microdroplet retention efficiency

The microdroplets generated to capture aerosols in air must subsequently be captured by the device to perform analyses. The microdroplet capture process is challenging due to the high rate of air flow through the device and the need to not constrict that air flow. As the ultrasonic atomizer generates microdroplets and the fan draws aerosols into the device, an airflow exhaust must be designed to prevent flow exiting through the inlet in the case of high back pressure. An unobstructed geometry will lead to microdroplets flowing through the device without being captured. We sought to maximize the microdroplet retention while keeping an outlet to prevent backflow. The pressure drop associated with the impinging jet at stagnation regions helps coalesce the droplets on the baffles, however, it should not be high enough to cause backflow. We chose not to employ a mesh filter to increase microdroplet retention because recovering bioaerosols from filters can be damaging.[53] Additionally, droplets clog the small apertures in mesh surfaces which blocks airflow.

Through various design iterations, we measured the percentage of liquid retained by weighing the ultrasonic atomizer filled with water and the aerosol capture region of the device before and after operating the ultrasonic atomizer. Microdroplet retention increased with numbers of baffles with an 81% droplet retention in the six-baffle design (Figure 5.6Aiv). We also studied the effect of the angle of the baffle on microdroplet retention. There was an increase in microdroplet retention between 0° and 15° baffle angle followed by a decrease between 15° and 30° baffle angle. A 15° baffle angle had the largest microdroplet retention of 83%, while 0° and 30° baffle angle had a 73% and 81% microdroplet retention, respectively (Figure 5.6B). Since there was not a statistically significant difference in microdroplet retention between a 15° and 30° baffle angle, we chose to move forward with the 30° baffle angle due to the reduced pressure near the fan inlet, which is favorable in reducing backflow as discussed previously (Figure D2).

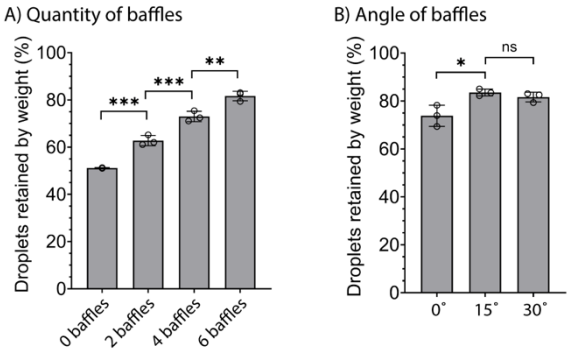

Figure 5.6. Effects of baffle quantity and angle on microdroplet retention. Microdroplet retention trends were determined by weighing liquid retained in the device before and after running the ultrasonic atomizer (see Experimental section). (A) The six-baffle design has the highest microdroplet retention (81.6% ± 1.6%) and was used for further device iteration studies. (B) The 15° baffle angle design retained a higher percentage of microdroplets (83.5% ± 1.1%) than a 0° baffle angle (73.8% ± 3.6%). No significant difference (ns) was observed with an additional 15° baffle angle (30°; 81.6% ± 1.6%). Bar graph represents the mean ± SD of n=3 experimental tests. One-way ANOVA with post-hoc Tukey's multiple comparison test; * $p<0.05$; ** $p<0.005$; *** $p<0.001$. Devices tested in (A) all had a 30° baffle angle.

5.6 Capture of model aerosols and a bioaerosol

An aerosol chamber[54] described previously was used to test the six-baffle, 30° baffle angle portable device for aerosol capture efficiency. Briefly, monodispersed fluorescent polystyrene latex spheres of varying sizes (0.5, 0.75, 1, 2, and 3 μm) were aerosolized in separate experiments using a nebulizer (Table D1). Two fans placed in opposite corners of the chamber were used to provide well-mixed conditions in the chamber. Three devices, co-located with reference filters, were tested in the chamber at the same time for 25-minutes. The reference filter flow rate matched the measured flow rate of our device (Figure D3). 25 mL of DI water was used to elute the particles from the filter and additional DI water was added to the device sample until the volume was also 25 mL. We measured the fluorescence of the liquid sample and used a ratio to determine aerosol collection efficiency. Particle sizes were selected based on model particles commonly used in bioaerosol research. The use of model polystyrene latex spheres for device testing was to avoid unnecessary exposure to bioaerosols (Table D2). It is important to note that we did not expect to reach 100% capture efficiency, nor is this required for analysis; further for bioaerosol detection, amplification steps (such as culture and PCR) can be employed. The highest efficiency observed in our device was 17.5% with 0.5 μm particles and the lowest efficiency was 4.5% with 2.0 um particles (Figure

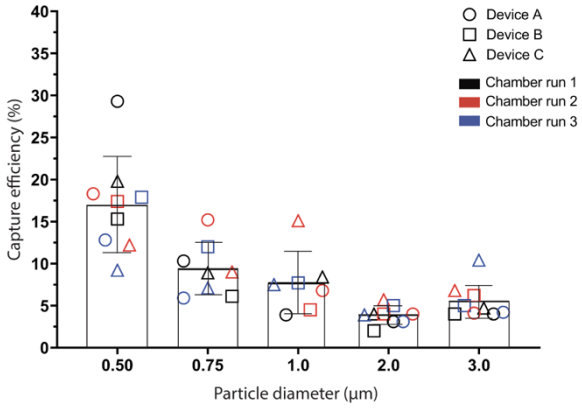

Figure 5.7. Capture efficiency of our portable air-sampling device (n=3 devices) for 0.5, 0.75, 1.0, 2.0, and 3.0 µm polystyrene particles. The highest aerosol capture efficiency observed was 17.5% with 0.5 µm particles and the lowest capture efficiency observed was 4.5% with 2.0 µm particles. Bar graphs represent mean ± SD of n=3 independent chamber runs for each device. Symbol shape indicates different device A, B, or C; symbol color indicates independent chamber runs.

5.7). Differences in aerosol capture efficiency were observed between the three devices tested, likely due to heterogeneity in the microdroplets produced by the ultrasonic mist generators (Figure D4) and inherent differences in the 3D printing of the devices. The reproducibility across devices could be improved with more accurate fabrication methods. Importantly, we note that variability in capture efficiency was also observed in reference filters used likely due to the manual control of the flow rate and particle nebulization (Table D3). Based on prior literature for other capture devices,[55-58] aerosol capture efficiency often varies with each particle size tested.

To demonstrate a potential application of our device in capturing bioaerosols while maintaining viability, we aerosolized a bacteriophage MS2 solution in a chamber with our device and analyzed the collected liquid from the device. MS2 is a virus that infects *E. coli* and is commonly used as a surrogate viral particle in aerosol studies for safety concerns.[59] Briefly, a MS2 solution was nebulized in a closed aerosol chamber containing a device for a 25-minute sampling period. As a control, we also performed a chamber run where no MS2 was nebulized. We then performed a plaque assay with the liquid samples collected from our device to determine if MS2 was present and viable. Plaque assays are used to quantify infectious viral particles.[63] The results from the control showed no MS2 (Figure 5.8, left). In comparison,

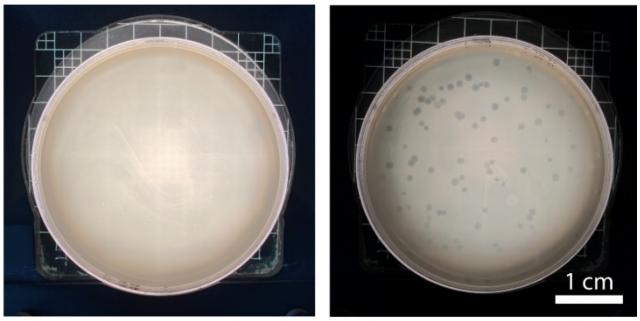

Figure 5.8. Bacteriophage MS2 captured in our air-sampling device remains viable. A plaque assay was performed using the liquid samples obtained from our device. A control liquid sample obtained from our device (no MS2 aerosolized in chamber) showed no plaques (left) when cultured with *E. coli*, demonstrating MS2 absence from the sample. In contrast, when MS2 was aerosolized in the chamber, plaques formed (dark grey circles; right) as a result of MS2 infecting *E. coli*, indicating MS2 presence in the sample. Representative images of n=2 independent chamber runs with one device.

samples from the chamber runs where MS2 was nebulized show MS2 was captured by the device and able to infect *E. coli*, an indication that the MS2 remained viable (Figure 5.8, right).

To our knowledge, our device is the first battery-powered air-sampling device that uses microdroplets to capture aerosols for analysis. The high humidity environment generated within the device coupled with storage of the captured aerosols in a fluid through the duration of the sampling period has the potential to keep bioaerosols viable for downstream culture and analysis; in this case, high capture efficiency is not critical to the identification of the captured bioaerosol because the sample can be amplified via culture (or detection methods like PCR). Additionally, the results were obtained with off-the-shelf low-cost components that can be further optimized to achieve higher efficiencies, however the device in its current state can be used in real-world environments. The bulk fluid also enables seamless integration with existing downstream analysis methods. To collect a sample from their environment, the only steps required by the user are: fill the reservoir with an appropriate fluid, flip the power switch, and put a cap on the collection reservoir after sampling. They would then mail the sample to a lab for analysis. Future work includes developing the sample preservation and analysis pipeline for bioaerosols of interest. We note that there are numerous considerations and validation steps required in future work including selection of media;

considerations will vary based on the analysis goal (e.g., simple detection of the presence of a microbe (yes/no) versus quantification). The platform introduced in this manuscript opens many avenues for future investigation.

5.7 Conclusion

In this work, we presented a portable air-sampling device that utilizes aerosolized microdroplets for aerosol capture. Future studies will focus on capture of bioaerosols for downstream analysis, viability studies, and infectivity assays. Our device is also well-positioned to be compatible with other low-viscosity fluids due to the working principles of the ultrasonic atomizer. Maximizing the capture of the liquid droplets after aerosolization by the ultrasonic atomizer will be part of future investigations to ensure the safety of expanding the use of potentially harmful fluids, such as organic solvents, as the capturing fluid. Ultimately our vision is that our air sampling platform will enable people who typically do not have access to or cannot afford services or products that measure environmental exposures (e.g., those in lower socioeconomic groups or high-risk environments), to collect air samples and determine the levels of environmental exposure within their daily lives.

5.8 Materials and methods

Device fabrication: The body of the device and ultrasonic atomizer cup were designed in Solidworks 2017 and 3D printed out of black resin (RS-F2-GPBK-04) using a Form 2 or Form 3 stereolithography 3D printer (Formlabs). The parts were cleaned in isopropyl alcohol (IPA) for 10 minutes in a FormWash (Formlabs) and rinsed down with clean IPA to remove excess uncured resin. The devices were dried with compressed air and cured under a 395-405 nm 20W UV lamp (Quans) for 1 hour. A 1.3 mm PS thick window was milled (Datron Neo) to enable visual access to the capture region of the device.

Portable Electronics (Figures 5.2A and 5.6): The ultrasonic atomizer (Comidox) with a frequency of 113 KHz and 730 apertures 5 μm in diameter was adhered to the floor of the ultrasonic atomizer cup with 100% silicone caulk (Gorilla Glue). A 40 mm square computer fan (Model OD4010-05HB55, Orion Fans) was used to generate airflow. The voltage delivered to the fan was controlled by a microcontroller (Arduino

Micro, Arduino). A darlington transistor (TIP122, STMicroelectronics), 100 Ohm resistor (SparkFun Electronics), 22 and 24 AWG jumper wires (OSEPP Electronics LTD), and 2.1 mm male and female barrel jacks (Centropower) were used. The device was powered by a 9V battery (Zeus Battery Products).

Simulations (Figure 5.5): Computational Fluid Dynamics Module in COMSOL Multiphysics v5.5 software was used to simulate the air flow and pressure in different device geometries in a stationary study. A 2D cross-section of our 3D device was modeled. The *Laminar Flow* physics interface, governed by the Navier-Stokes equations, was selected to model air flow in the device based on the estimated Reynolds number calculated (Re<1200). Two fan inlets with a fully developed flow profile, initial flow rate = 6.3 L/min, and entrance thickness of 0.02 m was used. An outlet boundary was defined by P=0 Pa with backflow suppressed. No slip boundary conditions were applied to all remaining boundaries. A fine element quadrilateral mesh with extra fine element boundary refinement at the baffles was used.

Droplet retention gravimetric analysis using non-portable electronics setup (Figure 5.**6):** Droplet retention was measured by weighing the ultrasonic atomizer cup filled with water and the 3D printed body separately using an analytical balance (Mettler Toledo ME103E) before and after operating the device for 30 seconds with the fan operating at 25% voltage for an airflow rate of 6.3 L/min.

Aerosol capture efficiency (Figure 5.7): A testing chamber (0.56 x 0.52 x 0.42 m) was used to determine the capture efficiency of our device using fluorescent polystyrene latex (PSL) particles (Fluoresbrite® YG Microspheres, Polysciences Inc.); particle sizes tested: 0.5, 0.75, 1, 2, and 3 μm. The particles were diluted in DI water and aerosolized using a VixOne Nebulizer (Westmed Inc.); each particle size had a dedicated nebulizer to prevent contamination of other particles sizes. An aerodynamic particle sizer (APS 3321, TSI Inc.) was used to monitor the particle size aerosolized and particle concentration during experimental runs. Particle concentration varied by size; see Table D1 for more information. Three open-face aerosol reference filter holders (EMD Millipore, Model #XX5004710) with 0.2 μm PTFE Omnipore membrane filters (Millipore Sigma, product #JGWP04700) were co-located with our air-sampling devices in the chamber to collect particles; filter membranes were collected for analysis Flow rates for reference filters placed in the chamber were calibrated using a mass flow meter (TSI Inc., Model #4140) to 3.15 slpm (half the flow rate

of our device due to limitations in the flow controller). A humidity monitor [(Extech Instruments, Model #SD700; AcuRite, Model #01083M)] and a dry airline in the chamber was used to keep the humidity between 60-70%. An interchangeable particle capture region was pre-wetted before placing the fully assembled devices into the chamber; the sampling region in the device was replaced between chamber runs. Devices and reference filters captured particles for 25 minutes followed by a 3-minute chamber purge before devices being removed from the chamber. A 1 oz. polystyrene cup collected the sample (Uline, product #S-14487) and was weighed (Smart Weigh Pro Pocket Scale TOP500, Amazon) before and after chamber runs. Sampling regions were rinsed down with approximately 5 mL of DI water after chamber runs. All samples were diluted to 25 g (25 mL) using DI water which matched the volume of water used for the reference filters. Reference filters were carefully placed in 50 mL polypropylene centrifuge tubes (ThermoFisher, product #339652) with 25 mL DI water.

Fluorescence measurements (Figure 5.7): Capture efficiency was calculated as 100 x (fluorescence of samples from our device/fluorescence of co-located reference filter). Fluorescence measurements were performed using a fluorometer set to a gain of 200 (Sequoia-Turner model 450). Sample cups and centrifuge tubes containing the reference filters were vortexed (Vortex-Genie 2, Scientific Industries, Inc.) for at least 8 minutes at 1800 RPM and remained vortexing until analysis. A 5 mL aliquot of the sample was transferred to a 12x75 mm borosilicate disposable culture tube (Fisherbrand, Cat No. 14-961-26) and discarded to rinse the tube of any previous sample. The sample was re-aliquoted into the test tube and measured then discarded, for a total of three measurements. Between each aliquot, the pipette was used to resuspend the particles in the sample cup once before measurement. A new glass test tube was used for each particle size on any given day. Blank measurements were always taken when switching to a new glass test tube. Calibration curves for each particle size are available in Figure D5. Blank measurements were subtracted from sample and reference fluorescent values prior to additional calculations and statistical analyses.

MS2 aerosolization and analysis (Figure 5.8): A testing chamber operating similarly to the one described previously was used to determine if our device was capable of capturing a bioaerosol (bacteriophage MS2 ATCC #15597-B1; see SI for more information on propagation). A 1-mL MS2 solution (1.9×10^{11} PFU)

was aerosolized (VixOne Nebulizer) in a closed chamber. An aerodynamic particle sizer (APS 3321, TSI Inc.) was used to monitor the particle concentration during experimental runs. A 25-minute sampling period followed by a 5 min purge was used. Device samples collected in the 1-oz. polystyrene cups were collected with no further dilution. A double agar layer plaque assay was performed to assess MS2 viability in a bacterial host (*Escherichia coli*). Briefly, Tryptic Soy Agar (TSA) (BD Difco #236950) was prepared following manufacturer's directions, added to petri dishes (Fisherbrand 100x15mm #FB0875712), and allowed to cool at room temperature. A ten-fold serial dilution was performed using 1X PBS for all samples. 100 µL of diluted sample and 100 µL of an *E. coli* Famp (ATCC #700891) suspension were added to 7 mL of top agar [0.5% (w/v) NaCl (Fisher Scientific #S271-500) and 0.7% (w/v) Bacto Agar (BD #214010)] in a borosilicate glass tube (Fisherbrand #14-961-27) after which the solution was mixed by rolling tube between hands and subsequently poured onto prepared TSA plates; top agar was cooled before plates were inverted and incubated overnight at 37 °C. Plaques were counted the following day. The assay was performed in duplicate for all sample dilutions, including undiluted samples. Additionally, a negative control (only *E. coli*) and PBS control (PBS added in place of sample) were also included.

Data analysis: All data and statistical analyses were performed using Prism v9.0 (GraphPad) software.

5.9 References

1. J. H. Ware, J. D. Spengler, L. M. Neas, J. M. Samet, G. R. Wagner, D. Coultas, H. Ozkaynak and M. Schwab, *Am J Epidemiol*, 1993, **137**, 1287-1301.
2. G. P. Pappas, R. J. Herbert, W. Henderson, J. Koenig, B. Stover and S. Barnhart, *Int J Occup Environ Health*, 2000, **6**, 1-8.
3. J. E. Thompson, *J Occup Environ Med*, 2018, **60**, 392-423.
4. I. Manisalidis, E. Stavropoulou, A. Stavropoulos and E. Bezirtzoglou, *Front Public Health*, 2020, **8**, 14.
5. E. R. Tovey, M. D. Chapman, C. W. Wells and T. A. Platts-Mills, *Am Rev Respir Dis*, 1981, **124**, 630-635.
6. B. J. Apelberg, L. M. Hepp, E. Avila-Tang, L. Gundel, S. K. Hammond, M. F. Hovell, A. Hyland, N. E. Klepeis, C. C. Madsen, A. Navas-Acien, J. Repace, J. M. Samet and P. N. Breysse, *Tob Control*, 2013, **22**, 147-155.
7. C. A. Pope, 3rd and D. W. Dockery, *J Air Waste Manag Assoc*, 2006, **56**, 709-742.
8. J. Y. Choi, J. Zemke, S. E. Philo, E. S. Bailey, M. Yondon and G. C. Gray, *Front Public Health*, 2018, **6**, 174.
9. R. E. Stockwell, E. L. Ballard, P. O'Rourke, L. D. Knibbs, L. Morawska and S. C. Bell, *J Hosp Infect*, 2019, **103**, 175-184.
10. C. Alonso, P. C. Raynor, S. Goyal, B. A. Olson, A. Alba, P. R. Davies and M. Torremorell, *J Vet Diagn Invest*, 2017, **29**, 298-304.

11. M. Śmiełowska, M. Marć and B. Zabiegała, *Environ Sci Pollut Res Int*, 2017, **24**, 11166-11176.
12. Y. Wu, A. Calis, Y. Luo, C. Chen, M. Lutton, Y. Rivenson, X. Lin, H. C. Koydemir, Y. Zhang, H. Wang, Z. Göröcs and A. Ozcan, *ACS Photonics*, 2018, **5**, 4617-4627.
13. P. Srikanth, S. Sudharsanam and R. Steinberg, *Indian J Med Microbiol*, 2008, **26**, 302-312.
14. J. Namieśnik, B. Zabiegała, A. Kot-Wasik, M. Partyka and A. Wasik, *Anal Bioanal Chem*, 2005, **381**, 279-301.
15. I. Lee, Y. Seok, H. Jung, B. Yang, J. Lee, J. Kim, H. Pyo, C. S. Song, W. Choi, M. G. Kim and J. Lee, *ACS Sens*, 2020, **5**, 3915-3922.
16. J. Volckens, C. Quinn, D. Leith, J. Mehaffy, C. S. Henry and D. Miller-Lionberg, *Indoor Air*, 2017, **27**, 409-416.
17. T. Reponen, in *Exposure to Microbiological Agents in Indoor and Occupational Environments* , eds. S. Viegas, C. Viegas, A. Gomes, M. Taubel and R. Sabino, Springer International Publishing , 1 edn., 2017, DOI: 10.1007/978-3-319-61688-9 , ch. 4.
18. J. Kesavan and J.-L. Sagripanti, *Environmental Science: Processes & Impacts*, 2015, **17**, 638-645.
19. C. H. Wang, B. T. Chen, B. C. Han, A. C. Liu, P. C. Hung, C. Y. Chen and H. J. Chao, *PLoS One*, 2015, **10**, e0120308.
20. S. A. Grinshpun, M. P. Buttner, G. Mainelis and K. Willeke, in *In Manual of Environmental Microbiology* eds. M. V. Yates, C. H. Nakatsu, R. V. Miller and S. D. Pillai, Fourth Edition edn., 2016, DOI: https://doi.org/10.1128/9781555818821.ch3.2.2, ch. 3.2.2.
21. V. Aizenberg, T. Reponen, S. A. Grinshpun and K. Willeke, *AIHAJ - American Industrial Hygiene Association*, 2000, **61**, 855-864.
22. J. M. Roux, R. Sarda-Estève, G. Delapierre, M. H. Nadal, C. Bossuet and L. Olmedo, *Environmental Science and Pollution Research*, 2016, **23**, 8175-8183.
23. T. T. Han, N. M. Thomas and G. Mainelis, *Aerosol Science and Technology*, 2017, **51**, 903-915.
24. T. G. Foat, W. J. Sellors, M. D. Walker, P. A. Rachwal, J. W. Jones, D. D. Despeyroux, L. Coudron, I. Munro, D. K. McCluskey, C. K. L. Tan and M. C. Tracey, *Journal of Aerosol Science*, 2016, **95**, 43-53.
25. I. V. Novosselov, R. A. Gorder, J. A. Van Amberg and P. C. Ariessohn, *Aerosol Science and Technology*, 2014, **48**, 822-830.
26. J. He, N. K. Beck, A. L. Kossik, J. Zhang, E. Seto, J. S. Meschke and I. Novosselov, *PLOS ONE*, 2018, **13**, e0197783.
27. K. A. Koehler and T. M. Peters, *Curr Environ Health Rep*, 2015, **2**, 399-411.
28. R. Chartier, M. Phillips, P. Mosquin, M. Elledge, K. Bronstein, S. Nandasena, V. Thornburg, J. Thornburg and C. Rodes, *Indoor Air*, 2017, **27**, 147-159.
29. J. Cai, B. Yan, J. Ross, D. Zhang, P. L. Kinney, M. S. Perzanowski, K. Jung, R. Miller and S. N. Chillrud, *Aerosol Air Qual Res*, 2014, **14**, 1-9.
30. G. E. Duncan, E. Seto, A. R. Avery, M. Oie, G. Carvlin, E. Austin, J. H. Shirai, J. He, B. Ockerman and I. Novosselov, *JMIR Mhealth Uhealth*, 2018, **6**, e12023.
31. Z. Wang, T. Reponen, S. A. Grinshpun, R. L. Górny and K. Willeke, *Journal of Aerosol Science*, 2001, **32**, 661-674.
32. W. D. Griffiths*, I. W. Stewart, J. M. Clark and I. L. Holwill, *Aerobiologia*, 2001, **17**, 109-119.
33. J. R. Kastner and K. C. Das, *J Air Waste Manag Assoc*, 2002, **52**, 459-469.
34. D. Mussatti and P. Hemmer, *Journal*, 2002.
35. C. H. Jung and K. W. Lee, *Environmental Engineering Science*, 2007, **24**, 257-266.
36. T. Gemci and F. Ebert, *Journal of Aerosol Science*, 1992, **23**, 769-772.
37. H. T. Kim, C. H. Jung, S. N. Oh and K. W. Lee, *Environmental Engineering Science*, 2001, **18**, 125-136.
38. K. W. Lee, *Journal of Aerosol Science*, 1981, **12**, 79-87.
39. J. Kim, J. J. Kim and S. J. Lee, *Building and Environment*, 2020, **175**, 106797.

40. E. Berthier, A. M. Dostie, U. N. Lee, J. Berthier and A. B. Theberge, *Analytical Chemistry*, 2019, **91**, 8739-8750.
41. B. P. Casavant, E. Berthier, A. B. Theberge, J. Berthier, S. I. Montanez-Sauri, L. L. Bischel, K. Brakke, C. J. Hedman, W. Bushman, N. P. Keller and D. J. Beebe, *Proceedings of the National Academy of Sciences*, 2013, **110**, 10111.
42. L. J. Clancy, 1975.
43. P. Fillingham, H. Murali and I. V. Novosselov, *Journal of Fluids Engineering*, 2017, **139**.
44. P. Fillingham and I. V. Novosselov, *International Journal of Heat and Fluid Flow*, 2020, **81**, 108516.
45. R. K. Chakrabarty, I. V. Novosselov, N. D. Beres, H. Moosmüller, C. M. Sorensen and C. B. Stipe, *Applied Physics Letters*, 2014, **104**, 243103.
46. J. Davis, K. Tiwari and I. Novosselov, *Fuel (Lond)*, 2019, **245**, 447-457.
47. J. W. Cleaver and B. Yates, *Journal of Colloid and Interface Science*, 1973, **44**, 464-474.
48. M. E. O'Neill, *Chemical Engineering Science*, 1968, **23**, 1293-1298.
49. P. Fillingham, K. Kottapalli, X. Zhan and I. V. Novosselov, *Journal of Aerosol Science*, 2019, **128**, 89-98.
50. P. Fillingham, R. S. Vaddi, A. Bruning, G. Israel and I. V. Novosselov, *Powder Technology*, 2021, **377**, 958-965.
51. J. Blazek, in *Computational Fluid Dynamics: Principles and Applications (Third Edition)*, ed. J. Blazek, Butterworth-Heinemann, Oxford, 2015, DOI: https://doi.org/10.1016/B978-0-08-099995-1.00001-4, pp. 1-407.
52. R. C. Petersen, A. G. Hallar, I. B. McCubbin, J. A. Ogren, E. Andrews, D. Lowenthal, R. Gorder, R. Purcell, D. Sleeth and I. Novosselov, *Aerosol Science and Technology*, 2019, **53**, 712-727.
53. W. G. Lindsley, B. J. Green, F. M. Blachere, S. B. Martin, B. F. Law, P. A. Jensen and M. P. Schafer, *Journal*, 2017, 2-115.
54. J. He and I. V. Novosselov, *Aerosol Science and Technology*, 2017, **51**, 1016-1026.
55. J. Gordon, P. Gandhi, G. Shekhawat, A. Frazier, J. Hampton-Marcell and J. A. Gilbert, *Microbiome*, 2015, **3**, 79.
56. H. R. An, G. Mainelis and M. Yao, *Indoor Air*, 2004, **14**, 385-393.
57. S. E. Mischler, E. G. Cauda, M. Di Giuseppe and L. A. Ortiz, *Journal of Occupational and Environmental Hygiene*, 2013, **10**, 685-693.
58. H. J. Walls, D. S. Ensor, L. A. Harvey, J. H. Kim, R. T. Chartier, S. V. Hering, S. R. Spielman and G. S. Lewis, *Aerosol Science and Technology*, 2016, **50**, 802-811.
59. G. T. Machado, C. R. C. Pinto, L. A. V. da Fonseca, T. Ramos, T. F. P. Paggi and B. Spira, *Arch Microbiol*, 2021, DOI: 10.1007/s00203-021-02382-8, 1-9.

Chapter 6 | Conclusion and Future Directions

This dissertation contributes to the diversity of fields open microfluidics can be applied to for technology development. From mining new knowledge in the fundamentals of open droplet microfluidics to usage in environmental air sampling and tissue engineering, open microfluidics is a continually growing field. Deployment of the technologies presented in this dissertation has the potential to result in impactful discoveries and new knowledge in the environment and human health fields. They are designed with the end user in mind and special attention was made to ensure they are simple to operate for people with various levels of training from researchers to non-specialists.

Chapter 2 serves as the first analysis of rapid injection molding for open microfluidic assays and details the geometries and design considerations necessary for successful rapid injection molding of polystyrene, polypropylene, and cyclic olefin copolymer—the most common thermoplastics used in cell culture ware. Chapter 3 introduces a novel open microfluidic droplet generator wherein droplets are formed by leveraging the inherent hydrostatic and capillary pressure. The use of hydrofluoroether (HFE)—a common fluorinated carrier fluid in traditional droplet microfluidics that is compatible with cell biology—emphasized the compatibility of this method to biological applications. In addition, PTFE was instrumental to the success of this method because the physical properties enabled the aqueous droplets to flow and autonomously be generated. Chapter 4 lays out the advancement of a hydrogel patterning method originally published in Berry and Zhang et al. from two dimensions to three dimensions. We showed that layer-by-layer hydrogel patterning with open microfluidics enables multi-material and multi-cell structures. The geometries displayed include overhanging features, asymmetric features, and fully enclosed gels which is particularly enabling for tissue engineering, 3D cell culture, and organoid development where multiple cell types and supporting material are needed to recapitulate the cellular environment. Lastly, chapter 5 presents a novel technology for capturing airborne particles and bioaerosols with microdroplets. Open microfluidic channels are used to guide the droplets to a collection region for downstream analysis.

The implementation of open microfluidics into technology for human health and the environment has gained momentum over the last several years and the technologies discussed in this dissertation contribute

to the growing body of technology leveraging open microfluidics. Follow up investigations on the open droplet generation include further leveraging the Cheerio effect for droplet manipulation and investigating droplet merging phenomena. Additionally, droplet monodispersity and throughput may be optimized with higher resolution fabrication methods. The 3D patterning technology can be optimized to be used with other biologically relevant hydrogels such as Matrigel and various concentrations of collagen. Also, the resolution of different hydrogels is still unknown. Lastly, the microdroplet air sampler can be further optimized for capture efficiency and droplet retention with design modifications such as surface treatments and fan placement to prevent bioaerosol losses on the device. Critical to the usefulness of this technology will be testing it in ambient real-world environments and preparing the sample for analysis which might require several analytical techniques. On-device sample analysis is a future body of work that can advance the impact of the microdroplet air sampler.

Appendix

A. Appendix for Chapter 2

Reproduced in part from U. N. Lee, E. Berthier, X. Su, J. Guckenberger, A. M. Dostie, T. Zhang, and A. B. Theberge, "Fundamentals of injection molding for cell-based microfluidics." Lab on a Chip, 2018, ***18****, 496–504.*

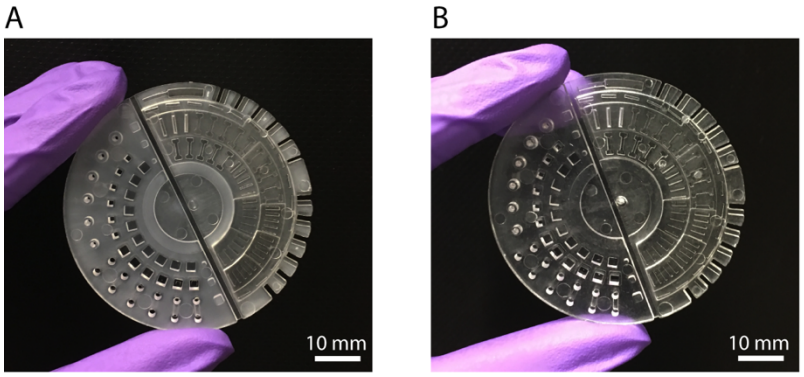

Figure A1. Image of PP device (left) and COC device (right).

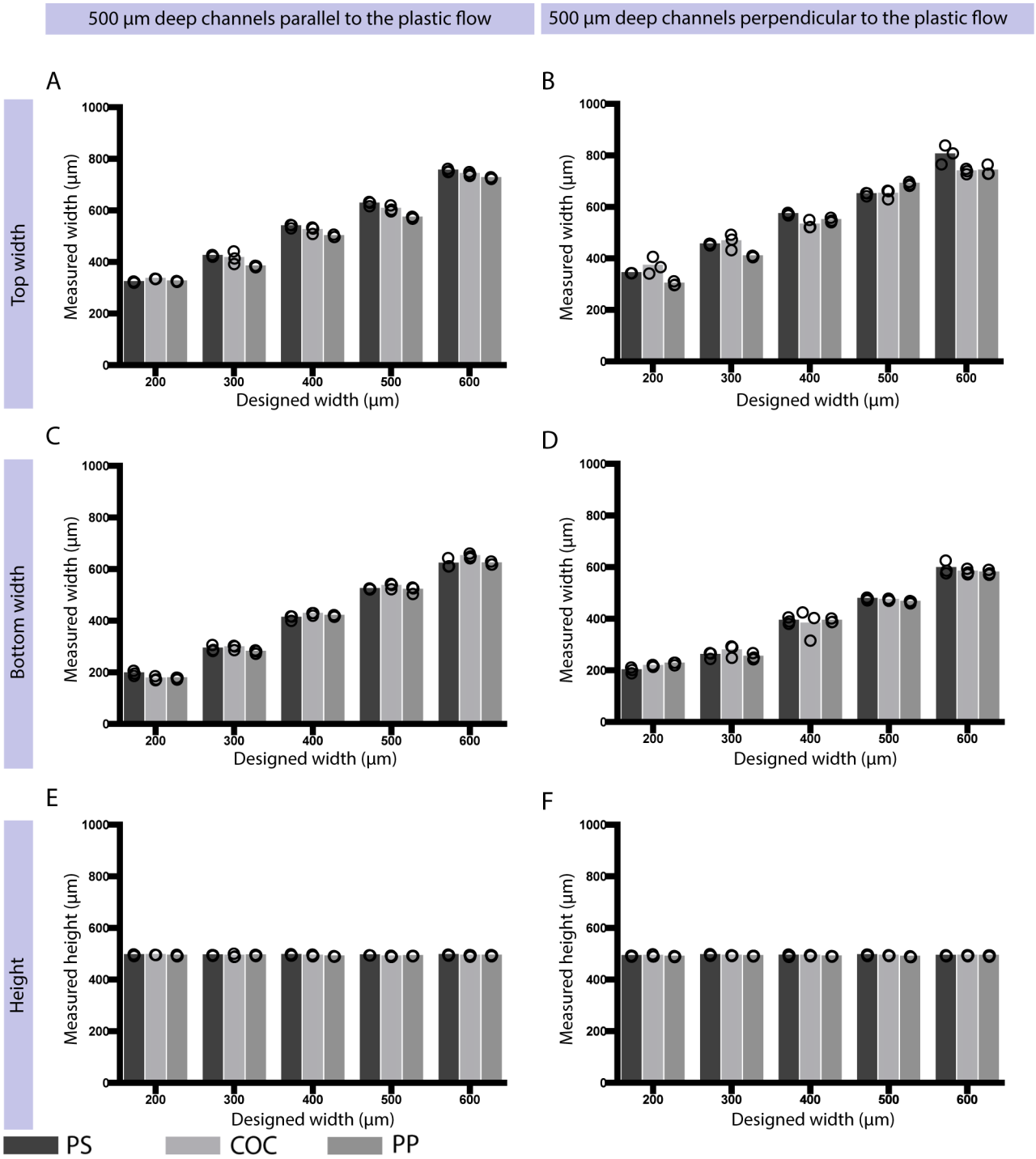

Figure A2. Measured dimensions of 500 µm deep rectangular channels in PS, COC, and PP devices. Channels are oriented parallel (left) or perpendicular (right) to the flow of molten plastic. Data points indicate three devices tested in each material. Data points (open circles plotted on top of bar graphs) indicate three devices measured (all from the same metal mold); bars indicate the mean.

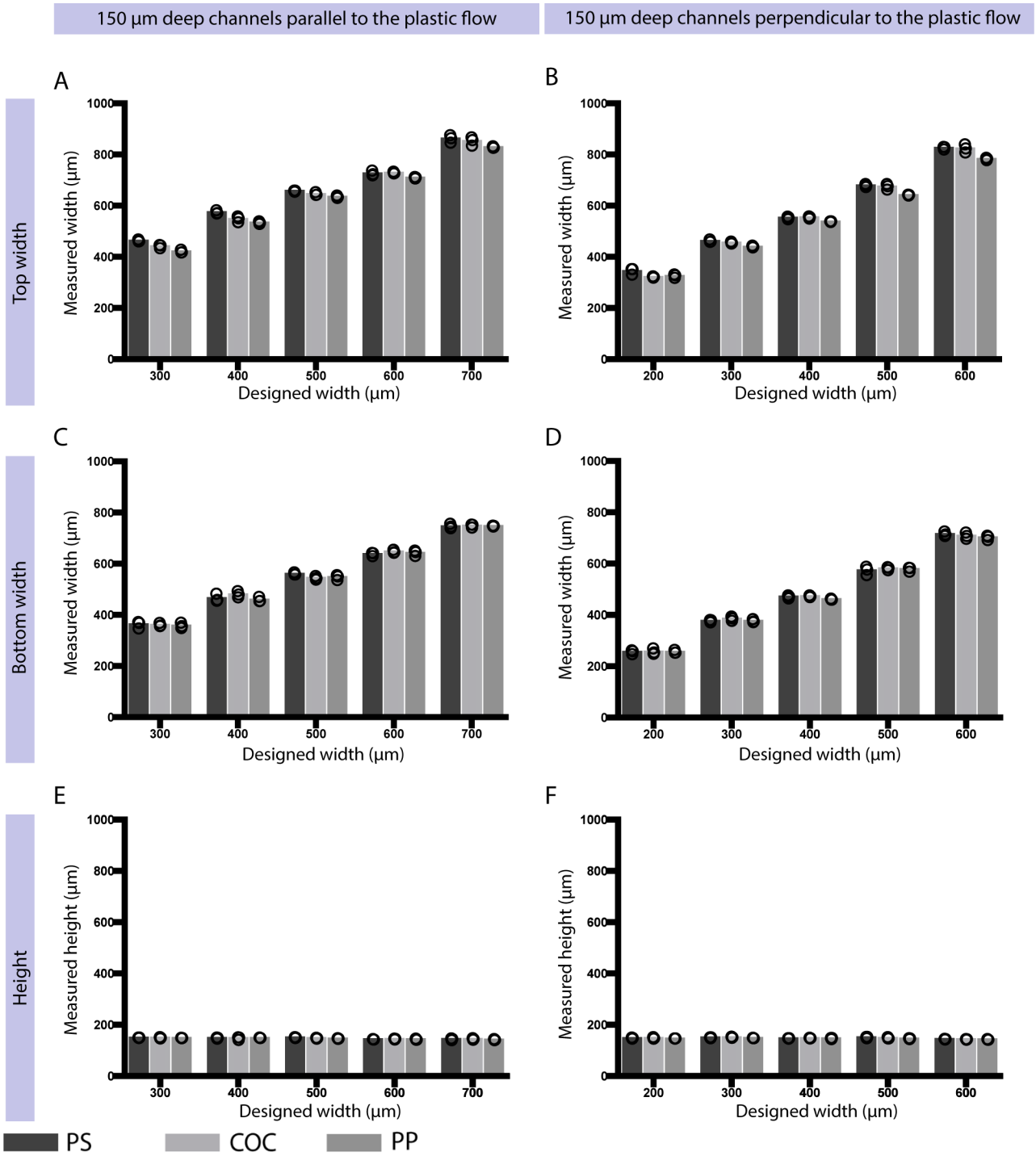

Figure A3. Measured dimensions of 150 µm deep rectangular channels in PS, COC, and PP devices. Channels are oriented parallel (left) or perpendicular (right) to the flow of molten plastic. Data points indicate three devices tested in each material. Data points (open circles plotted on top of bar graphs) indicate three devices measured (all from the same metal mold); bars indicate the mean.

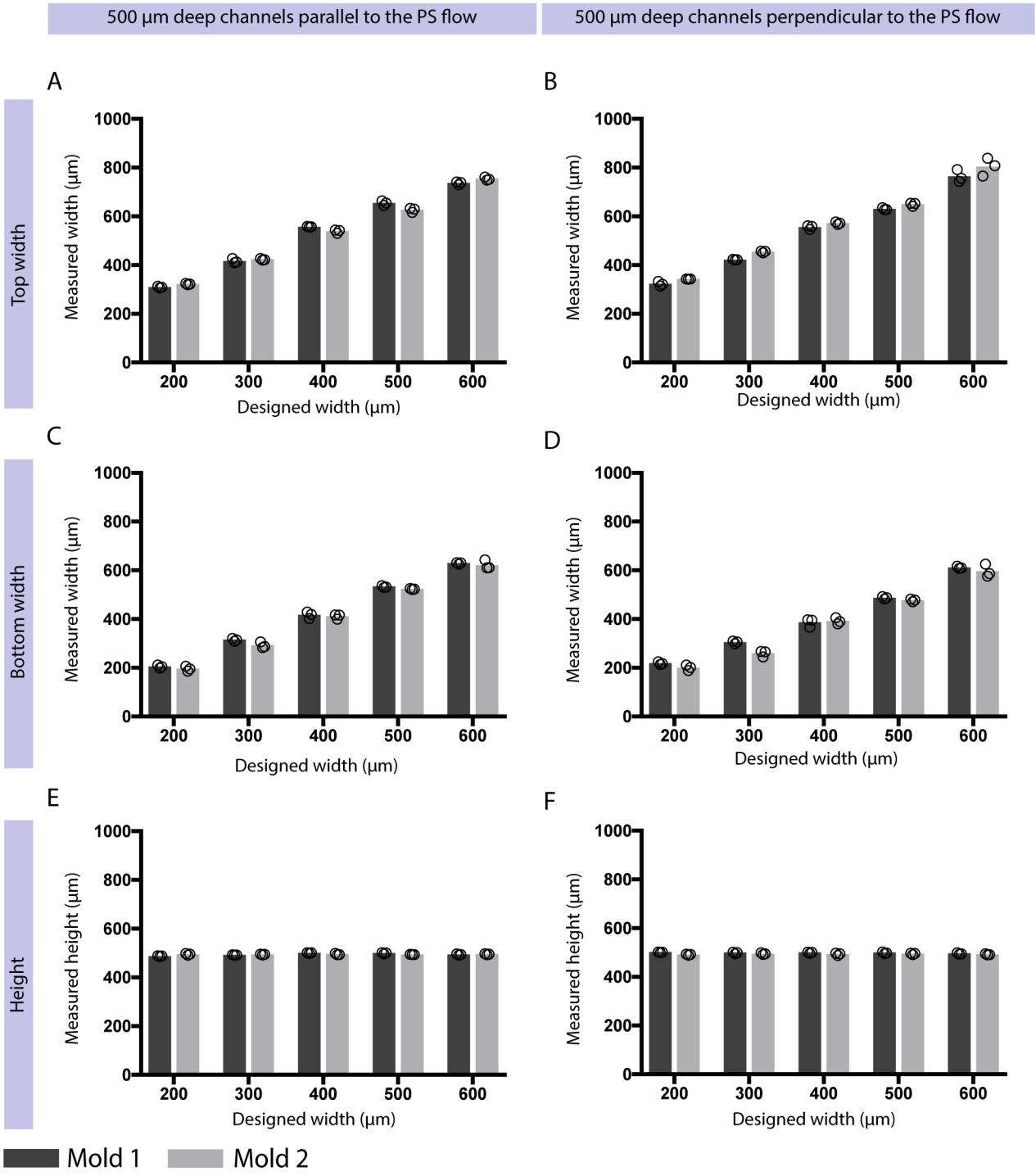

Figure A4. Quantification of channel dimensions from devices injection molded out of two identically designed molds. Graphs of mold 1 and mold 2 for 500 µm deep rectangular channels parallel (left) and perpendicular (right) to molten PS flow. Data points (open circles plotted on top of bar graphs) indicate three devices measured (all from the same metal mold); bars indicate the mean.

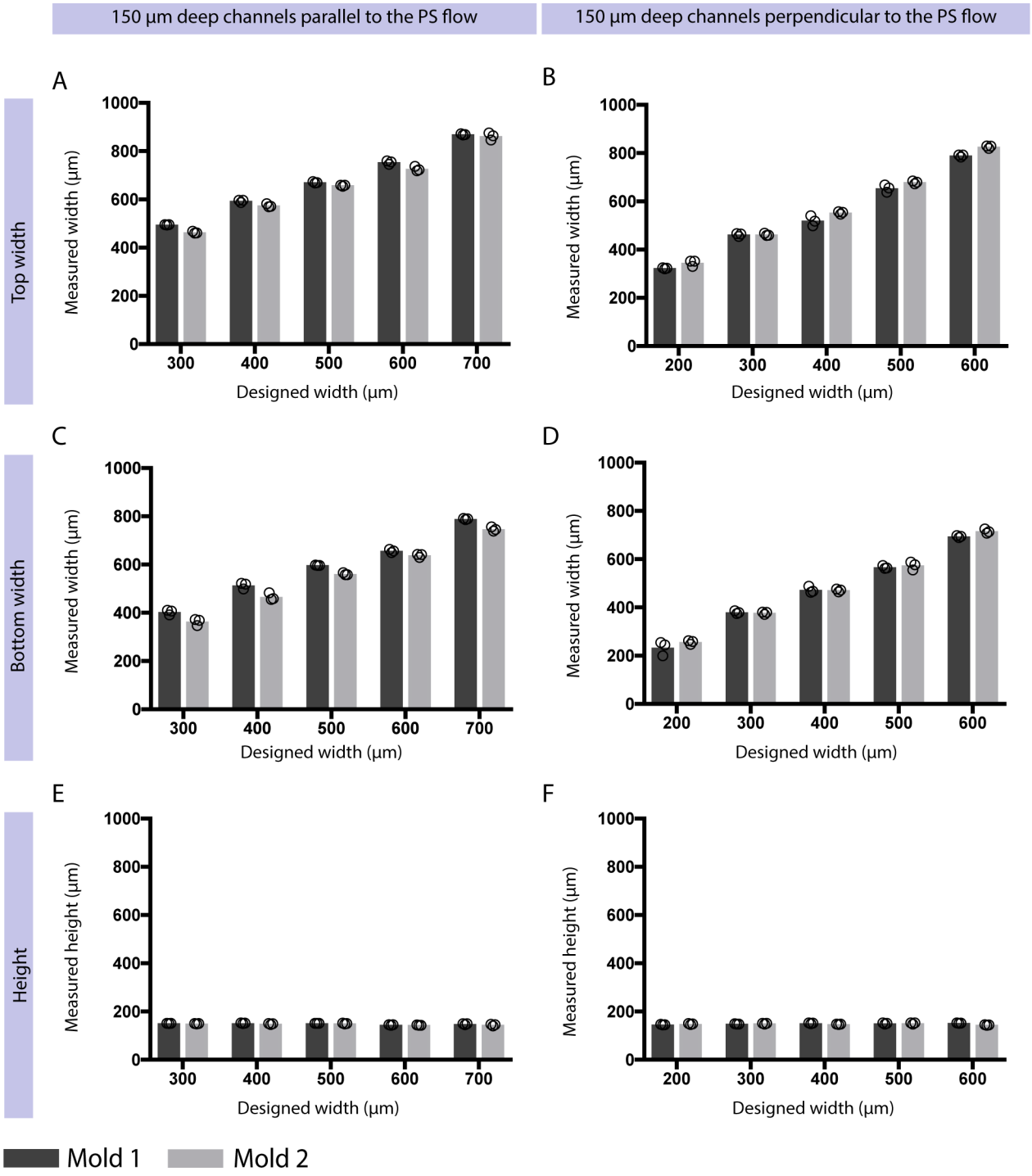

Figure A5. Quantification of channel dimensions from devices injection molded out of two identically designed molds. Graphs of mold 1 and mold 2 for 150 µm deep rectangular channels parallel (left) and perpendicular (right) to molten PS flow. Data points (open circles plotted on top of bar graphs) indicate three devices measured (all from the same metal mold); bars indicate the mean.

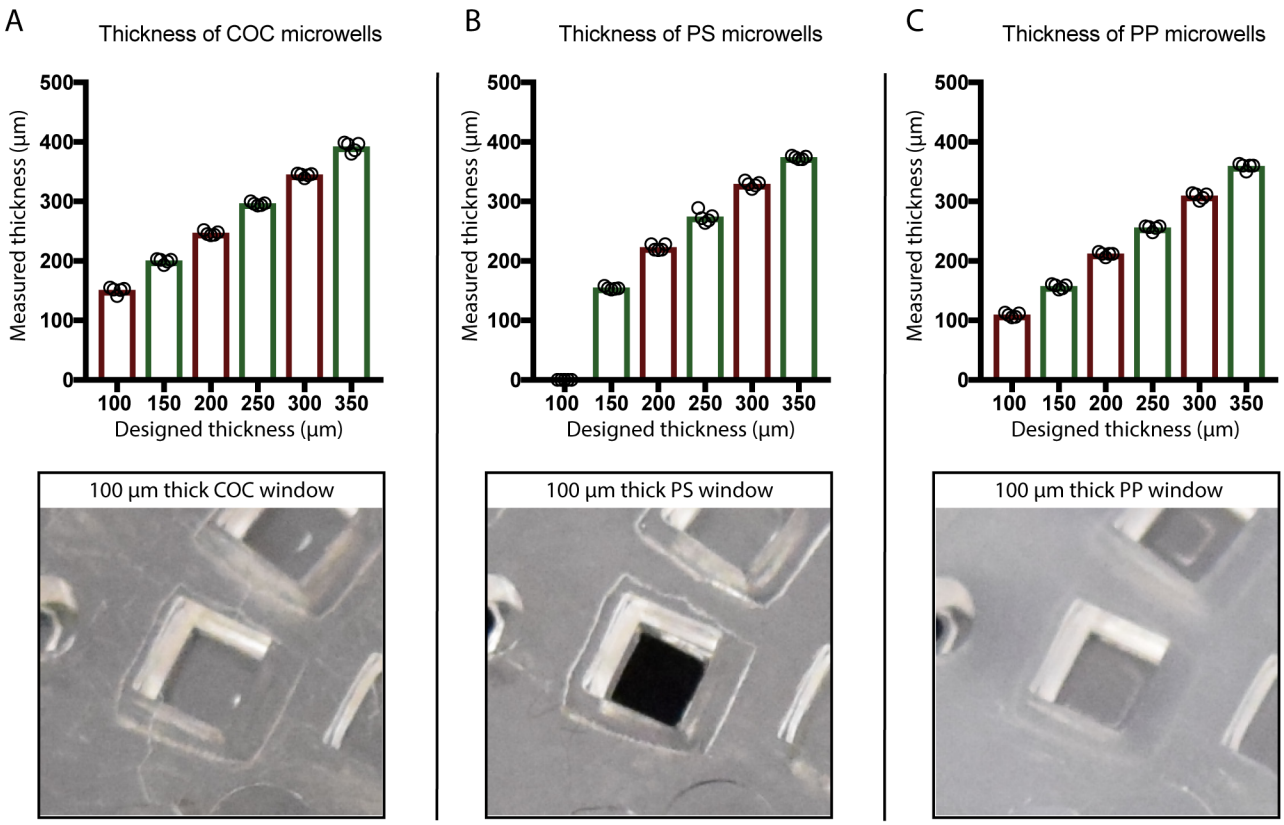

Figure A6. Measured microwell thicknesses (top) and photo of 100 µm thick microwell (below) for (A) COC (B) PS (C) PP. Red bars indicate SPI_A2 polishing level, and green indicates SPI_B1 polishing level. Data points (open circles plotted on top of bar graphs) indicate five devices measured (all from the same metal mold); bars indicate the mean.

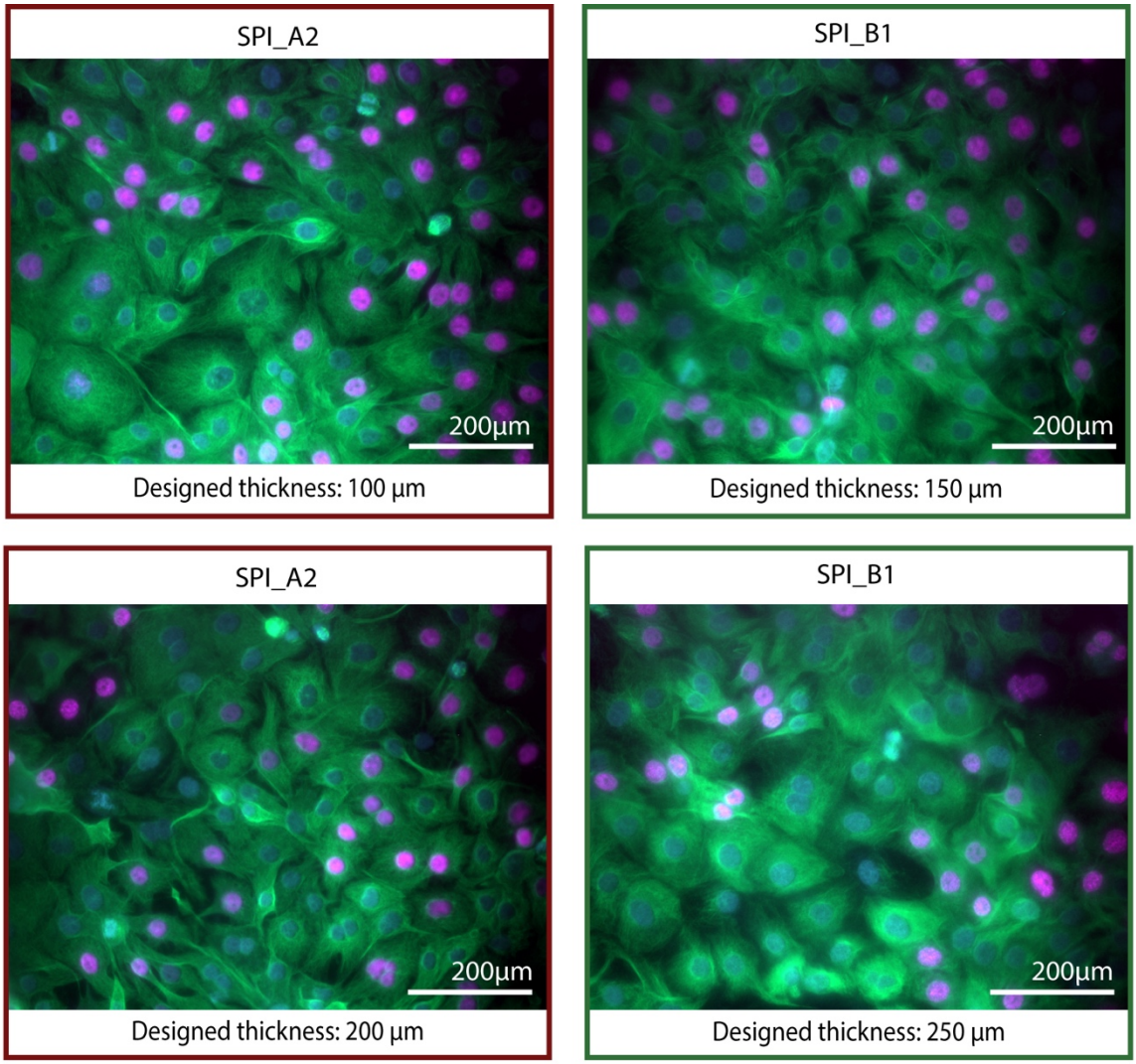

Figure A7. Unmodified fluorescence images of BHPrE1 cells in COC microwells of varying thickness and surface roughness. Images taken at 20x (0,40 NA) magnification with nuclear staining (DAPI, blue), proliferating nuclei (EdU, red), and tubulin (green). Red borders indicate SPI_A2 as highest level of polishing provided by Proto Labs® (left) and green indicates SPI_B1 as second highest level of polishing (right).

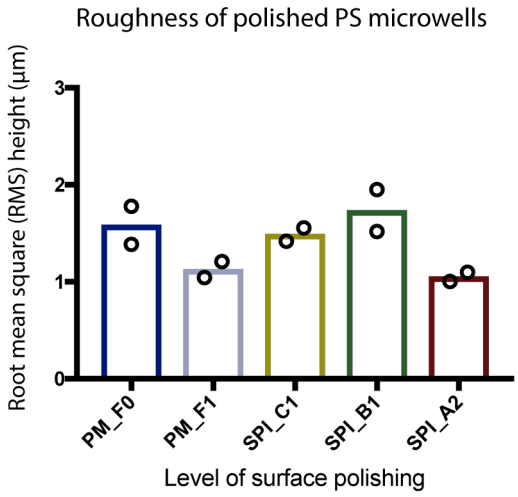

Figure A8. Root mean square height for PS microwells. Points represent measurements from two microwells of the same polishing in one device.

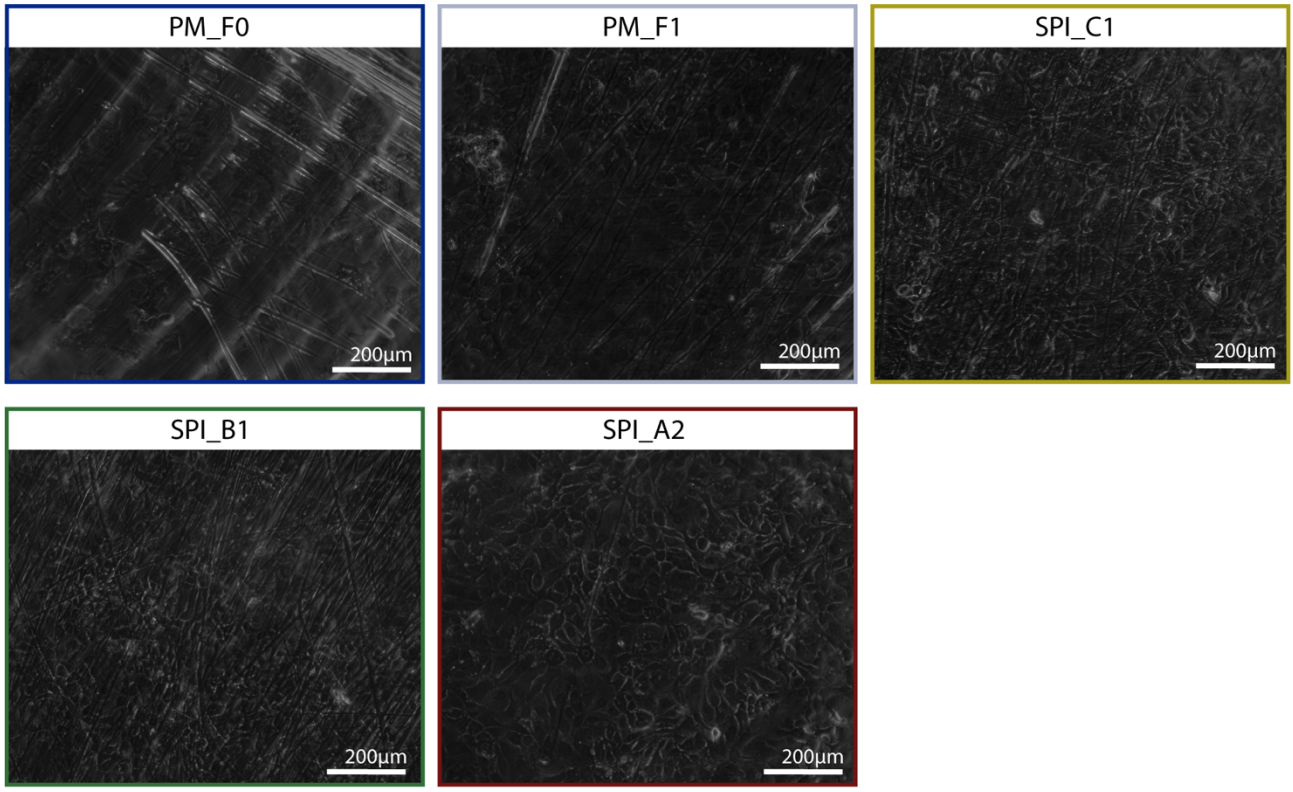

Figure A9. Unmodified phase contrast images of BHPrE1 cells on COC microwells of varying surface roughness taken at 10x magnification. Images are representative of two replicate microwells from one device.

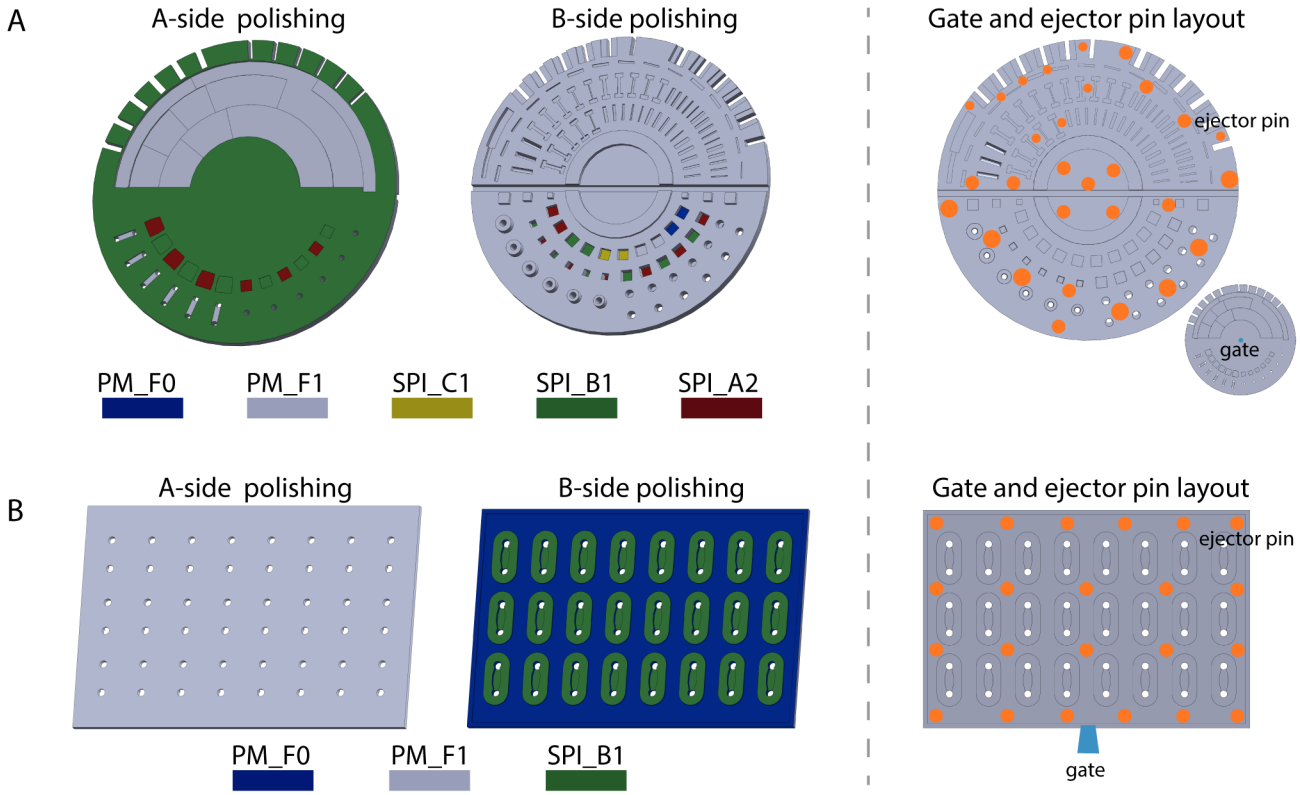

Figure A10. Polishing levels applied to both sides of the mold for all devices. Ejector pin and gate layout on molds. (A) test device and (B) closed cell culture channels. Five levels of polishing offered by Proto Labs®: PM-F0: Non-cosmetic, finish to Proto Labs® discretion; PM-F1: Low-cosmetic, most toolmarks removed; SPI-C1: 600 grit stone; SPI-B1: 600 grit paper; SPI-A2: Grade #2 diamond buff.

Considerations when working with and choosing rapid injection molding companies

The following is a list of questions and considerations that may be useful to ask when choosing a rapid injection molding company.

Questions to consider when calculating price comparisons

1. The metal mold used to manufacture plastic parts is typically retained by the rapid injection molding company. Companies typically will not release the mold to customers because it contains aspects of their proprietary process technology (such as the way the mold configures with their injection molding system to enable rapid work flows). Molds are typically stored indefinitely or for an agreed upon period of time, and the customer can request additional parts at a later date. Some questions to ask include:

a) How long are the metal molds stored? Is there a fee for storing the mold (some, but not all, companies charge a storage fee)?

b) What is the 'setup fee' for making a new batch of devices? (Some, but not all, companies charge a fee to take the mold from storage and set it up for subsequent batches of devices.)

2. Is there a 'material change fee' if parts in different materials are desired from the same mold? Typically the material change fee is less than the 'setup fee' discussed in 1 b. (For example, it may cost $500 to setup a new batch of devices and $100 to change materials within a batch, so if parts are desired in PS, COC and PP it may be advantageous to combine all three materials in a single order to avoid multiple 'setup fees'. However, some companies may not charge a fee for either setup or material changes.) Note: switching materials may result in different dimensions and tolerance, since plastics have different properties (e.g., shrink rates, flow properties, melting temperatures).

3. How many parts can be produced from the mold? The metal mold wears over time, and different companies guarantee the mold for different numbers of parts (Proto Labs: ~10,000 parts in an aluminum mold).

Additional technical questions

1. What metal are the molds made of? Aluminum is typically used for rapid injection molding, but some companies may use soft steels that provide results more typical of production scale injection molding.

2. Are the parts inspected for accuracy by the manufacturer? If so, how are the parts inspected?

3. Is the shrinking of the part accounted for in the design of the mold? Is the mold specifically designed for a certain material with a determined shrink rate?

4. Can the designer choose the tolerances? What are the highest tolerances achievable? (Proto Labs has a predetermined tolerance for most uploaded parts and thus tolerances cannot be specifically chosen.)

B. Appendix for Chapter 3

Reproduced in part from J. W. Khor, U. N. Lee,* J. Berthier, E. Berthier,[#] A. B. Theberge,[#] "Interfacial tension driven open droplet microfluidics." bioRxiv, https://doi.org/10.1101/2021.07.29.454194.*
** Equal contribution*
[#]Co-corresponding authors

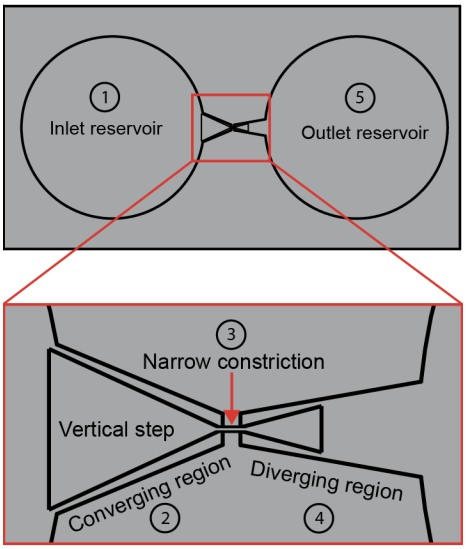

Figure B1. Main regions of the device. (1) Inlet reservoir which leads to the (2) converging region, followed by the (3) narrow constriction, (4) diverging region, and (5) outlet reservoir.

Note 1: Theoretical derivation of condition for aqueous plug extrusion or droplet generation in our channel

In this section, a theoretical model is derived to determine the condition required for aqueous plug extrusion or droplet generation in our channel. Let us consider the schematization of Figure B2 where an aqueous plug is placed in a constriction and both sides of the plug are filled with an immiscible carrier fluid. The converging region holds the aqueous plug where the anterior end of the plug meets the narrow constriction. The pressure on the anterior and posterior sides of the plug are different. The model is based on the fact that the pressure difference between the posterior and anterior interfaces of the plug causes the plug extrusion or droplet generation. This pressure difference is due to the hydrostatic pressure exerted by the carrier in the reservoir on the aqueous plug. In our system, the interfacial tension between carrier fluid and aqueous plug (HFE7500/deionized water) is very low. Therefore, the carrier fluid (HFE7500) does not flow over the aqueous plug. This configuration is called shift mode as defined in Lee *et al.*[1] Furthermore, because the aqueous plug does not wet the PTFE channel walls, there is a small leakage of carrier fluid along the inner corners of the converging region.[2] It is assumed that this leakage of carrier fluid imposes the same interfacial tension on both corners (left and right) of the aqueous plug. Finally, a simplifying assumption has been made: The vertical curvature radii on both sides of the plug cancel out.

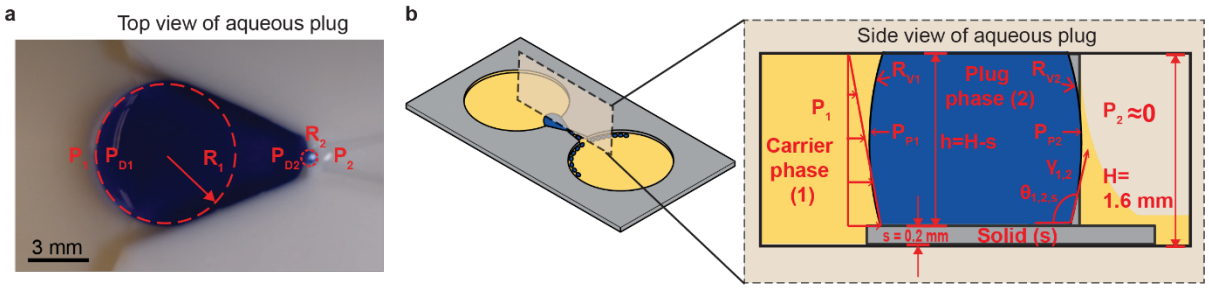

Figure B2. (A) Top and (B) side view of aqueous plug placed in the converging region prior to aqueous plug extrusion.

Let us write the Laplace pressure for each end of the aqueous plug[2-4]

For the posterior interface,

$$P_{P1} - P_1 = \gamma \left(\frac{1}{R_1} + \frac{1}{R_{v1}}\right) \quad (1)$$

Similarly for the anterior interface,

$$P_{P2} - P_2 = \gamma \left(\frac{1}{R_2} + \frac{1}{R_{v2}}\right) \quad (2)$$

Where P_{Pi} is the local pressure in the aqueous plug at the interface, P_i is the carrier fluid pressure at the external aqueous plug interface, γ is the interfacial tension between carrier fluid and aqueous plug, R_i is the curvature radius in the horizontal plane (Figure B2a), and R_{vi} is the curvature radius in the vertical plane (Figure B2b). When the subscript of parameters, $i = 1$, it denotes that the parameter is referring to parameters at the posterior side of the aqueous plug and when $i = 2$, it denotes that the parameter is referring to parameters at the anterior side of the aqueous plug.

Subtracting Eq. (2) from Eq. (1) yields

$$P_{P1} - P_{P2} = (P_1 - P_2) + \gamma \left(\frac{1}{R_1} - \frac{1}{R_2} + \frac{1}{R_{v1}} - \frac{1}{R_{v2}}\right) \quad (3)$$

We make the assumption that $R_{v1} \approx R_{v2}$because the channel height is uniform throughout the channel and we are left with

$$P_{P1} - P_{P2} \cong (P_1 - P_2) + \gamma \left(\frac{1}{R_1} - \frac{1}{R_2}\right) \quad (4)$$

The pressure in the inlet reservoir P_1 (see Figure B2a) is the hydrostatic pressure ($P_1 = \rho g h$) and that in the outlet, nearly empty reservoir is determined to be $P_2 \approx 0$. Then relation (4) becomes

$$P_{P1} - P_{P2} \cong \rho g h + \gamma \left(\frac{1}{R_1} - \frac{1}{R_2}\right) \quad (5)$$

where ρ is the density of the carrier fluid, g is the gravitational acceleration, and h is the carrier fluid height (note that for our device, aqueous plug height is also equal to carrier fluid height).

The condition for the aqueous plug to advance into the constriction is $P_{P1} > P_{P2}$, or

$$\rho g h + \gamma \left(\frac{1}{R_1} - \frac{1}{R_2}\right) > 0 \quad (6)$$

At the beginning of the plug advancement (depicted in Figure 2), the curvature radius R_1 is very large when compared to curvature radius R_2 ($R_1 \gg R_2$). This means $1/R_1$ can be neglected when subtracted by $1/R_2$ ($1/R_1 \ll 1/R_2$ *so* $1/R_1 - 1/R_2 \approx -1/R_2$).

Then the condition for plug extrusion or droplet generation is

$$\rho g h > \frac{\gamma}{R_2} \quad (7)$$

When the anterior section of the aqueous plug interface advances through the constriction (see **Figure B2a**), the initial curvature radius R_2 is approximately[2]

$$R_2 \approx \frac{w}{2|cos\theta|} \quad (8)$$

where w is the constriction width and θ is the contact angle between channel wall, aqueous plug, and carrier fluid.

The condition for plug extrusion or droplet generation is then

$$\rho g h > \frac{2\gamma\,|cos\theta|}{w} \quad (9)$$

Relation Eq. (9) shows that the constriction width *w* must not be too small when designing the device ($w > \frac{2\gamma\,|cos\theta|}{\rho g h}$).

References

1. Lee, J. J. *et al.* Droplet Behavior in Open Biphasic Microfluidics. *Langmuir* **34**, 5358-5366, doi:10.1021/acs.langmuir.8b00380 (2018).
2. Berthier, J. & Brakke, K. A. *The Physics of Microdroplets*. (Wiley, 2012).
3. Berthier, J., Brakke, K. A. & Berthier, E. *Open Microfluidics*. (Wiley, 2016).

4. de Gennes, P.-G., Wyart-Brochard, F. & Quere, D. *Capillarity and Wetting Phenomena.* (Springer, 2004).

Note 2: Use of units when computing $\frac{2\gamma\,|cos\theta|}{\rho g h}$ in Figure 3

When calculating $\frac{2\gamma\,|cos\theta|}{\rho g h}$, we use SI units for all parameters during calculation; thus, the final value will be the SI unit for length, meters. In Figure 3 since we used millimeters on the x-axis, we convert $\frac{2\gamma\,|cos\theta|}{\rho g h}$ to millimeters (1 mm = 0.001 m).

Here, we show the rearrangement and simplification of the units of $w > \frac{2\gamma\,|cos\theta|}{\rho g h}$ and show that the final unit is meter.

The unit of γ is of N/m, θ is unitless, ρ is kg/m^3, g is m/s^2, and h is m. Unit of N is kg*m/s^2

$\frac{2\gamma\,|cos\theta|}{\rho g h}$ would then have units:

$$\frac{\frac{N}{m}}{\left(\frac{kg}{m^3}\right)*\left(\frac{m}{s^2}\right)*(m)} = \frac{N*m^3*s^2}{kg*m^3} = \frac{N*s^2}{kg} = \frac{kg*m*s^2}{kg*s^2} = m$$

From there, convert meters to millimeters to obtain the same unit as Figure 3a.

Note 3: Table of parameters

Table B1. Table of parameters of Figure 3a regime map.

Constriction width (mm)	Interfacial tension (mN/m)	Density (kg/m^3)	Carrier fluid height (mm)	Contact angle (degree)	Plug Extrusion (Yes/No)	Droplet generation (Yes/No)
0.20	3.9	1614	1.4	125.2	Yes	Yes
0.40	3.9	1614	1.4	125.2	Yes	Yes
0.60	3.9	1614	1.4	125.2	Yes	Yes
3.00	3.9	1614	1.4	125.2	Yes	No
1.00	3.9	1614	1.4	125.2	Yes	No
2.00	3.9	1614	1.4	125.2	Yes	No
0.20	10.3	1614	1.4	132.4	No	Yes
0.40	10.3	1614	1.4	132.4	Yes	Yes
0.60	10.3	1614	1.4	132.4	Yes	Yes
3.00	10.3	1614	1.4	132.4	Yes	No
0.25	14.8	1614	1.4	135.2	No	No
0.40	14.8	1614	1.4	135.2	No	No
1.00	14.8	1614	1.4	135.2	No	No
2.00	14.8	1614	1.4	135.2	Yes	No
3.00	14.8	1614	1.4	135.2	Yes	No
1.00	35.0	1614	1.4	140.1	No	No
2.00	35.0	1614	1.4	140.1	No	No
3.00	35.0	1614	1.4	140.1	No	No
0.25	35.0	1614	1.4	140.1	No	No
0.40	35.0	1614	1.4	140.1	No	No
0.20	47.9	1614	1.4	147.2	No	No
0.40	47.9	1614	1.4	147.2	No	No
0.60	47.9	1614	1.4	147.2	No	No
3.00	47.9	1614	1.4	147.2	No	No
1.00	47.9	1614	1.4	147.2	No	No
2.00	47.9	1614	1.4	147.2	No	No

Table B2. Table of parameters of Figure 4 generated droplet volume

Constriction width (mm)	Density (kg/m^3)	Carrier fluid height (mm)	Interfacial tension (mN/m)	Contact angle (degree)	Generated droplet volume (μL)	
					Average	Standard deviation
0.20	1614	1.4	3.9	125.2	0.52	0.025
0.40	1614	1.4	3.9	125.2	2.49	0.175
0.60	1614	1.4	3.9	125.2	7.75	0.465
1.00	1614	1.4	3.9	125.2	19.22	1.344
0.40	1614	1.4	10.3	132.4	7.23	0.504
0.60	1614	1.4	10.3	132.4	15.09	0.906
1.00	1614	1.4	10.3	132.4	34.55	2.422

Supplementary Note 4: Engineering drawing of open microfluidic channels

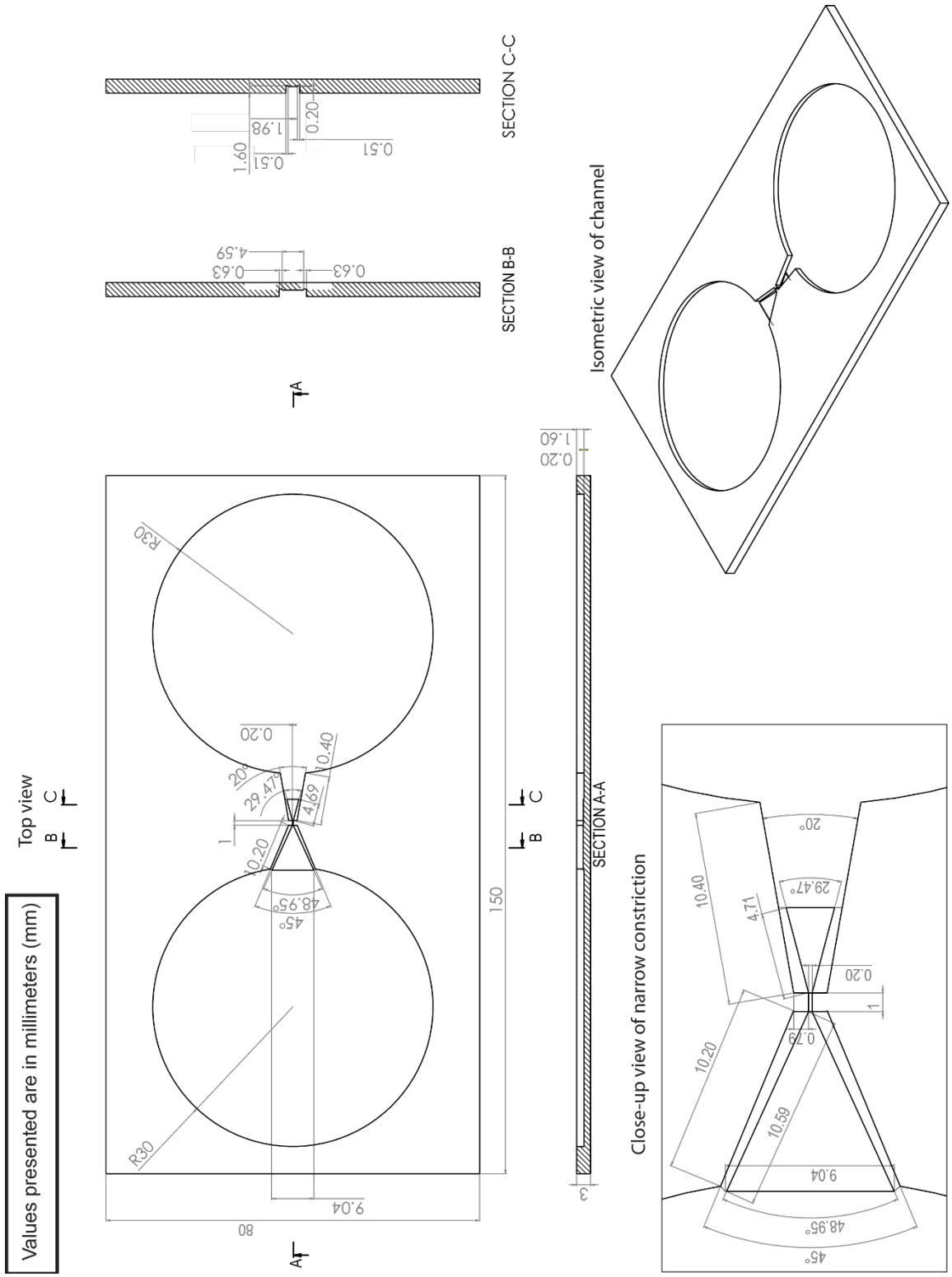

Figure B3. Engineering drawing of droplet generation channel.

Values presented are in millimeters (mm)

Detailed measurements of converging-diverging region and constriction can be found in Supplementary figure S3

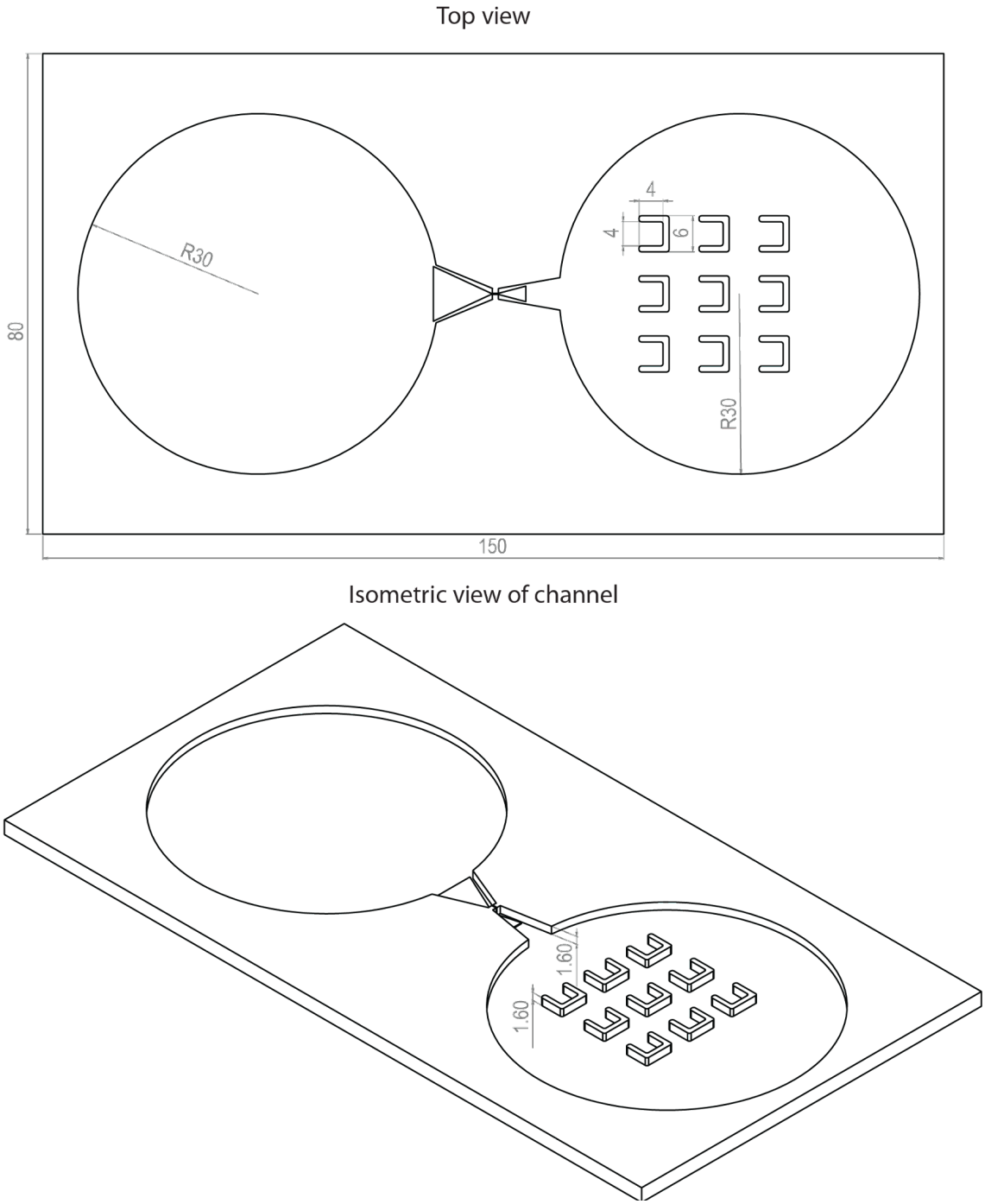

Figure B4. Engineering drawing of sorting channel.

Values presented are in millimeters (mm)

Detailed measurements of converging-diverging region and constriction can be found in Supplementary figure S3

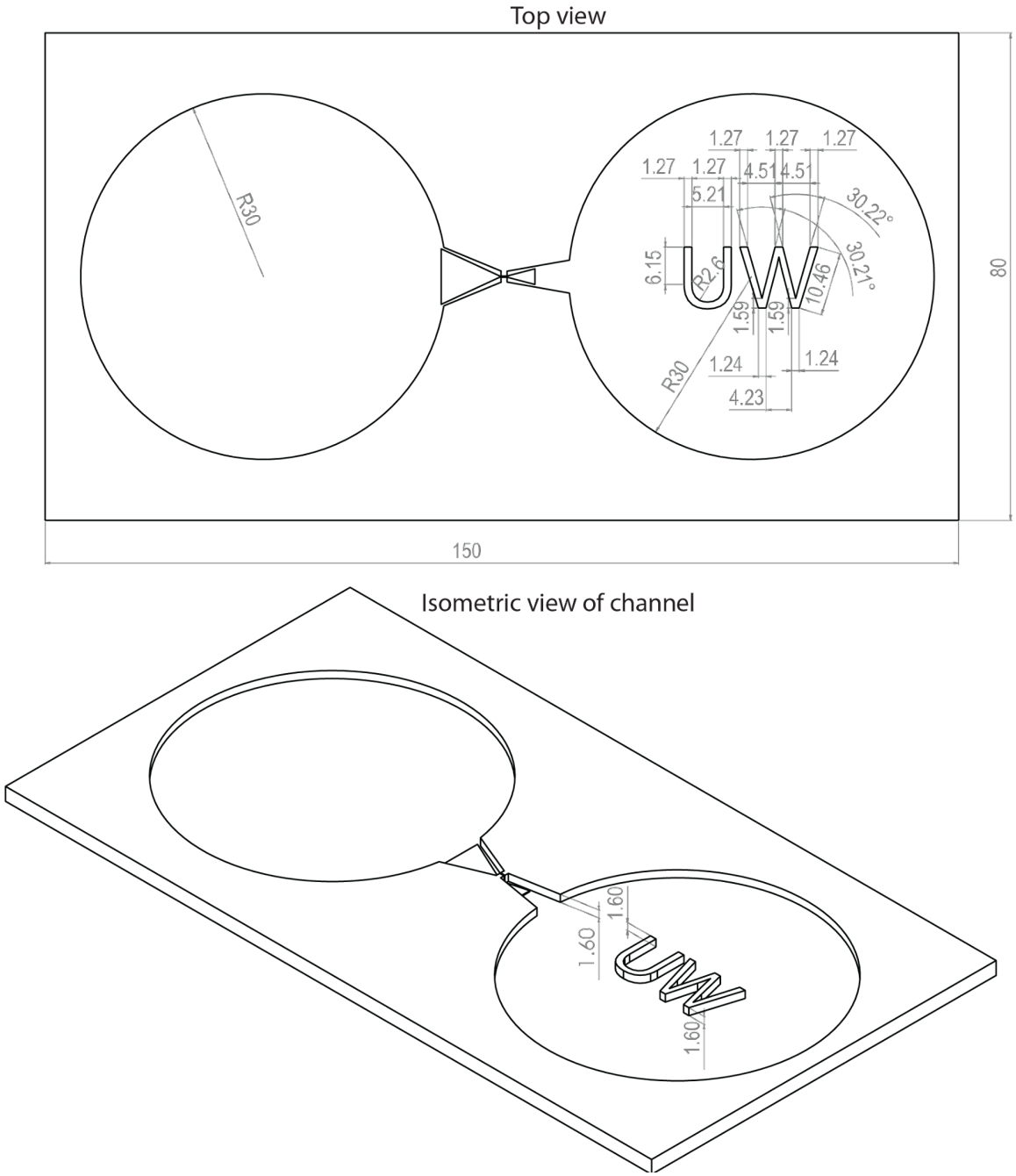

Figure B5. Engineering drawing of UW channel.

Values presented are in millimeters (mm)

Detailed measurements of converging-diverging region and constriction can be found in Supplementary figure S3

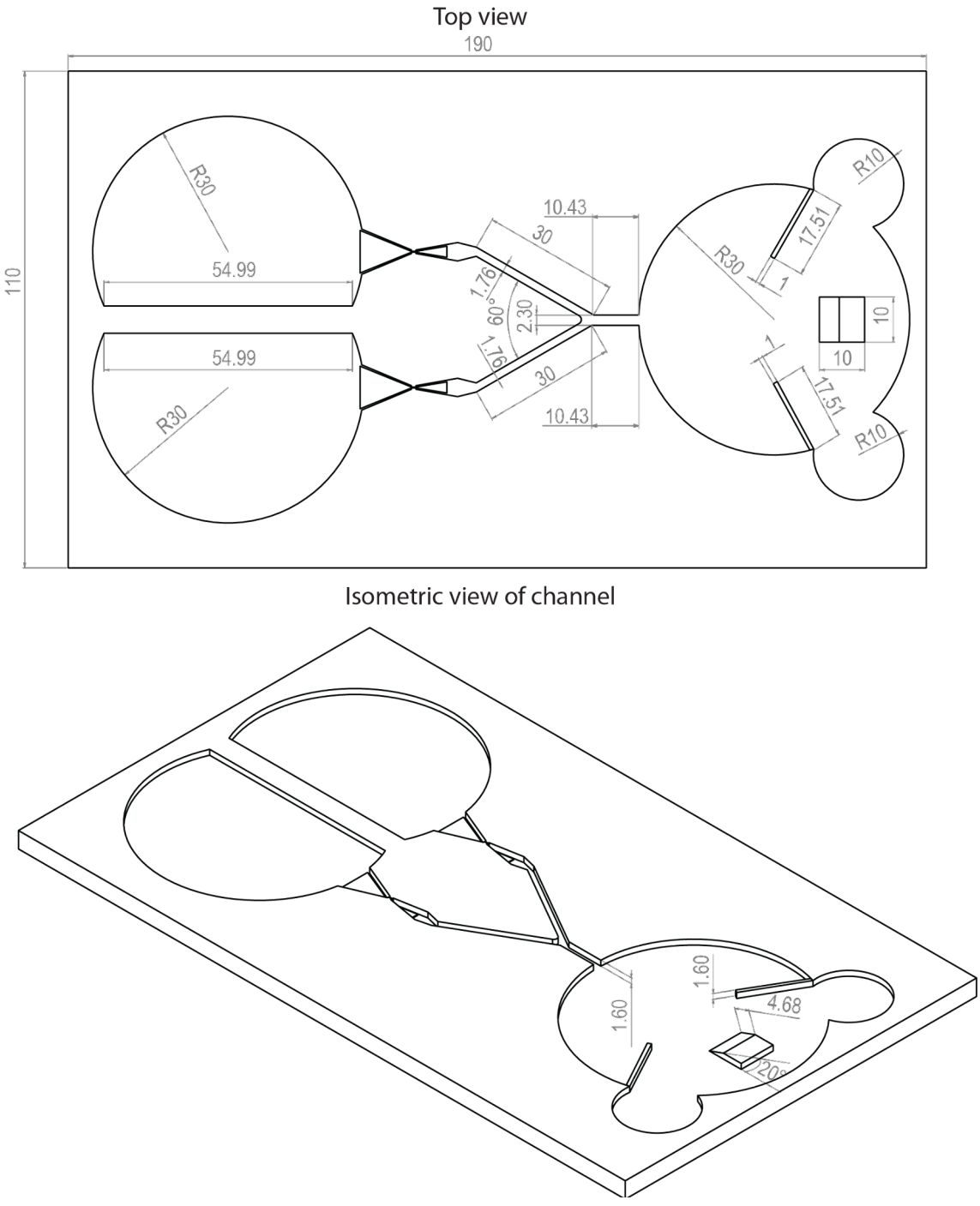

Figure B6. Engineering drawing of fusion channel.

Supplementary Note 5: Accuracy of Matlab code during computation of droplet volume.

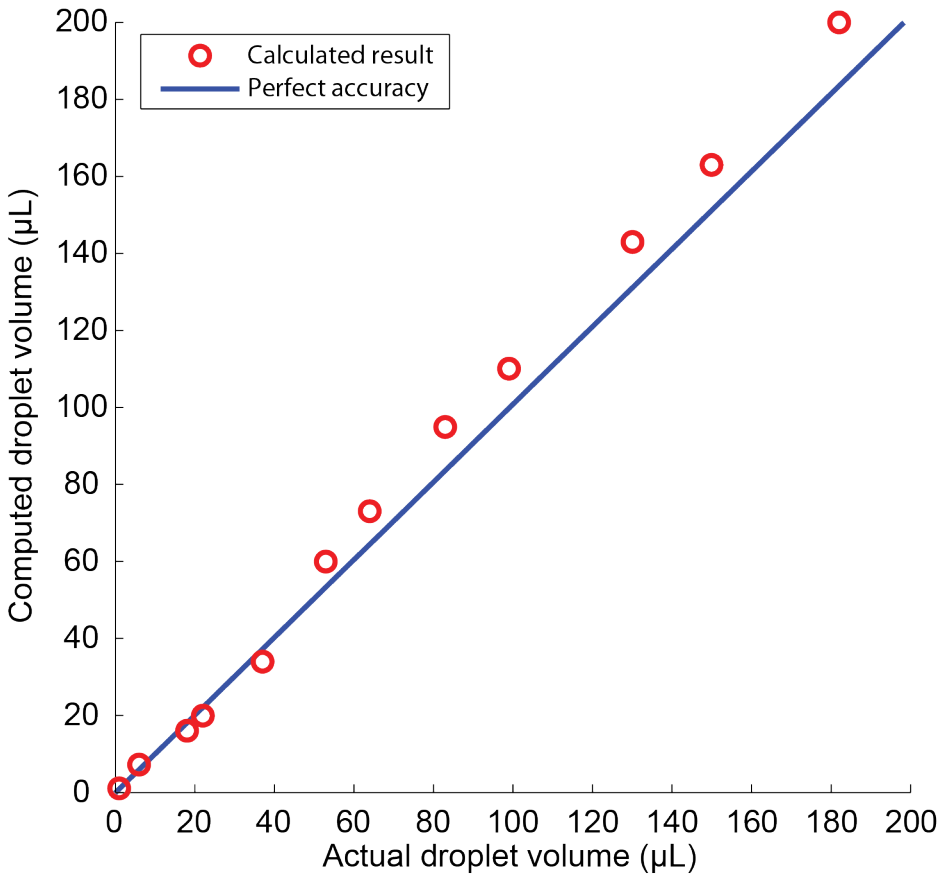

Figure B7. Plot that shows the accuracy of the custom Matlab code in determining droplet volume when compared to actual droplet volume. Red circles represent droplet volume computed by Matlab code and blue solid line represents the curve when the Matlab code would achieve a perfect accuracy (100%). When compared to the "perfect accuracy" reference curve, the data points has coefficient of determination, $R^2 = 0.9799$.

C. Appendix for Chapter 4

Reproduced in part from U. N. Lee, J. H. Day,* A. J. Haack,* R. C. Bretherton, W. Lu, C. A. DeForest,[#] A. B. Theberge,[#] and E. Berthier,[#] "Layer-by-layer fabrication of 3D hydrogel structures using open microfluidics." Lab on a Chip, 2020, **20**, 525–536.*
**Equal contribution*
[#]Co-corresponding authors

Extended Materials and Methods

Derivation for SCF condition in rail-based microchannels
In the case where a channel is comprised of multiple surfaces with different materials and unique contact angles, the condition for advancement of a fluid in the channel is given by a condition on the Cassie Angle, θ^*(1a), referred to as the Generalized Cassie law (1b), where f_i is the fraction of the channel's cross-sectional perimeter composed of a material i, and θ_i is the contact angle of material i.

$$\cos(\theta^*) = \sum_i f_i \cos(\theta_i) \quad \text{(Eq. 1a)}$$

$$\cos(\theta^*) > 0 \quad \text{(Eq. 1b)}$$

Given the cross-sectional geometry of a rail-based channel and the convention that the contact angle of fluid on air is 90°, Eq. 1 can be rewritten as:

(Eq. 2)

Where w_1 is the width of the channel ceiling, w_2 is the width of the channel floor, and h is the distance between the channel ceiling and the floor. Assuming that $w_1 = w_2$, Eq. 2 reduces down to:

$$\frac{h}{w_1} < \frac{\cos(\theta_1) + \cos(\theta_2)}{2} \quad \text{(Eq. 3)}$$

where h is the height of the patterned layer (defined by the distance between the patterning area of the patterning device and the underlying substrate), θ_1 is the contact angle of the patterning device, and θ_2 is the contact angle of the underlying substrate.

Design of hollow double helix
The helix consists of a total of 30 layers of agarose (including the base layer), which were all patterned via SCF and rail-based technology. Each layer looks like a button with two holes, that is rotated about the center for each subsequent layer. Figure C3A illustrates a top-down schematic for the helix design. The length, d, is the diameter of the holes, which is 3 mm for all layers on both sides. r is the distance from the center of the design to the center of the holes on both sides, and for all layers is 2.5 mm. The angle of rotation about the center of the design is denoted by ϕ, and the maximum overhang length is denoted by s. For the first two layers, the angle of rotation, ϕ, is 5° with a designed overhang, s, of 240 μm to establish the overhang. After the overhang was established, the remaining layers were rotated 10° for a total designed maximum overhang of 479 μm. A new device was used for each layer with an alignment marker for consistency in the degree of rotation. The helix was designed to include a curvature that outlined the two

holes which allowed for SCF to continue to the edge of the desired overhang. These values can be found in Table C1.

Imaging of hollow double helix

A Nikon DSLR camera was used to take images of the double helix. The helices were removed from the well plate with a spatula and placed on a standard No. 1.5, 25 mm square coverslip (Fisherbrand). A 1 mL syringe with a 18 gauge needle with 18 gauge PTFE tubing attached to reach the bottom of the helices was used to load the helices with dye. A syringe with a 25 gauge needle was used to remove any air pockets that formed from filling the hollow tubes with dye. During loading, the tubing damaged the walls of the agarose and these irregularities filled with dye (Figure 4C, right). Yellow and blue India ink dye (Dr. Ph. Martin's Bombay India Ink) was used to fill the helix (Figure 4C, right), and dextran with fluorescein 70,000 MW in DI water at 10 mg/mL (Invitrogen) was used to fill a separate helix in Figure 2C. To take the photo in Figure 2C, the fluorescent dye was excited using a 365 nm lamp (Spectroline). Helix images were processed using Adobe Photoshop CC 2018 using a uniform brightness/contrasts adjustment.

Imaging and design of overhanging cross sections

The cross-sectional images shown in Figure 4A were designed such that the overhang and curvature of each layer corresponded to the maximum overhang in the first seven layers of the helix. The curvature information can be found in Table C1 where the first seven layers correspond to the overhang cross section device, as well as the first seven layers of the helix. To image the cross section, a smooth edge was cut using a coverslip (Fisherbrand) and the overhang was transferred to another coverslip for imaging with a DSA25E goniometer (Kruss). The images in Figure 4A are separately constructed agarose structures, cut and imaged at different stages.

Design of curvature for overhanging features

In order to achieve spontaneous capillary flow for all layers of the seven layered overhanging structure (Figure 4A) and the hollow double helix structure (Figure 4C, Figure 2C), the geometry of curvature was adjusted for each layer. If each layer had the same curvature, then the maximum distance (air gap) between the two layers would become great enough that spontaneous capillary flow is inhibited. This concept is illustrated in Figure C3C, as denoted by the red arrow. However, by applying a calculation to change the curvature dimensions of the current layer based upon the dimensions of the previous layer, the distance between layers can be minimized allowing for SCF, illustrated by the reduction of the double-headed red arrow length (Figure C3C). Note that the overhang dimensions for the seven layered overhanging structure in Figure 4A are the same as the dimensions for the first seven layers of the helix. The calculation was made as follows: for the first overhanging layer, layer 2, the radius of curvature is set to 1 mm. Every subsequent layer's radius of curvature is increased by 0.5 mm, i.e., layer 3 is 1.5 mm, layer 4 is 2 mm, etc. Take any layer, n where $n > 1$, and the radius of curvature, r_n is then given by Eq. 4.

$$r_n = 0.5n \qquad \text{(Eq. 4)}$$

Layer 1 has no radius of curvature, as it is not an overhanging layer. The curvature of layer n was designed such that the curvature began at half the distance of the x-component of the previous layer, x_{n-1}, which is illustrated in the diagram below.

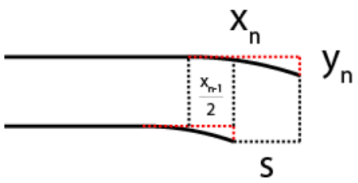

Note that s is the designed maximum overhang, which for the helix design is also denoted by s in Figure C3A. The s component of the curvature for layer n, x_n, is then given by taking one half of the x-component of the previous layer, and adding this to the maximum overhang, s, described in Eq. 5.

$$x_n = \frac{x_{n-1}}{2} + s \quad \text{(Eq. 5)}$$

Note that the maximum overhang, s is set by the angle of rotation for the helix (ϕ in Figure C10A). Using the calculated x-component and the radius of curvature for layer n, the y-component of the curvature can then be derived. The schematic below shows the geometrical schematic to calculate these layers.

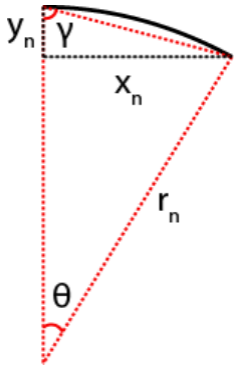

To calculate the angle, θ, which represents the arc angle of the circle that encompasses the curvature, the geometric relation of the radius of curvature, r_n, to the x-component of the curvature was used, and described in Eq. 6 where θ is in degrees.

$$\theta = \arcsin\left(\frac{x_n}{r_n}\right) \quad \text{(Eq. 6)}$$

Using this angle and the fact that the red dotted triangle is an isosceles triangle, the value of angle γ could be calculated using Eq. 7, where γ and θ are in degrees.

$$\gamma = \frac{180 - \theta}{2} \quad \text{(Eq. 7)}$$

Then, the value of y_n can be calculated using Eq. 8.

$$y_n = \frac{x_n}{\tan(\gamma)} \quad \text{(Eq. 8)}$$

These calculations were applied to all layers to derive the values in Table C1. Note that the first overhanging layer, layer 2, was set such that the curvature began at the edge of layer 1.

Enzymatically degradable hydrogels synthetic information

Chemical reagents were obtained from either Sigma-Aldrich or Fisher Scientific unless otherwise noted. Amino acids for peptide synthesis were purchased from ChemPep and associated coupling reagents from Chem-Impex.

Peptides were synthesized using standard Fmoc Solid Phase Peptide Synthesis (SPPS) on a microwave-assisted Liberty1 automated peptide synthesizer. Fmoc groups were deprotected in 20% piperidine (v/v) in N,N dimethylformamide (DMF) with 0.1 M 1-hydroxybenzotriazole (HOBt) at 90°C for 90 seconds. Fmoc-protected amino acids (1 mmol; 4x) were coupled in a solution of 1-[Bis(dimethylamino)methylene]-1H-1,2,3-triazolo[4,5-b]pyridinium 3-oxide hexafluorophosphate (HATU; 1 mmol; 4x) and diisopropylethylamine (DIEA; 2 mmol; 8x) in a mixture of 20% N-methyl-2-pyrrolidone (NMP) in DMF at 75°C for 5 minutes.

Semi-preparative scale reversed-phase high-pressure liquid chromatography (RP-HPLC) was conducted on a Dionex Ultimate 3000 with 220 nm and 280 nm detection wavelengths, through a Thermo 5 μm Sychronis silica 250x21.2 mm C18 column. Pure fractions were lyophilized using a LABCONCO FreeZone 2.5 plus freeze-dryer equipped with a LABCONCO rotary vane 117 vacuum pump. Matrix-assisted laser desorption/ionization time of flight (MALDI-TOF) mass spectrometry was performed on samples suspended in a matrix of α-cyano-4- hydroxycinnamic acid:2,5-dihydroxy benzoic acid (2:1) using a Bruker AutoFlex II mass spectrometer in reflectron positive mode with detector range set to 600-3000 Da.

Four-arm poly(ethylene glycol) (MW = 20,000 Da) end-functionalized with bicyclononyne (PEG-tetraBCN) and N_3-GRGDS-NH_2 peptide were synthesized as previously described [1,2].

Recombinant Expression and Purification of SrtA(5M)

pET30b-5M SrtA was a gift from Hidde Ploegh (Addgene plasmid # 51140 ; http://n2t.net/addgene:51140 ; RRID:Addgene_51140). Chemically competent BL21 *E. coli* cells were transformed with the pET30b-5M SrtA plasmid, expanded in 1 L of Luria broth at 37°C under agitation at 200 RPM, and induced using 0.5 mM Isopropyl-beta-D-thiogalactoside when OD600 of the bacterial culture reached 0.6, measured on a Thermo Fisher Nanodrop 2000 spectrophotometer. After overnight culture at 17°C and 200 RPM agitation, cells were pelleted, resuspended in lysis buffer (20 mM Tris; 50 mM NaCl; 10 mM imidazole; 40 mL) on ice, and lysed by sonication (6 x 3 min cycles; 30% amplitude, 33% duty cycle and 3 min resting). The soluble lysate fraction was incubated with 3 mL Ni-NTA Agarose Beads (GoldBio) for 1hr at 4°C in a gravity column. The resin and bound His-tagged protein were washed in wash buffer (20 mM Tris; 50 mM NaCl; 20 mM imidazole; 5 x 20 mL), then purified SrtA was eluted in elution buffer (20 mM Tris; 50 mM NaCl; 20 mM imidazole; 20 x 1 mL). Protein was then dialyzed against PBS with Thermo Fisher SnakeSkin Dialysis Tubing (MWCO ~10 kDa) to remove Tris and imidazole. Protein was then spin concentrated in an Amicon centrifugal column (MWCO ~10 kDa), glycerol was added to 20% wt/vol, and aliquots were stored at -80°C prior to use. Protein identity and purity were confirmed using SDS-PAGE and whole protein ESI-MS (Expected 17.8 kDa, Observed 17.8 kDa).

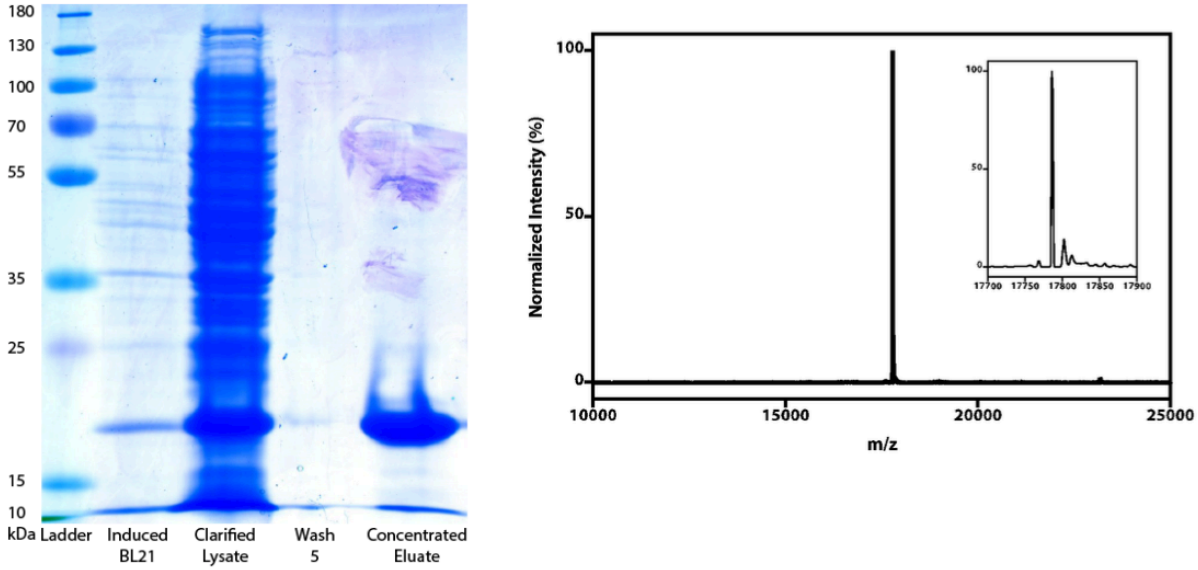

SrtA(5M) protein purification was evaluated by SDS-PAGE, revealing a strong 18 kDa band corresponding to the protein (left). Protein Identity was verified by mass spectrometry (right).

Synthesis of N_3-RGPQGIWGQGRK(N_3)-NH_2 and N_3-RGPQGIWGQLPETGGRK(N_3)-NH_2

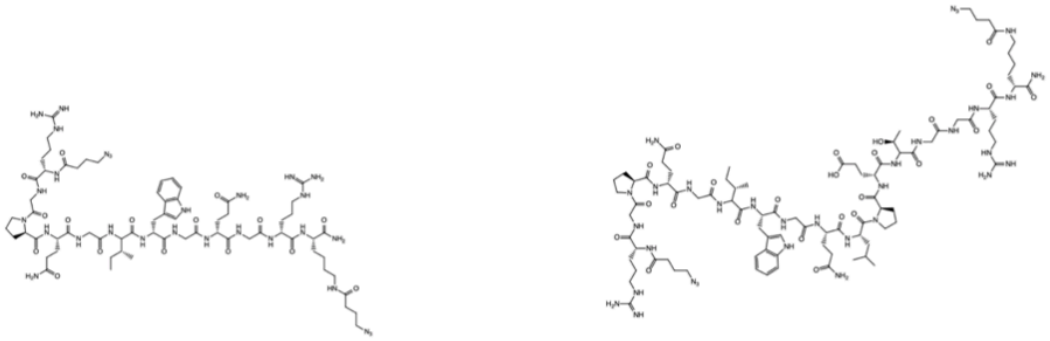

Chemical structures of the MMP-degradable peptide N_3-RGPQGIWGQGRK(N_3)-NH_2 (left) and the MMP OR SrtA degradable peptide N_3-RGPQGIWGQLPETGGRK(N_3)-NH_2 (right)

The peptides H-RGPQGIWGQGRK(Dde)-NH_2 and H-RGPQGIWGQLPETGGRK(Dde)-NH_2 were synthesized by Fmoc SPPS at 0.25 mmol scale on rink amide resin. The Dde protecting group was cleaved from resin-bound peptide using 2% hydrazine (3 x 10 min). 4-azidobutanoic acid (4x; 259 mg; 2 mmol) was conjugated to the free amines on the N-terminus and deprotected Lysine though *in situ* ester activation using a solution of HATU (3.95X; 750 mg; 1.97 mmol) and diisopropylethylamine (DIEA; 8X; 1.38 mL; 4 mmol) for 90 minutes [1]. Resin was then thrice washed with DMF and thrice with dichloromethane (DCM) prior to peptide cleavage from resin [95%/2.5%/2.5% Trifluoracetic Acid (TFA)/ Triisopropylsilane (TIS)/ H_2O]. Crude peptide product was precipitated in ice-cold diethyl ether and dried under N_2 prior to purification by RP-HPLC (55-minute gradient of 5-100% acetonitrile in water). Lyophilization yielded the pure final products (N_3-RGPQGIWGQGRK(N_3)-NH_2 and N_3-RGPQGIWGQLPETGGRK(N_3)-NH_2), each as a light-yellow solid. Peptide identity was confirmed using MALDI-TOF.

Peptide Sequence	Expected Mass (Da)	Observed Mass (Da)	Yield (mg)	Yield (mmol)	Yield (%)
N_3-RGPQGIWGQGRK(N_3)-NH_2	1559.83	1560.36	52.5	0.033	13.2
N_3-RGPQGIWGQLPETGGRK(N_3)-NH_2	2056.08	2058.47	51.2	0.025	9.9

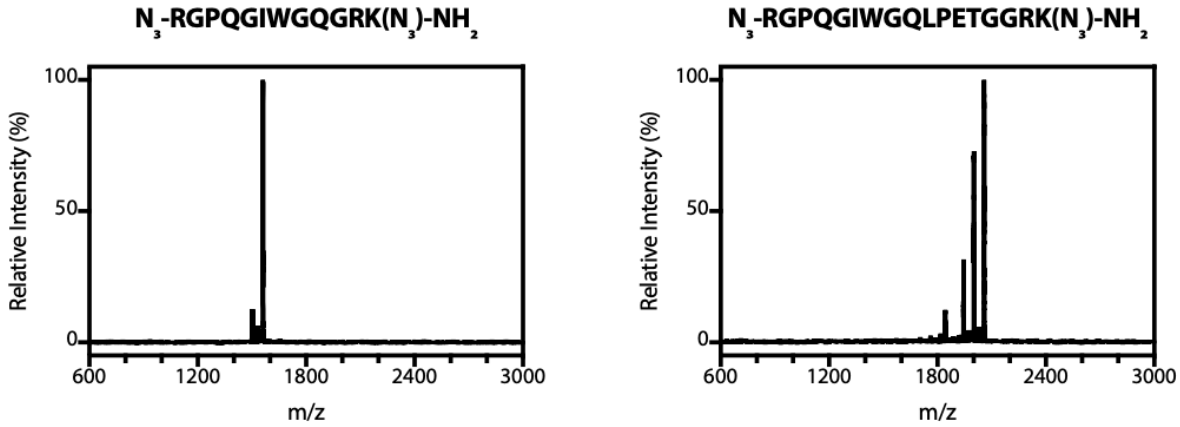

MALDI mass spectra for the synthesized and HPLC purified peptides.

Preparation of Patterning Rails for cell-encapsulated PEG hydrogel patterning.
Rails were printed with a Form 2 3D printer. Devices were sterilized under UV light for 1 hour. To prevent hydrogel or cell adhesion, the devices were incubated in 1% Bovine Serum Albumin (BSA) for 1-2 hours, and allowed to fully air dry prior to use.

References

1. DeForest, C.A.; Tirrell, D.A. A photoreversible protein-patterning approach for guiding stem cell fate in three-dimensional gels. *Nat. Mater.* **2015**, *14*, 523–531.
2. Arakawa, C.K.; Badeau, B.A.; Zheng, Y.; DeForest, C.A. Multicellular Vascularized Engineered Tissues through User-Programmable Biomaterial Photodegradation. *Adv. Mater.* **2017**, *29*, 1703156.
3. Bellis, S.L. Advantages of RGD peptides for directing cell association with biomaterials. *Biomaterials* **2011**, *32*, 4205–4210.

Supplementary Figures

Note: Figures C1-4 are demonstrations of the resolution in agarose structures achievable with the Form 2 3D printer that we used to fabricate the rail structures and is not inherent to the 3D patterning method presented in this paper.

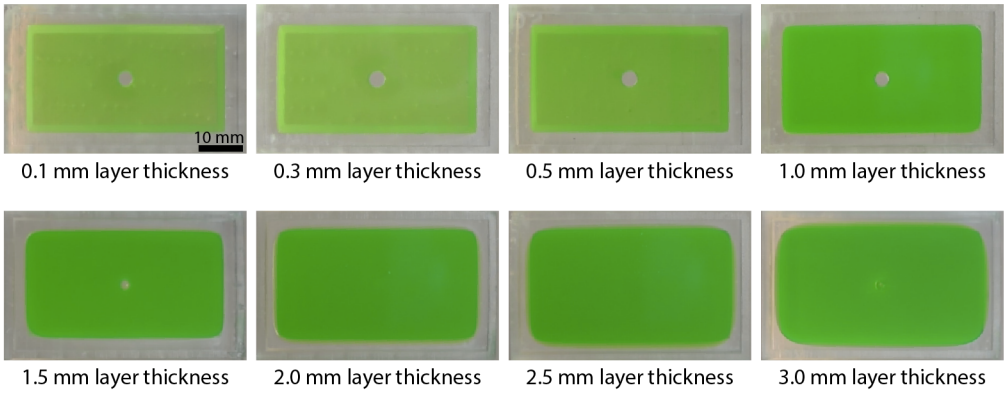

Figure C1. Effects of increasing layer thickness on capillary pinning at corners. At layer thickness 0.1, 0.3, and 0.5 mm the agarose fully fills to the corner of the patterning device. At 1.0 mm and above, agarose is unable to pin at the corners of the patterning device. Images are taken from the underside of single layers of patterned agarose. Images are representative of n=3.

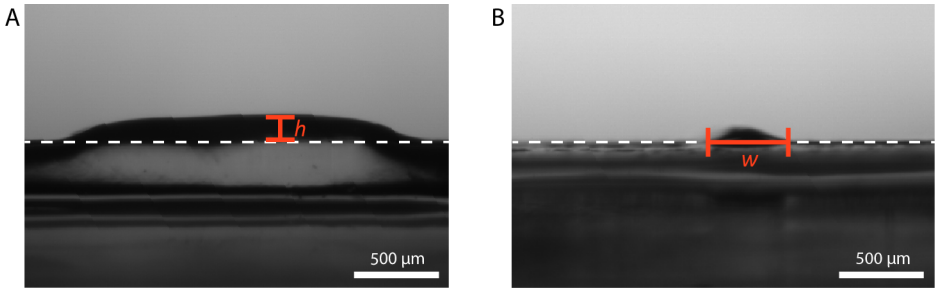

Figure C2. Cross-sectional images of minimum height and width of a layer. (A) Minimum layer height, *h*, was meausred from the baseline (dotted line) to the highest point on the gel layer. The average minimum height was 140 ± 19 µm. (B) Minimum feature width, *w*, was measured at the base of the top layer. The average minimum width was 660 ± 210 µm. At larger widths there was better control over deviations in the width (1292 ± 46 µm). All data are reported as mean ± SD for n=3.

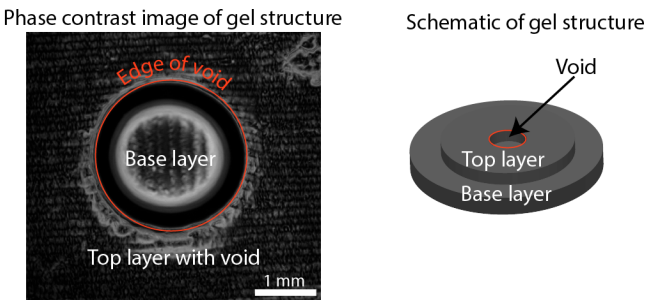

Figure C3. Minimum diameter of void. Red indicates the circle used to measure the diameter of the void. Minimum diameter of void is 1256 ± 18 µm. Data are reported as mean ± SD for n=3. Phase contrast images were taken with a Zeiss Primovert inverted microscope with a MU1403B camera (AmScope).

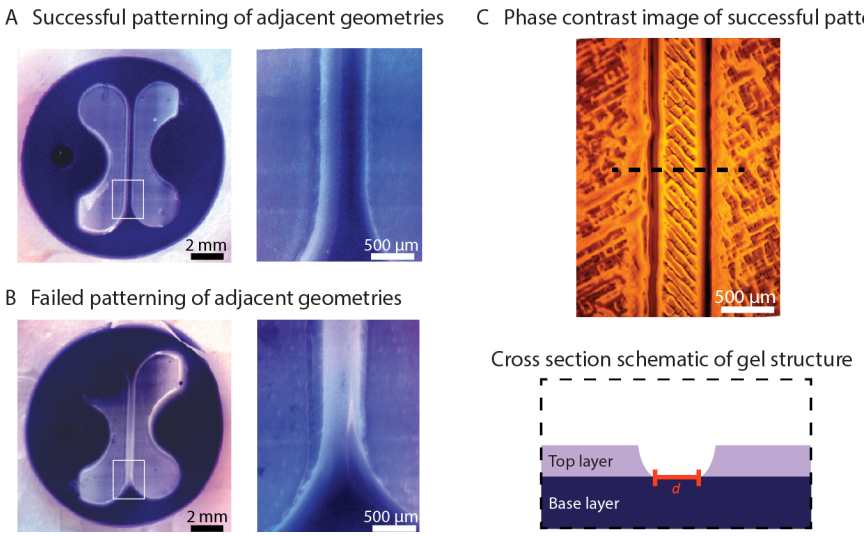

Figure C4. Minimum spacing between two independently patterned geometries (white) over a base layer of gel (purple) is 270 ± 49 µm. (A) Successful patterning of adjacent geometries. (B) Failed patterning of adjacent geometries. (C) Representative image of phase contrast image of agarose structure. Dotted line indicates cross section of the gel in schematic where *d* indates the area of measurement on the gel. Phase contrast images were taken with a Zeiss Primovert inverted microscope with a MU1403B camera (AmScope). All data are reported as mean ± SD for n=3.

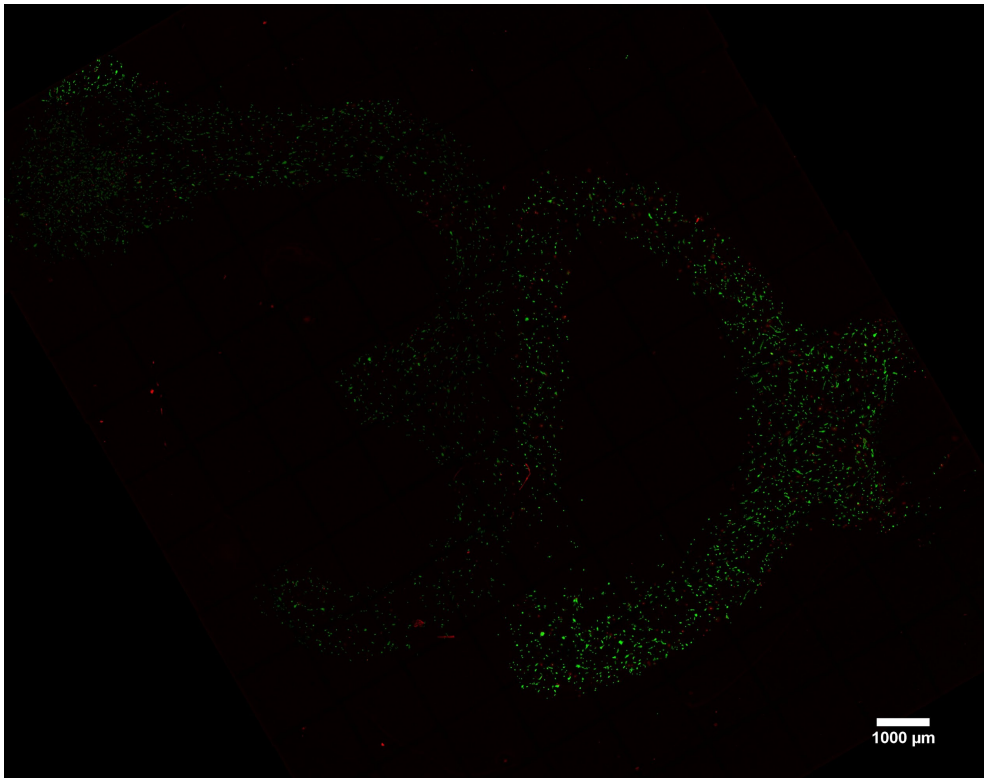

Figure C5. Confocal images showing live/dead staining of human fetal lung fibroblast cells in 3D collagen structure from Figure 6. Image comprises 130 fields of view (which each contain 27 Z-stacked images) stitched together. Green is Calcein AM, which stains the cytoplasm of live cells, and red is ethidium homodimer, which stains the nuclei of dead cells. Viability (87% over all, 93% and 86% in the '3' and D' patterns, respectively) was quantified in FIJI image processing software (using a minimum cell area of 25 px^2 for the live and dead stains and a minimum circularity of 0.25 for the dead stain).

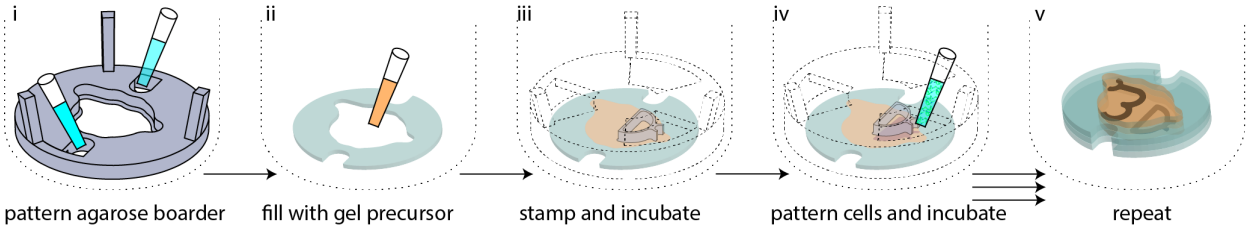

Figure C6. Schematic workflow of agarose and collagen patterning process used to make the cell-laden collagen structure in Figure 6. (i) A 200 μm tall agarose border is patterned in a 6-well plate. (ii) The agarose border is then filled with collagen gel precursor. (iii) A 200 μm tall 'D' patterning device is then placed in the well, which precisely sets the height of the collagen fill to 200 μm (the patterning device is shown as two parts for visualization purposes, where the main device component is shown in dotted lines and the 'D' patterning component is shown in transparent grey). The well plate is then incubated with the device in place for 10 minutes to polymerize the collagen. (iv) The previous patterning device is then removed, and an identical, 300 μm tall patterning device is placed in the same position. 8 μL of cell-laden collagen gel precursor solution is then pipetted into the loading region of the patterning device, at which point the gel precursor solution flows through the 'D' pattern. These 4 steps are repeated once more with a '3' pattern, and then again with no pattern to yield (v) the final structure. As described in the manuscript, the final structure consists of a first cell-free layer that is 200 μm tall, then a cell-laden collagen layer containing the 'D' pattern that is 100 μm tall, then a cell-free layer that is 200 μm tall, then a finally cell-laden collagen '3' pattern that is 100 μm tall, then a cell-free layer.

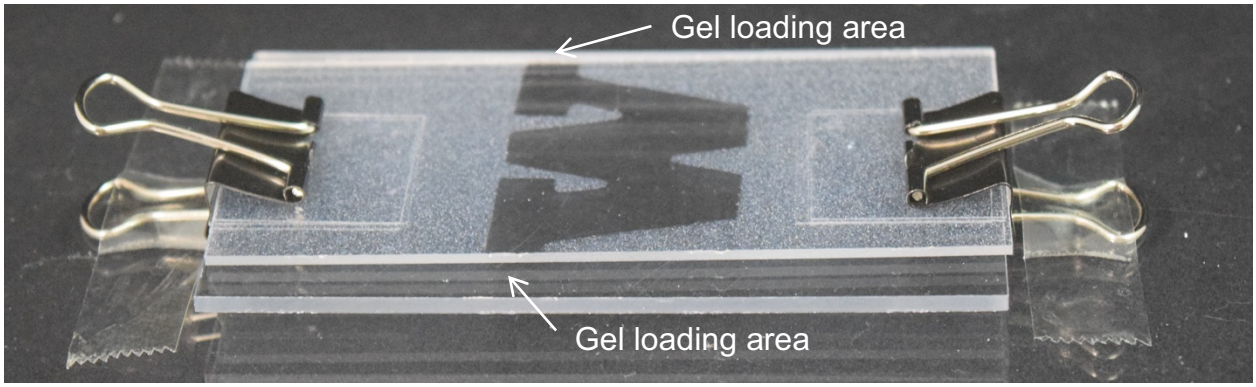

Figure C7. Set up of Figure 8Aii before pre-gel solution is pipetted into gel loading areas.

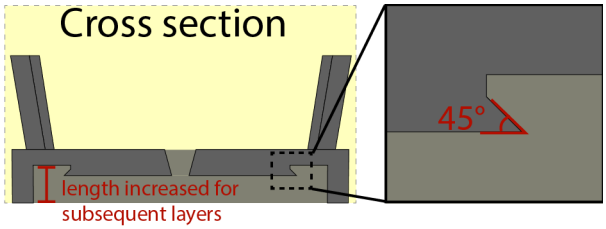

Figure C8. Cross section of patterning device with inset of 45° angled edge to prevent capillary rise. If the patterning device contained a simple 90° angled edge rather than the 45° angled edge shown here, the pre-gel solution would wet the vertical edge of the patterning device due to capillary rise. The diagram also shows the portion of patterning device that is adjusted to increase the height of the patterning area for subsequent layers of hydrogel.

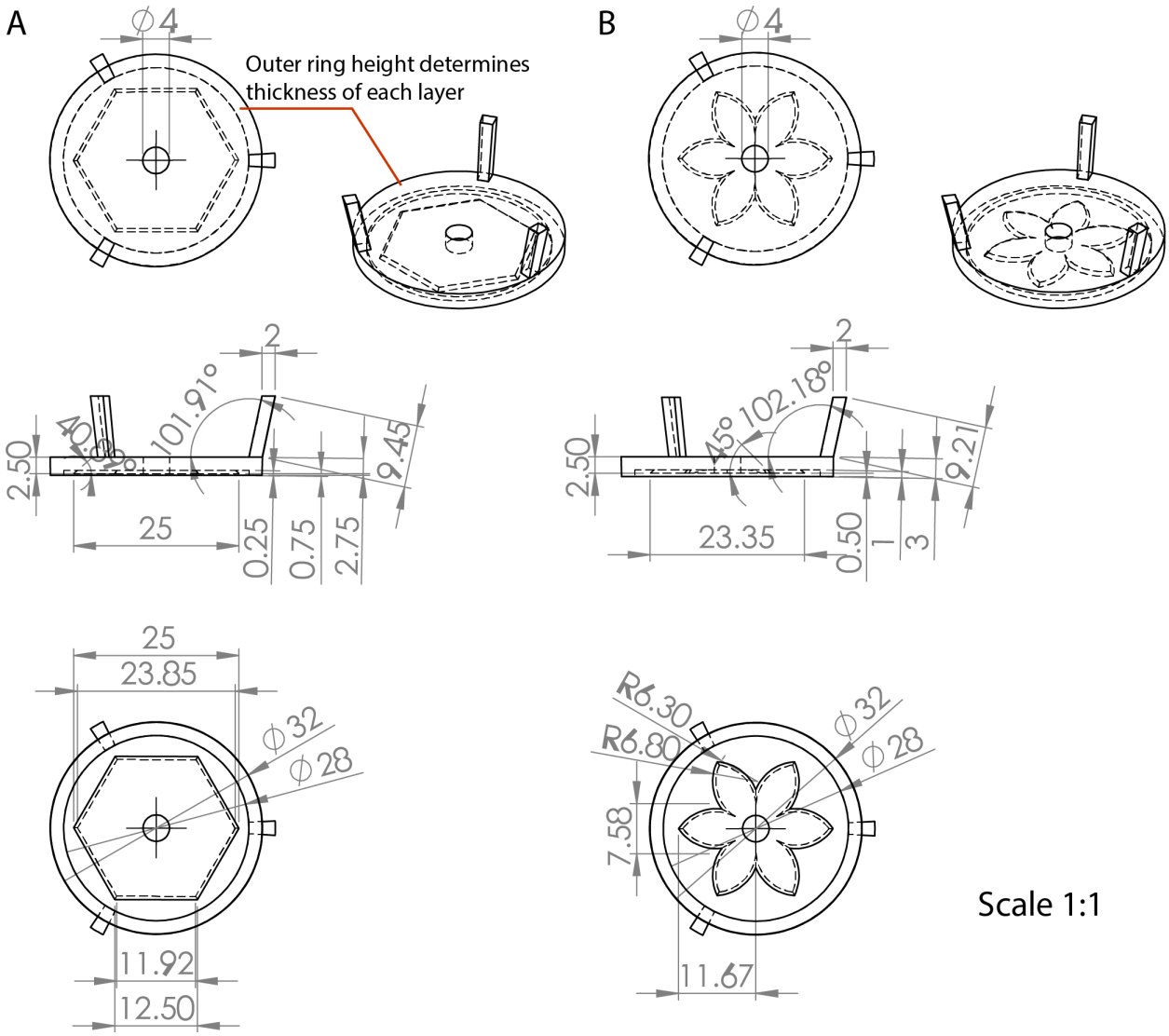

Figure C9. Schematic diagrams illustrating the dimensions of the patterning devices in Figure 2B. (A) First layer hexagon pattern. Red lines indicate the ring ('foot' of the device) that sits flush to the well plate floor which is adjusted for each patterning device to determine layer thickness. (B) Second layer flower pattern.

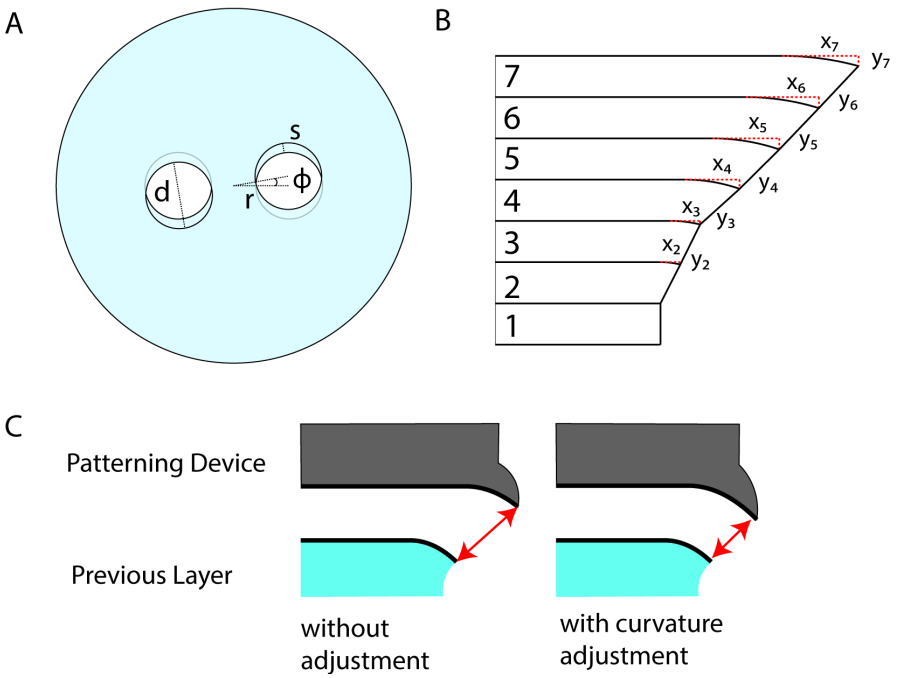

Figure C10. Schematic of helix and overhang design used to make the structures shown in Figure 4 of the manuscript. (A) Dimensions of each design parameter where d is diameter of hole, r is distance from center of the design to the center of the hole, ϕ is the angle of rotation from layer to layer, and s is the maximum overhang length. (B) Schematic of the overhang design for 7 layers, showing the curvatures for each layer. Note: there is no curvature for the first layer. (C) The effect of adjusting the curvature based on the previous curvature on the distance between the two layers, as denoted by the red arrows, which limits the surface capillary flow to the edge of the overhang. The left diagram shows the same curvature for both layers and the right diagram shows curvature adjustment on the patterning device based on the previous layer,

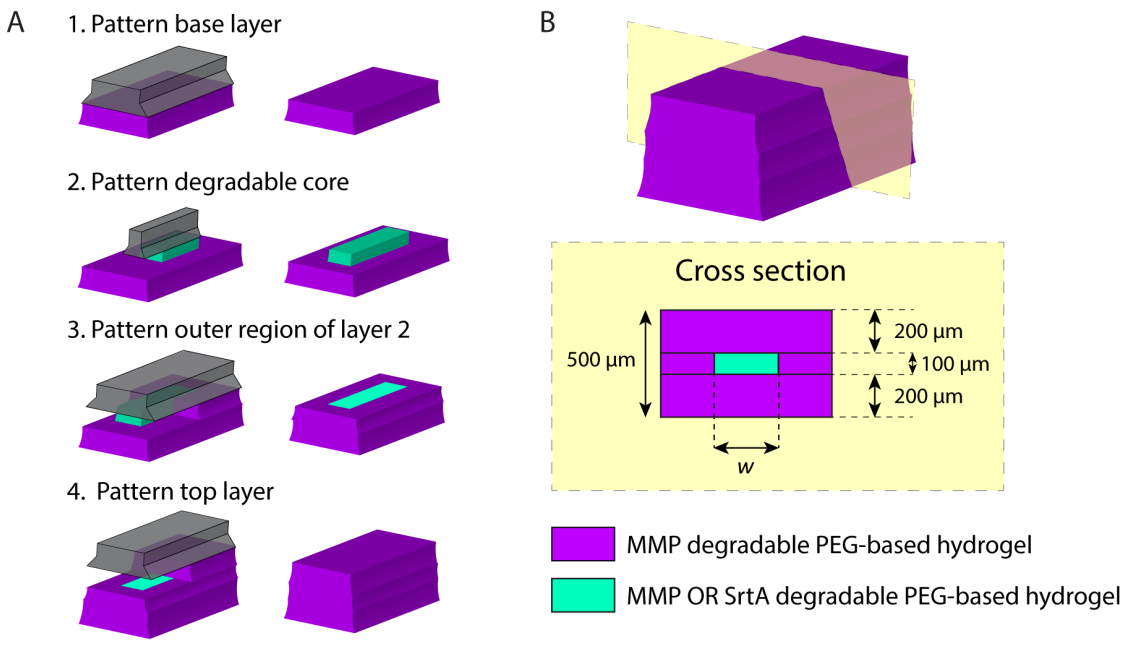

Figure C11. 3D open microfluidic fabrication of PEG-based structure with a enzymatically degradable core. (A) Workflow of fabrication. The gel structure was fabricated in four steps to create a three layered structure consisting of a matrix metalloproteinase (MMP) OR sortase (SrtA) degradable core (teal gel) surrounded entirely by a MMP only degradable gel (purple gel). The middle layer consisting of the core was patterned in two steps, with the SrtA OR MMP degradable core patterned first. (B) Cross section showing dimensions of gel. The total height was designed as 500 μm with the middle layer designed as 100 μm. The width of the core, *w*, was either 1.0 mm or 0.5 mm.

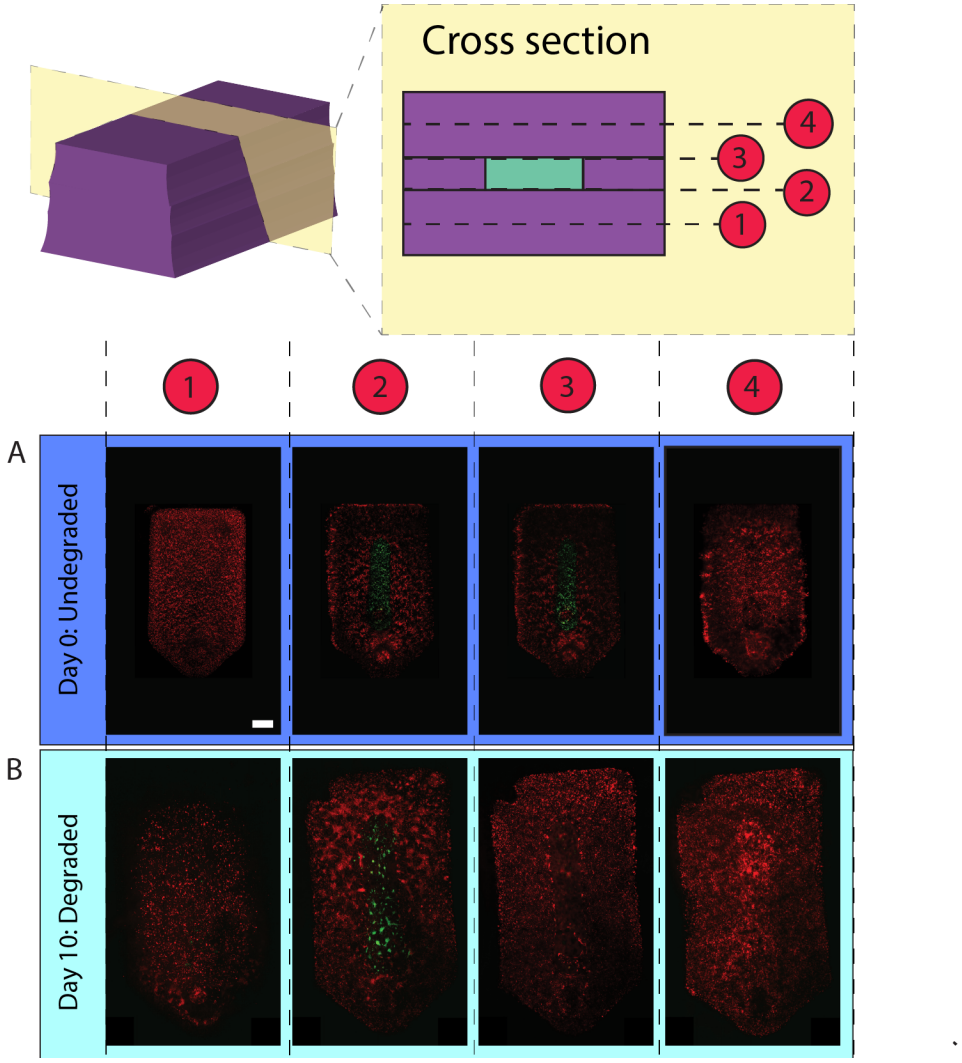

Figure C12. Confocal slices of multiple top-down views of the structure shown in Figure 7. Slice 1-4 is denoted on the cross section schematic with dotted lines. (A) Slices taken from gel just after encapsulation and patterning with no SrtA degradation. (B) Slices taken from gel on day 10 of culture, after SrtA degradation on day 5. eGFP expressing cells are not found in at the top of the middle layer (cross section 3), as the cells have settled to the bottom of the cavity. Scale bar is 1 mm.

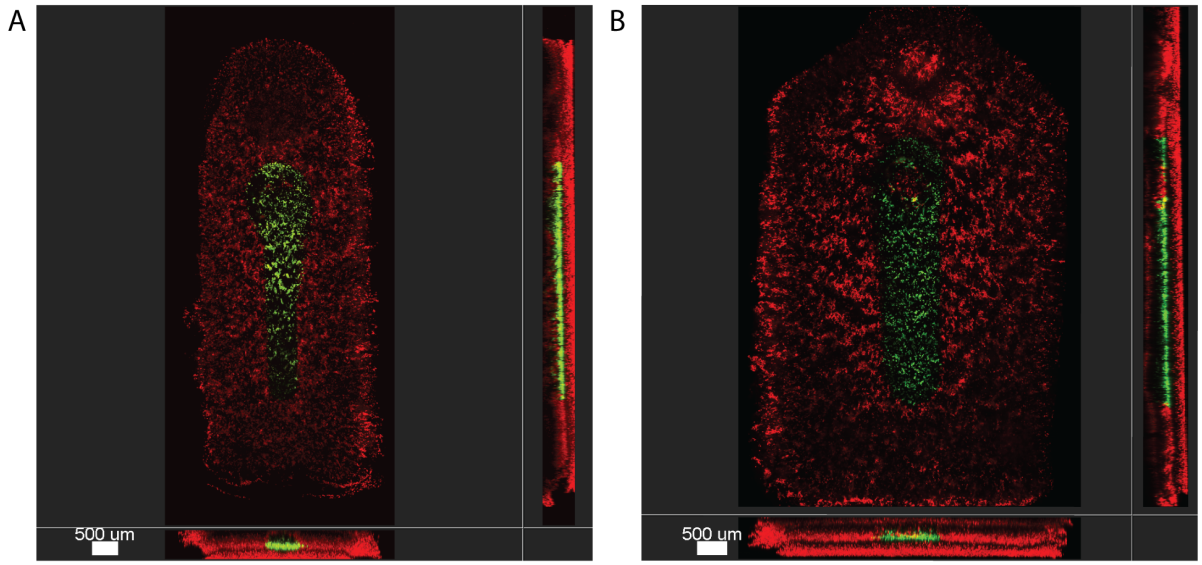

Figure C13. Confocal images of different degradable core geometries. (A) Degradable core width designed with a width of 0.5 mm, and the outside structure was designed with a width of 2.5 mm (B) Degradable core width designed with a width of 1.0 mm with an outside structure designed with a width of 4.5 mm. Scale bars apply to all planes of imaging.

Table C1. Calculated designed curvature values for all patterning devices used for double helix structure.*

Layer	Rotation angle, ϕ (degree)**	Maximum overhang*** (μm)	Radius of curvature (mm)	Horizontal length of curvature, x (μm)	Vertical length of curvature, y (μm)
1	0	0	0	0	0
2	5	239.9	1.0	239.9	29.2
3	5	239.9	1.5	359.9	43.8
4	10	479.4	2.0	659.3	111.8
5	10	479.4	2.5	809.1	134.5
6	10	479.4	3.0	884.0	133.2
7	10	479.4	3.5	921.4	123.5
8	10	479.4	4.0	940.1	112.0
9	10	479.4	4.5	949.5	101.3
10	10	479.4	5.0	954.2	91.9
11	10	479.4	5.5	956.5	83.8
12	10	479.4	6.0	957.7	76.9
13	10	479.4	6.5	958.3	71.0
14	10	479.4	7.0	958.6	65.9
15	10	479.4	7.5	958.7	61.5
16	10	479.4	8.0	958.7	57.7
17	10	479.4	8.5	958.7	54.2
18	10	479.4	9.0	958.7	51.2
19	10	479.4	9.5	958.7	48.5
20	10	479.4	10.0	958.7	46.1
21	10	479.4	10.5	958.7	43.9
22	10	479.4	11.0	958.7	41.9
23	10	479.4	11.5	958.7	40.0
24	10	479.4	12.0	958.7	38.4

25	10	479.4	12.5	958.7	36.8
26	10	479.4	13.0	958.7	35.4
27	10	479.4	13.5	958.7	34.1
28	10	479.4	14.0	958.7	32.9
29	10	479.4	14.5	958.7	31.7

*First seven layers curvature and overhang information also corresponds to the cross section device in Figure 4A.
**Rotation angle represents the rotation change from the previous layer. Values are in degrees.
***Maximum overhang corresponds to s in Figure C10A.

D. Appendix for Chapter 5

Reproduced in part from U. N. Lee, T. L. van Neel,* F. Y. Lim, JW. Khor, J. He, R. S. Vaddi, A. Q. W. Ong, A. Tang, J. Berthier, J. S. Meschke, I. V. Novosselov,[#] A. B. Theberge,[#] E. Berthier,[#] "Miniaturizing wet scrubbers for aerosolized droplet capture." Analytical Chemistry, 2021, **93**, 11433–11441.*
** Equal contribution*
[#]Co-corresponding authors

Extended Materials and Methods

Non-portable Electronics (Figures D3-D6): The ultrasonic atomizer (Comidox) with a frequency of 113 KHz and 730 apertures 5 μm in diameter was adhered to the floor of the ultrasonic atomizer cup with super glue (Ultra Gel Control, Loctite) or 100% silicone caulk (Gorilla Glue). A 40 mm square computer fan (Model AB4010M12**,** HK Fan) was used to generate airflow. The voltage delivered to the fan was controlled by a microcontroller (Arduino Uno, Arduino) and L298N transistor (Qunqi). Two power supplies and 2.1 mm male and female barrel jacks (Centropower) were required for this setup.

Simulations (Figure D5): The *Laminar Flow,* physics interface, governed by the Navier-Stokes equations, was selected to model air flow in the device. Air was modeled as an incompressible fluid with standard fluid values at 1 atm (reference pressure) and 293.15 K (reference temperature). Two fan inlets and one outlet were set with the remaining boundary conditions set no slip. A fine element, free quadrilateral mesh was used for the majority of the device; an extra fine, free quadrilateral mesh calibrated for fluid dynamics was used for the baffle features. A stationary study was used with a direct, fully coupled linear solver.

Fan flow rate measurement (Figure D7): The device was attached to a 1 ft long pipe and a hot-wire anemometer (AN-1005) was used to measure the velocity profile at the outlet of the pipe. These velocity measurements were also used for calculations of the sampling flow rate. TSI 1213-20 hot wire probe connected to an anemometer was positioned at the outlet. The anemometer was calibrated for the range of 0.2 m/s - 7 m/s using the standard calibration procedure. The data from the anemometer was collected at a frequency of 10 kHz with a data acquisition module (National Instruments, myRIO-1900) for a sampling time of 30 seconds. The experiments showed the maximum velocity was located at the centerline; the profile decays with radial distance. The maximum velocity of the device was ~0.28 m/s for both devices/ fans and flowrate is ~6.3+/-0.7 slpm. Data in SI Figure D3.

Bacteriophage MS2 propagation (Figure D8): *Escherichia coli* bacteriophage MS2 was propagated using the Adam's Overlay method.[1] Briefly, Tryptic Soy Agar (TSA) plates were prepared and stored at RT overnight. A 2 mL aliquot of an overnight culture of the host species (*E. coli* Famp) was inoculated with 100 μL bacteriophage MS2 and incubated for 1 hr at 37 ºC with shaking. An additional 2-3 mL of overnight host culture was then mixed with the 1 hr phage MS2 culture and top agar before being poured onto prepared TSA plates for an overnight incubation at 37 ºC. Plates were then washed with 5-10 mL PBS for 5-10 mins before top agar was collected, rinsed with chloroform, and centrifuged (4000 x g for 15 mins at 4 ºC). Supernatant was then collected and mixed with glycerol for a final composition of 20% glycerol, 80% bacteriophage MS2 before being aliquoted. 1 mL aliquots were stored at -80 ºC until use.

(1) Adams, M.H. Bacteriophages. New York: Interscience Publishers, 1959.

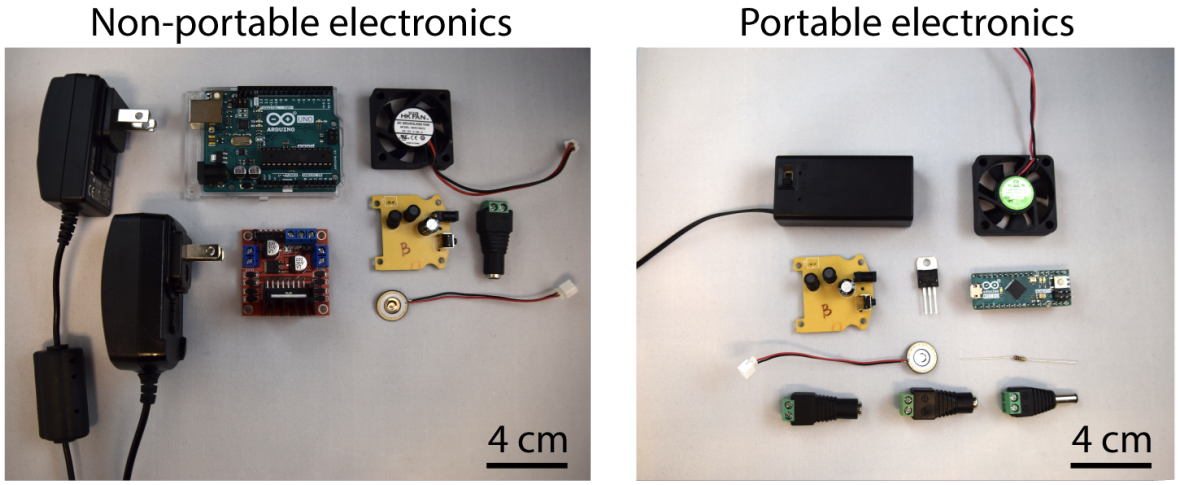

Figure D1. Photo of non-portable electronic components used for droplet retention measurements and videos (Figures D3-D6) and portable electronics used for particle chamber experiments (Figure D7 and D8). Wires not pictured.

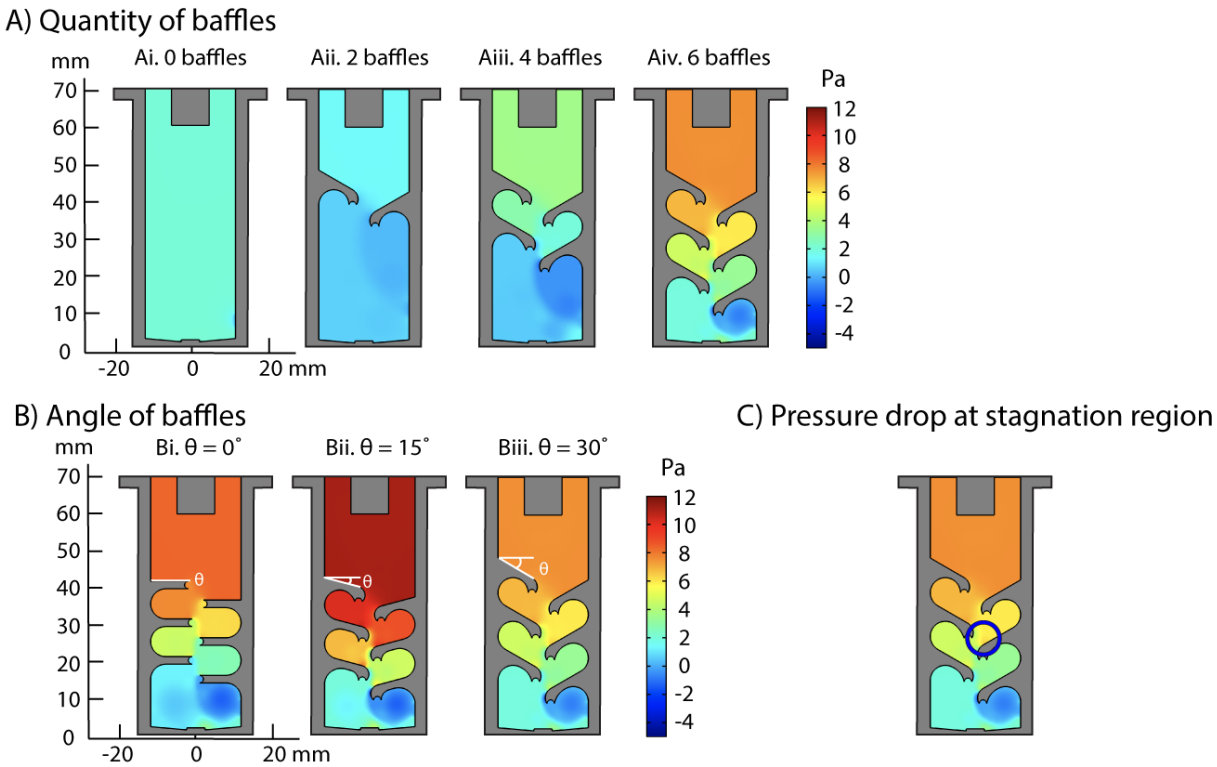

Figure D2. Pressure maps from simulations of device iterations pictured in Figure 5. (A) Pressure above the top baffles increases with each additional set of baffles. (B) When the angle of the baffle is changed from 0° to 15°, pressure increases before decreasing again at a 30° baffle angle. Reduced pressure is preferable to allow aerosol entrance into the device. (C) The pressure drop generated by impinging jets at stagnation regions increases droplet coalescence on baffle surfaces. Scale bar indicates the pressure above or below atmospheric pressure (i.e., 0 Pa = atmospheric pressure

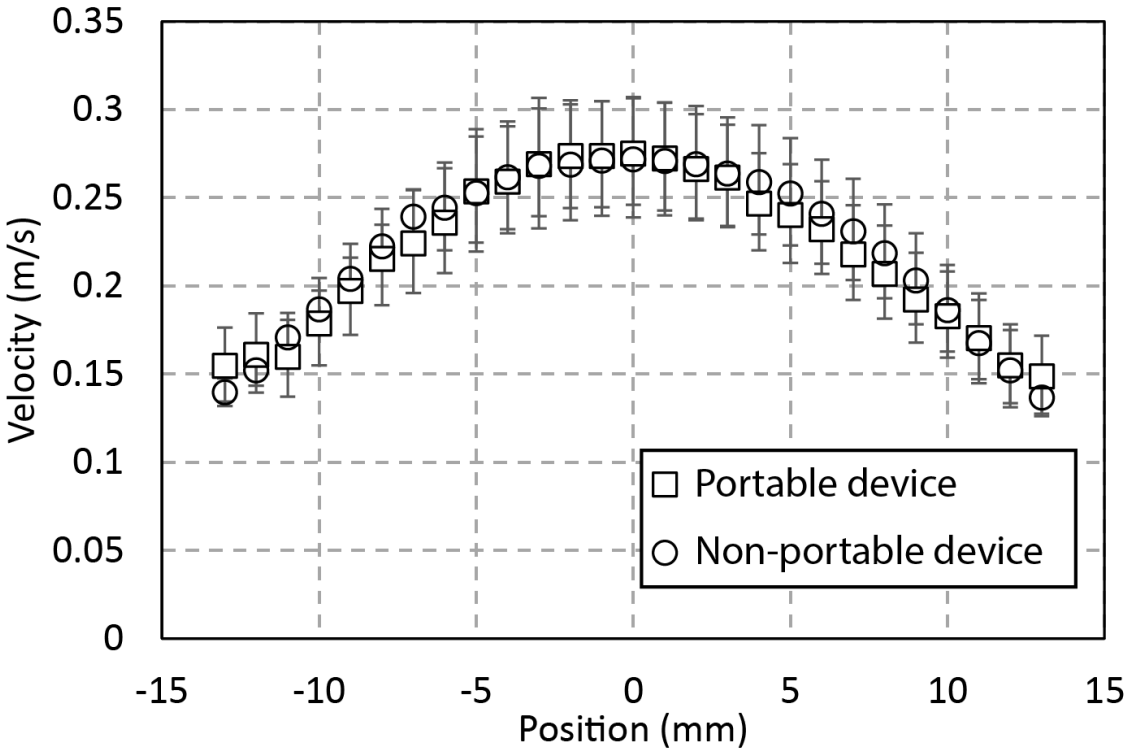

Figure D3. Plot of air flow velocity from the outlet of the device comparing the airflow rate between our non-portable device (Figures D3-D6) and our portable device (Figure D7 and D8). The two devices used two different fans to accommodate voltage requirements for each electronics set up, but produced the same velocity and volumetric flow rate.

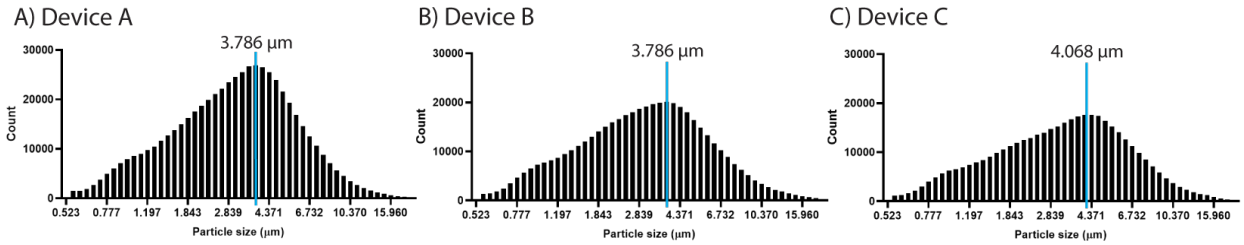

Figure D4. Droplet size distributions for each device as measured using an aerodynamic particle sizer. Average droplet size ± SD from n=3 devices is 3.88 ± 0.16 µm.

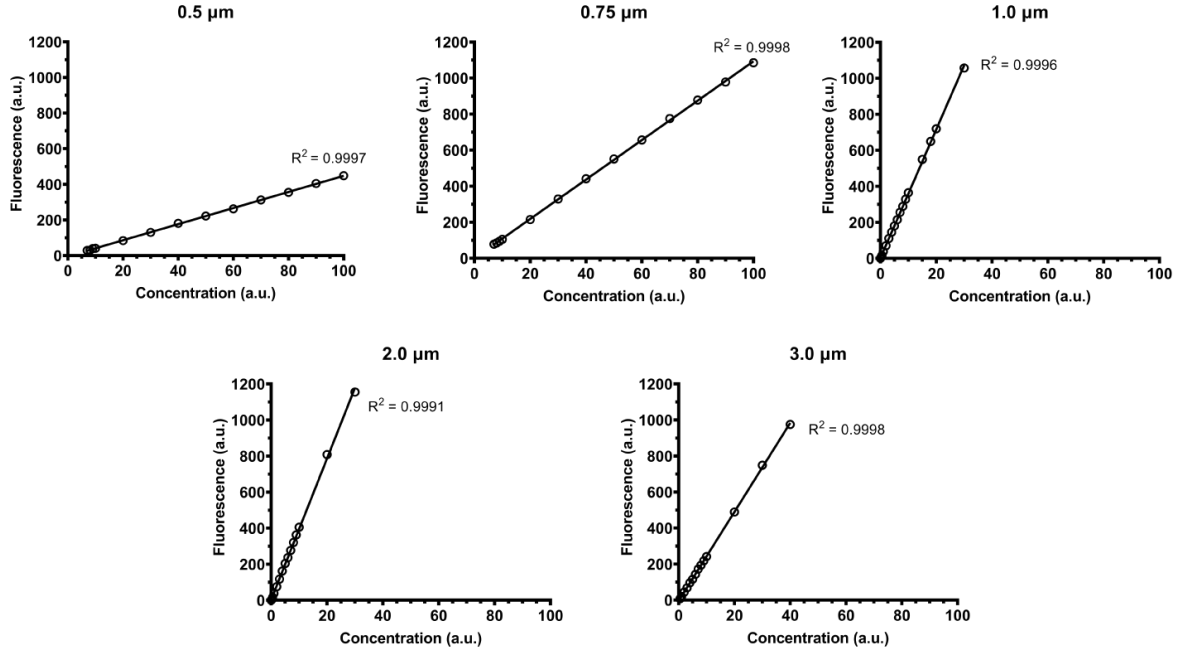

Figure D5. Calibration curves for each particle size used in Figure D7. Calibration curves were used to validate fluorescent signals of samples collected from devices and reference filters were in the linear range. Points represent mean ± SD of n=3. In all cases the standard deviation was smaller than the point plotted.

Table D1. Particle concentration used in the test chamber for each particle size. Particle concentrations used at each size varied to ensure adequate particles were aerosolized and available for capture in the test chamber as in prior work (He, J.; Novosselov, I. V., Design and evaluation of an aerodynamic focusing micro-well aerosol collector. *Aerosol Science and Technology* **2017,** *51* (9), 1016-1026). During each 25-minute chamber run, 2-3 mL of solution was nebulized. Concentration reported here was measured with the aerodynamic particle sizer (APS) attached to the chamber exhaust.

Particle size (µm)	**Concentration (particle/cm^3)**
0.50	4500-5500
0.75	10000-13000
1.0	4200-5800
2.0	1200-1500
3.0	1200-1500

Table D2. Diameter of aerosolized biological particles of interest. To avoid unnecessary exposure to known biological pathogens in this initial characterization publication, we chose to use monodispersed fluorescent polystyrene latex spheres as a proxy. Sizes used were based on relevant bioaerosols that are known to adversely affect human health.

Diameter of inert particle proxy (µm)	**Diameter of relevant bioaerosol (µm)**	**Reference**	**Examples of human health impact**
0.5	SARS-CoV-2 aerosols 0.25 - 0.5	Liu, Y. et al., *Nature* **2020**, *582* (7813), 557–560.	COVID-19, respiratory complications
0.75	*Staphylococcus aureus* 0.5 - 1.0	Madsen, A. M. et al., *Annals of Work Exposures and Health* **2018**, *62* (8), 966–977.	Sepsis, pneumonia, infections
1.0	viral particle + respiratory droplet ≤ 1.0	Fennelly, K. P. *The Lancet Respiratory Medicine* **2020**, *8* (9), 914–924.	Flu, common cold
2.0	*Aspergillus fumigatus* 2 - 3.5	Kwon-Chung, K. J. et al., *PLoS Pathog* **2013**, *9* (12).	Pulmonary aspergillosis, allergic asthma
3.0	*Mycobacterium tuberculosis* 2 - 4	Kim, K.-H. et al., *Journal of Environmental Sciences* **2018**, *67*, 23–35.	Tuberculosis

Table D3. Relative standard deviation (RSD) of reference filters and devices across the three experimental test chamber runs. While variability is generally higher in our devices, it is important to note variability also exists within the reference filters used, likely due to the manual control of the flow rate and particle nebulization. The averages shown here were taken from n=3 devices or n=3 reference filters within a run of the test chamber.

A) 0.5 µm particles

	Device Avg (a.u.)	Device RSD (%)	Reference Avg (a.u.)	Reference RSD (%)
run 1	104.2	**23.9**	495.5	**8.8**
run 2	102.5	**9.2**	654.4	**14.8**
run 3	83.9	**13.9**	662.3	**23.4**

B) 0.75 µm particles

	Device Avg (a.u.)	Device RSD (%)	Reference Avg (a.u.)	Reference RSD (%)
run 1	164.7	**25.8**	1954.2	**5.4**
run 2	132.7	**17.8**	1138.3	**19.0**
run 3	107.0	**19.8**	1335.7	**16.8**

C) 1.0 µm particles

	Device Avg (a.u.)	Device RSD (%)	Reference Avg (a.u.)	Reference RSD (%)
run 1	68.3	**56.6**	1096.8	**5.1**
run 2	113.0	**77.3**	1206.0	**14.8**
run 3	66.7	**17.0**	880.2	**19.4**

D) 2.0 µm particles

	Device Avg (a.u.)	Device RSD (%)	Reference Avg (a.u.)	Reference RSD (%)
run 1	38.1	**38.7**	1237.1	**7.6**
run 2	55.3	**16.2**	1224.3	**4.6**
run 3	54.6	**18.7**	1366.9	**4.9**

E) 3.0 µm particles

	Device Avg (a.u.)	Device RSD (%)	Reference Avg (a.u.)	Reference RSD (%)
run 1	29.0	**17.4**	682.4	**10.1**
run 2	42.2	**26.1**	738.6	**1.6**
run 3	48.3	**51.7**	738.3	**0.7**